

FRONTIERS IN LIFE SCIENCES AND RELATED TECHNOLOGIES



AGRICULTURAL SCIENCES BIOLOGY BIOCHEMISTRY
BIOINFORMATICS BIOTECHNOLOGY BIOCONTROL
BIOMECHANICS BIOCOMPUTERS BIOENGINEERING
BIOELECTRONICS BIOPHYSICS BIOMATERIALS
BIOMEDICAL SCIENCES BIOMONITORING BIOPOLYMERS
CELL BIOLOGY CONSERVATION BIOLOGY CRYOBIOLOGY
ECOLOGY ENVIRONMENTAL SCIENCES FOOD SCIENCES
GENETICS GENOMICS IMMUNOTHERAPY MARINE SCIENCES
MEDICAL SCIENCES MICROBIOLOGY MOLECULAR BIOLOGY
METABOLOMICS NANOTECHNOLOGY NEUROSCIENCES
PHYSIOLOGY PHARMACOGENOMICS PHARMACOLOGY
POPULATION DYNAMICS PROTEOMICS REMEDIATION
SYNTHETIC BIOLOGY SYSTEMATICS TOXICOLOGY

AUGUST, 2023, VOLUME 4, ISSUE 2

Contents

Research Articles

- **Fluorescence-based thermal stability screening is concentration-dependent and varies with protein size**

Elif Yavsan, Sibel Kalyoncu

Pages: 62-67

- **Investigating the relationship between COVID-19 and total oxidative stress and antioxidant capacity in individuals**

Aysegul Oglakci Ilhan, Serhat Sirekbasan, Filiz Yarimcan, Ayse Istanbulu Tosun

Pages: 68-71

- **Identification and verification of promising diagnostic genes in bisphenol A-associated breast cancer development via *in silico* analysis**

Mervenur Akkus, Hamid Ceylan

Pages: 72-78

- **Structural, thermoelectric, and magnetic properties of pure and Ti-doped $\text{Ca}_3\text{Co}_4\text{O}_9$ ceramic compounds**

Cihat Boyraz

Pages: 79-84

- **Identification of phenolic content, antibacterial and antioxidant activities of *Lonicera caucasica* PALLAS subsp. *orientalis* leaves**

Mehmet Emin Seker

Pages: 85-91

- **Automated comet assay segmentation using combined dot enhancement filters and extended-maxima transform watershed segmentation**

Lavdie Rada Ulgen

Pages: 92-98

- **Infuse herbal oils: a comparative study of wheat germ and tomato seed oils**

Firat Baris Barlas

Pages: 99-104

- **Important extremophilic model microorganisms in astrobiology**

Simge Emlik, Sevgi Marakli

Pages: 105-110

Issue Editorial Board

Prof. Dr. Ali ASLAN

Institution: Van Yuzuncu Yil University

Prof. Dr. Muhammad ASHRAF

Institution: University of Lahore

Prof. Dr. Goksel DEMIR

Institution: University of Health Sciences, Türkiye

Prof. Dr. Nermin GOZUKIRMIZI

Institution: Istanbul University

Editor

Prof. Dr. Ibrahim Ilker OZYIGIT

Co-Editors



Asst. Prof. Dr. Ibrahim Ertugrul YALCIN

Assoc. Prof. Dr. Aysegul YILDIZ



Research article

Fluorescence-based thermal stability screening is concentration-dependent and varies with protein size

Elif Yavsan¹ , Sibel Kalyoncu*¹ ¹ Dokuz Eylul University, Izmir Biomedicine and Genome Center, 35340, Izmir Türkiye

Abstract

Proteins are used in many areas including diagnostic and therapeutical applications. Screening protein stability is an essential step for production, pharmacokinetic/pharmacodynamic studies, and determination of storage conditions. Instability of proteins can cause serious problems such as activity loss and unexpected adverse effects, so determination of sensitive and reliable methods for protein stability measurement is crucial. There are several “gold-standard” protein stability tests such as differential scanning calorimetry (DSC), but they are usually not suitable for high-throughput settings and consume large amounts of proteins. Instead, more high-throughput methods such as fluorescent-based assays can be used and validated to make stability screening process more straight-forward, easier, and lower-cost. Here, two methods were systemically compared to see whether their measurements depended on protein sizes. DSC and Sypro Orange dye-based fluorescent assay were compared for various proteins with different sizes and quaternary structures. This is the first systemic comparison of these two methods for thermal stability testing for different ranges of proteins in the literature. It was shown that protein melting temperature (T_m) measured by fluorescent assay highly depends on protein concentration and protein size. Larger proteins with multi-domain structures such as monoclonal antibodies gave more deviated and lower than expected T_m s compared to small proteins. It has been concluded that fluorescent-based thermal stability assays are more suitable for smaller proteins, but protein concentrations used are still needed to be optimized in their settings for more reliable results.

Keywords: *Differential scanning calorimetry; fluorescent dye; thermal melt; thermal stability; protein stability*

1. Introduction

Chemical and physical instabilities are challenging for development of protein therapeutics. Chemical instability involves processes that change chemical properties by modifying covalent bonds. Physical instability includes processes such as precipitation, adsorption, denaturation, and aggregation (Manning et al., 1989; Akbarian and Chen, 2022). In the production and development of protein therapeutics, it is essential to screen protein stability during various processes such as expression, purification, formulation, biophysical characterization, *in vivo* testing, and storage. It is important to determine protein stability in the easiest and cheapest way,

especially in areas where various biotechnological products such as protein-based therapeutics, reagents, antibodies, and industrial enzymes are developed (Stourac et al., 2021).

Various techniques are being used to determine protein stability, mainly classifying as label-required and label-free methods (Gromiha, 2010; Rufer and Hennig, 2020). There are also various computational approaches to estimate the thermal stability with improved accuracies (Miotto et al., 2019; Jana et al., 2020; Jung et al., 2023). The most common approaches include differential scanning calorimetry (DSC) (Gill et al., 2010), circular dichroism (CD) (Fiedler et al., 2013), fluorescence-based thermal-shift assays (Lavinder et al., 2009), nuclear magnetic resonance (NMR) (Puglisi et al., 2020), pulse-

* Corresponding author.

E-mail address: sibel.kalyoncu@ibg.edu.tr (S. Kalyoncu).

<https://doi.org/10.51753/flsrt.1209699> Author contributions

Received 24 November 2022; Accepted 16 May 2023

Available online 26 August 2023

2718-062X © 2023 This is an open access article published by Dergipark under the [CC BY](https://creativecommons.org/licenses/by/4.0/) license.

chase methods (Elgendy, 2017), light scattering and gel filtration (Al-Ghobashy et al., 2017). Most widely used label-free method is DSC, which is referred as “gold standard” for protein thermal stability analysis (Vuorinen et al., 2020; Kopra et al., 2022). DSC is a thermal analyzer that examines how the physical properties of a sample are altered with temperature depending on time. It is known that conformational states and physicochemical stability of proteins are thermodynamically-driven (Araya et al., 2012). Thus, direct measurements of thermodynamic parameters and heat effects by DSC is convenient to determine protein thermal stability. However, DSC and some of other label-free techniques requires high amount of protein and they do not adapt to high-throughput experimental settings.

Fluorescence-based assays are very convenient methods to observe and examine protein stability through protein thermal shift technique (Engrola et al., 2023). Various extrinsic fluorescent dyes are being used for high-throughput protein characterization (Hawe et al., 2008; Kirley and Norman, 2022). Because these dyes form only non-covalent interactions with the protein and its solvent environment, they are great tools for accurate predictions of protein states. Besides stability testing, these dyes can be used to analyze various properties of proteins such as hydrophobicity (Cardamone and Puri, 1992), unfolding/refolding (Acharya and Rao, 2003), aggregation/fibrillation (Vetri et al., 2007), crystallization (Groves et al., 2007) and chemical degradation (Anraku et al., 2001). The protein thermal shift assay basically involves incubation of a naturally folded protein with a fluorescent dye and analyzing the fluorescence signal by either a fluorometer or more high-throughput settings like real-time PCR instrument (Layton and Hellinga, 2011). Various dyes such as Sypro Orange, 1.8-ANS (1-anilinophthalene-8-sulfonate) and 2.6-TNS (naphthalene-6-sulfonic acid) are among the common dyes used for protein stability testing (Huynh and Partch, 2015). Most of these dyes provide sensitive detection by fluorescence spectroscopy but have excitable wavelengths outside the range of real-time PCR instruments. Sypro Orange is a dye which binds to hydrophobic parts of proteins to exhibit a fluorescent effect. One of the advantages of using Sypro Orange dye in protein thermal shift analysis is that its fluorescent properties are compatible with filter sets found in high-throughput real-time PCR instruments (Tresnak and Hackel; 2023; Warrender et al., 2023).

In this study, the aim was to compare two most used methods, DSC and fluorescence-based assay for protein thermal stability analysis. While DSC is an excellent label-free method, it has disadvantages such as excessive sample consumption, costly equipment, and time-intensive. More high-throughput and less costly methods are desirable, but their sensitivity and reliability should be comparable to a “gold-standard” method such as DSC. Fluorescent thermal shift assay method based on Sypro Orange dye is very advantageous in both academia and industry due to its low sample consumption, high-throughput potential, use of widely common real-time PCR equipment, and time/cost efficiency (Redhead et al., 2017; Kazlauskas et al., 2021). While DSC is a concentration-independent method (Nemergut et al., 2017), fluorescent-based methods can be concentration-dependent which should be analyzed thoroughly for each protein system. Here, the protein- and dye-concentration dependencies and protein size effects on fluorescent-based thermal assays were documented. According to the results of this study, certain ranges of fluorescent dye and

protein concentrations affect the obtained melting point results. While 5X Sypro Orange dye concentration are optimum for all proteins, lower protein concentrations (2-8 μ M) give the closest T_m results to those of DSC. It can be concluded that dye/protein concentrations in fluorescence-based thermal shift set-ups should be selected based on the size and domain structure of used proteins to obtain reliable thermal stability results.

2. Materials and methods

2.1. Proteins

Receptor-binding domain (RBD) of the SARS-CoV-2 spike protein (amino acids 332-550) was produced *in house* in *Pichia pastoris* system (Kalyoncu et al., 2023). This RBD was a kind gift of Mehmet Inan at Izmir Biomedicine and Genome Center. Commercial bovine serum albumin (BSA, Diagnostum-D661), bevacizumab (Roche), and adalimumab (Abbvie) were used. Concentrations of proteins were measured by their absorbance at 280 nm via NanoDrop (Thermo Fisher).

2.2. Differential Scanning Calorimetry (DSC)

Protein thermal stability and the thermodynamic parameters of protein denaturation were estimated by using a nano-DSC (TA Instruments) equipment. Before DSC measurements, protein solutions (1.2 mg/ml receptor-binding domain (RBD) of the SARS-CoV-2 spike protein, 1 mg/ml bovine serum albumin (BSA), 1 mg/ml bevacizumab, 1 mg/ml adalimumab) were prepared in 1X phosphate-buffered-solution (PBS, pH 7.4) at room temperature. Each sample was placed in a degassing device (TA instruments) at 15 Hg for 15 minutes before measurement. For blank measurement, 1 mL of 1X PBS was loaded into the instrument. The measurements were done in the temperature range of 25-98°C, with a scanning rate of 1°C/min. At least two measurements were done for each protein. The partial heat capacity contribution from 1X PBS and proteins in 1X PBS were measured independently and subtracted. The calorimetric data were corrected for the calorimetric baseline between the initial and the final state by using a sigmoidal baseline from NanoAnalyze software. DSC traces were deconvolved using OriginPro 8.5 software and melting temperatures (T_m) were represented.

2.3. Fluorescence-based thermal stability analysis

Thermal melt profiles of each protein were determined with SYPRO Orange dye (Sigma-S5692) via ABI 7500 Fast RT-PCR instrument. Each protein was diluted in 1X PBS (2, 4, 8, 16, 24, 32 μ M), and mixed with SYPRO Orange dye (2X, 5X, 10X) in opaque 96-well PCR plates and sealed with foil. Fluorescence readings were obtained between 25-99°C with 0.05% ramp rate. Three replicates in the plate were done for each protein and each experiment was repeated at least two times at different days. Obtained melt curves were background subtracted using background signals obtained with 1X PBS control. Transition mid-points (T_m values) from the thermogram data were calculated using the Hill1 equation fit using the OriginPro 8.5 software.

3. Results and discussion

The thermal stability of proteins is only partially

understood despite its great importance in both scientific and industrial fields. Adopting suitable methods for thermal stability measurement will undoubtedly contribute greatly to understanding of physicochemical determinants of protein stability. While “gold standard” methods such as DSC are great tools for stability determination, more high-throughput methods are needed to screen more proteins and conditions at a time. Therefore, reliability of these high-throughput methods should be tested for different proteins because protein size and quaternary structure could be important for their sensitivity.

In this study, four different proteins ranging from small, single-domain proteins to large, multi-domain proteins were tested (Fig. 1). Receptor-binding domain (RBD) of SARS-CoV-2 virus which is 218 amino acids long (332-550 of the Spike protein for SARS-CoV-2) were used (Kalyoncu et al., 2023). RBD is single domain protein with a molecular weight of 25 kDa. Bovine serum albumin (BSA) has three domains with a molecular weight of 66 kDa. As multi-domain proteins, two therapeutic monoclonal antibodies were used: bevacizumab and adalimumab. They are traditional Immunoglobulin G type 1

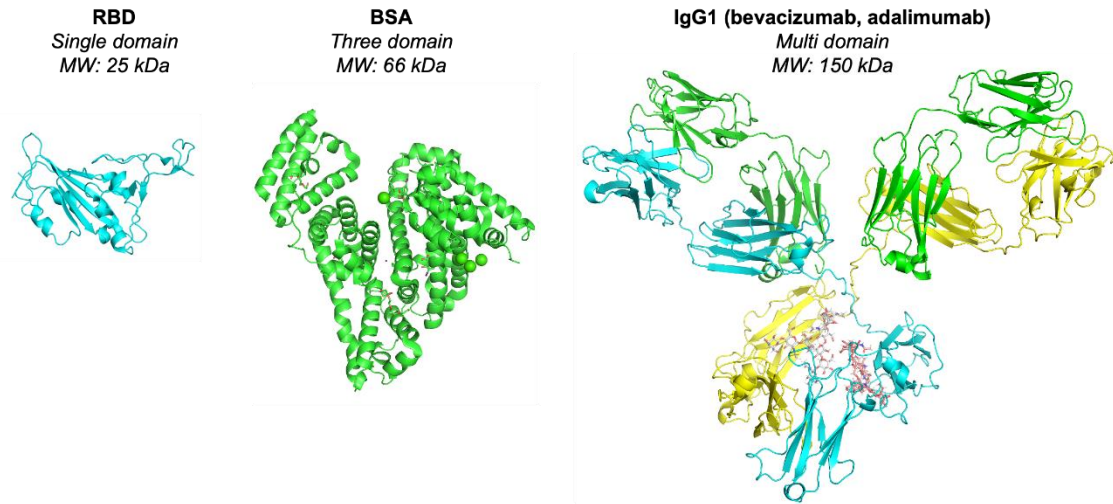


Fig. 1. Structures of proteins used in this study. Cartoon representation of RBD (left, PDB ID: 7E7Y), BSA (middle, PDB ID: 4F5S), IgG1 representing bevacizumab and adalimumab (right, PDB ID: 1HZH). Their domain structures and molecular weights (MWs) are represented on top of each structure.

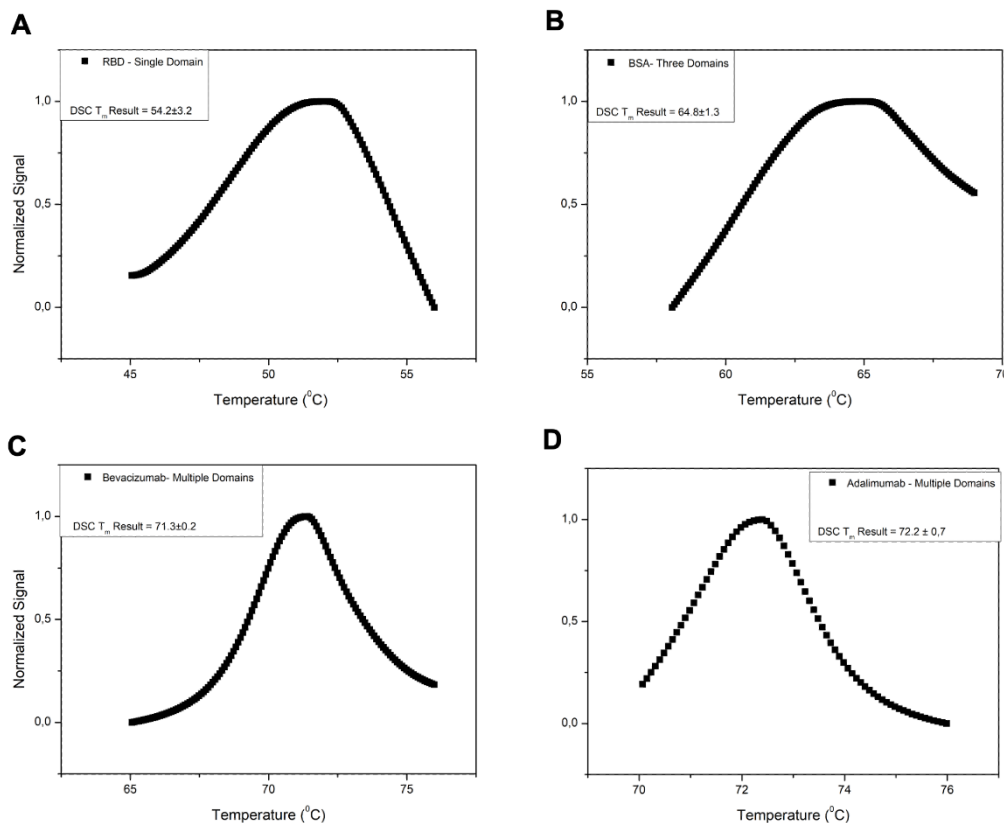


Fig. 2. DSC thermograms of proteins used in this study. Normalized DSC thermograms and calculated thermal melting point (T_m) of (A) RBD (B) BSA, (C) Bevacizumab, (D) Adalimumab.

(IgG1) antibodies with a multi-domain structure and a molecular weight of 150 kDa (Fig. 1).

As a gold standard method (Kopra et al., 2022), DSC was first performed to determine their thermal stability (Fig. 2). While RBD and BSA gave single peak, IgGs gave multiple peaks as expected. The first dominant peak of IgGs which represent Fab region was only potted for comparison (Nemergut et al., 2017), because fluorescent-based methods are usually not that sensitive to resolve multiple transitions. While RBD and BSA gave T_m s of 54.2°C and 64.8°C, respectively (Fig. 2A, 2B), IgGs gave high T_m values around 71-73°C as expected (Fig. 2C, 2D). A large range coverage in T_m values were also targeted from around 50 to 70°C for this study to see whether fluorescent-based methods depend on increasing/decreasing thermal stability.

A high-throughput fluorescent based thermal denaturation experiment was performed in a 96-well setting screening both protein concentration and Sypro Orange dye concentration at the same time in triplicates (Fig. 3). Recommended protein and dye

concentrations for this set-up were 2-20 μ M and 0.5-10X, respectively (Huynh & Partch, 2015). Proteins were screened in 2-32 μ M range and Sypro Orange in 2-10X range. While small proteins gave closer values to DSC T_m values (Fig. 3A, 3B, 3E), large proteins gave more deviated and lower T_m values compared to that of DSC (Fig. 3C, 3D, 3E). In some cases, 2X dye concentration did not gave any reliable data, so they were not included for some of proteins. Also, for RBD and BSA, the lowest protein concentration (2 μ M) did not give any reliable signal. This shows that lower Sypro Orange concentrations for all proteins and lower protein concentrations for small proteins are not suitable for this type of assay. Dye concentration of 5X gave the closest T_m to the DSC data for all proteins used (Fig. 3E). Overall, T_m values obtained from fluorescent-based assay were consistently lower than those of “gold standard”s. While smaller proteins (RBD and BSA) gave more accurate T_m values, larger proteins had much lower T_m s. High deviation in multi-domain proteins were expected due to their allosteric effects of each domain on the stability (Oh et al., 2023). Independent of

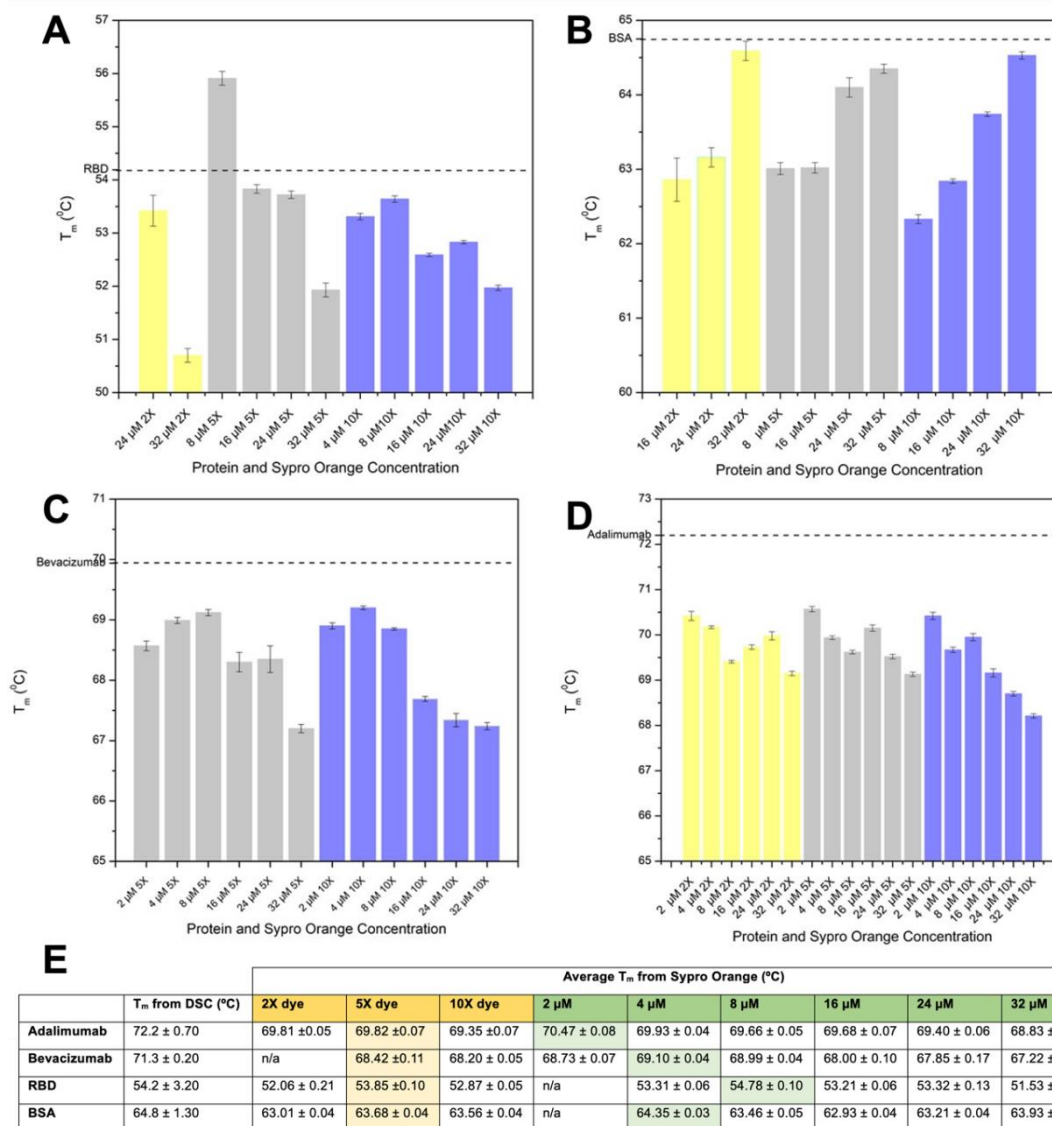


Fig. 3. Fluorescence-based Sypro Orange thermal melt results. Calculated thermal melting point (T_m) of (A) RBD (B) BSA, (C) Bevacizumab, (D) Adalimumab from Sypro Orange based thermal melt. T_m s were calculated from transition mid-points of Hill equation fittings. Dotted lines in each plot represent “gold-standard” T_m of each respective protein measured by DSC. (E) Comparison of average T_m values from DSC and Sypro Orange based thermal melt. Averages were calculated based on each varying dye and protein concentrations, the values closest to the “gold-standard” T_m obtained from DSC were highlighted.

dye concentrations, lower protein concentrations (2-8 μM) gave T_{ms} closer to that of their actual T_{m} (Fig. 3E).

Thermal stability of a protein directly affects its performance. Stability has become a very important issue by researchers and manufacturers, especially with the increasing use of proteins/antibodies in therapeutics, and diagnostics. Instability of proteins has been reported as a major problem in all aspects of research and development (Schuster et al., 2020). Instability in therapeutic proteins can change its pharmacokinetic and pharmacodynamic properties and it can cause adverse effects such as undesired immune response (Boll et al., 2017).

Since protein stability directly affects its production, efficacy, and storage conditions, accurate measurement and screening of their stability is of great importance. High-throughput assays are needed to screen protein stability parameters in various settings, but their sensitivity and reliability should be tested for any protein format. Although it was known that some additives, buffers and concentrations can affect the results of stability analysis (Kopra et al., 2022; Engrola et al., 2023), roles of protein characteristics on the stability measurement are not widely discussed in the literature. Here, a fluorescent-dye based high-throughput assay was compared

with a gold standard method.

According to dye-based assays, it was shown that calculated T_{ms} highly depend on protein concentration and protein size. Larger proteins with multi-domain structures such as monoclonal antibodies gave more deviated and lower T_{ms} compared to those of small proteins. This means that these fluorescent-based high-throughput assays are more suitable for smaller proteins, but protein concentrations are still needed to be optimized in these settings for more reliable results.

Acknowledgments: Authors would like to acknowledge The Scientific and Technological Research Institution of Türkiye (TUBITAK) grant no 119Z161 for funding this research. We thank Aslı Kurden Pekmezci (IBG), Merve Arslan (IBG), Cansu Ergün (Izmir University of Economics), and Ayşe Argünođan (IBG) for their contribution.

Conflict of interest: The authors declare that they have no conflict of interests.

Informed consent: The authors declare that this manuscript did not involve human or animal participants and informed consent was not collected.

References

- Acharya, P., & Rao, N. M. (2003). Stability studies on a lipase from *Bacillus subtilis* in guanidinium chloride. *Journal of Protein Chemistry*, 22(1), 51-60.
- Akbarian, M., & Chen, S. H. (2022). Instability challenges and stabilization strategies of pharmaceutical proteins. *Pharmaceutics*, 14(11).
- Al-Ghobashy, M. A., Mostafa, M. M., Abed, H. S., Fathalla, F. A., & Salem, M. Y. (2017). Correlation between dynamic light scattering and size exclusion high-performance liquid chromatography for monitoring the effect of pH on stability of biopharmaceuticals. *Journal of Chromatography B: Analytical Technologies in the Biomedical and Life Sciences*, 1060, 1-9.
- Anraku, M., Yamasaki, K., Maruyama, T., Kragh-Hansen, U., & Otagiri, M. (2001). Effect of oxidative stress on the structure and function of human serum albumin. *Pharmaceutical Research*, 18(5), 632-639.
- Araya, C. L., Fowler, D. M., Chen, W., Muniez, I., Kelly, J. W., & Fields, S. (2012). A fundamental protein property, thermodynamic stability, revealed solely from large-scale measurements of protein function. *Proceedings of the National Academy of Sciences of the United States of America*, 109(42), 16858-16863.
- Boll, B., Bessa, J., Folzer, E., Rios Quiroz, A., Schmidt, R., Bulau, P., Finkler, C., Mahler, H. C., Huwyler, J., Iglesias, A., & Koulov, A. V. (2017). Extensive chemical modifications in the primary protein structure of IgG1 subvisible particles are necessary for breaking immune tolerance. *Molecular Pharmaceutics*, 14(4), 1292-1299.
- Cardamone, M., & Puri, N. K. (1992). Spectrofluorimetric assessment of the surface hydrophobicity of proteins. *Biochemical Journal*, 282(Pt 2), 589-593.
- Elgendy, M. (2017). Assessment of modulation of protein stability using pulse-chase method. *Bio-Protocol*, 7(16), e2443.
- Engrola, F. S. S., Paquete-Ferreira, J., Santos-Silva, T., Correia, M. A. S., Leisico, F., & Santos, M. F. A. (2023). Screening of buffers and additives for protein stabilization by thermal shift assay: a practical approach. In: Sousa Á., Passarinha L. (eds) *Methods in Molecular Biology* (Vol. 2652, pp. 199-213). Humana.
- Fiedler, S., Cole, L., & Keller, S. (2013). Automated circular dichroism spectroscopy for medium-throughput analysis of protein conformation. *Analytical Chemistry*, 85(3), 1868-1872.
- Gill, P., Moghadam, T. T., & Ranjbar, B. (2010). Differential scanning calorimetry techniques: applications in biology and nanoscience. *Journal of Biomolecular Techniques*, 21(4), 167-193.
- Gromiha, M. M. (2010). Protein folding, stability and interactions. *Current Protein & Peptide Science*, 11(7), 497.
- Groves, M. R., Muller, I. B., Kreplin, X., & Muller-Dieckmann, J. (2007). A method for the general identification of protein crystals in crystallization experiments using a noncovalent fluorescent dye. *Acta Crystallographica Section D: Biological Crystallography*, 63(Pt 4), 526-535.
- Hawe, A., Sutter, M., & Jiskoot, W. (2008). Extrinsic fluorescent dyes as tools for protein characterization. *Pharmaceutical Research*, 25(7), 1487-1499.
- Huynh, K., & Partch, C. L. (2015). Analysis of protein stability and ligand interactions by thermal shift assay. *Current Protocols in Protein Science*, 79(1), 28-29.
- Jana, K., Mehra, R., Dehury, B., Blundell, T. L., & Kepp, K. P. (2020). Common mechanism of thermostability in small alpha- and beta-proteins studied by molecular dynamics. *Proteins: Structure, Function, and Bioinformatics*, 88(9), 1233-1250.
- Jung, F., Frey, K., Zimmer, D., & Muhlhaus, T. (2023). DeepSTABp: A deep learning approach for the prediction of thermal protein stability. *International Journal of Molecular Sciences*, 24(8), 7444.
- Kalyoncu, S., Yilmaz, S., Kuyucu, A. Z., Sayili, D., Mert, O., Soyuturk, H., ... & Inan, M. (2023). Process development for an effective COVID-19 vaccine candidate harboring recombinant SARS-CoV-2 delta plus receptor binding domain produced by *Pichia pastoris*. *Scientific Reports*, 13(1), 5224.
- Kazlauskas, E., Petrauskas, V., Paketuryte, V., & Matulis, D. (2021). Standard operating procedure for fluorescent thermal shift assay (FTSA) for determination of protein-ligand binding and protein stability. *European Biophysics Journal*, 50(3-4), 373-379.
- Kirley, T. L., & Norman, A. B. (2022). Critical evaluation of fluorescent dyes to evaluate the stability and ligand binding properties of an anti-cocaine mAb, h2E2. *Journal of Immunological Methods*, 508, 113323.
- Kopra, K., Valtonen, S., Mahran, R., Kapp, J. N., Hassan, N., Gillette, W., ... & Härmä, H. (2022). Thermal shift assay for small GTPase stability screening: evaluation and suitability. *International Journal of Molecular Sciences*, 23(13), 7095.
- Lavinder, J. J., Hari, S. B., Sullivan, B. J., & Magliery, T. J. (2009). High-throughput thermal scanning: a general, rapid dye-binding thermal shift screen for protein engineering. *Journal of the American Chemical Society*, 131(11), 3794-3795.
- Layton, C. J., & Hellinga, H. W. (2011). Quantitation of protein-protein interactions by thermal stability shift analysis. *Protein Science*, 20(8), 1439-1450.
- Manning, M. C., Patel, K., & Borchardt, R. T. (1989). Stability of protein

- pharmaceuticals. *Pharmaceutical Research*, 6(11), 903-918.
- Miotto, M., Olimpieri, P. P., Di Rienzo, L., Ambrosetti, F., Corsi, P., Lepore, R., Tartaglia, G. G., & Milanetti, E. (2019). Insights on protein thermal stability: a graph representation of molecular interactions. *Bioinformatics*, 35(15), 2569-2577.
- Nemergut, M., Zoldak, G., Schaefer, J. V., Kast, F., Miskovsky, P., Pluckthun, A., & Sedlak, E. (2017). Analysis of IgG kinetic stability by differential scanning calorimetry, probe fluorescence and light scattering. *Protein Science*, 26(11), 2229-2239.
- Oh, J., Durai, P., Kannan, P., Park, J., Yeon, Y. J., Lee, W. K., Park, K., & Seo, M. H. (2023). Domain-wise dissection of thermal stability enhancement in multidomain proteins. *International Journal of Biological Macromolecules*, 237, 124141.
- Puglisi, R., Brylski, O., Alfano, C., Martin, S. R., Pastore, A., & Temussi, P. A. (2020). Quantifying the thermodynamics of protein unfolding using 2D NMR spectroscopy. *Communications Chemistry*, 3(1), 100.
- Redhead, M., Satchell, R., McCarthy, C., Pollack, S., & Unitt, J. (2017). Thermal shift as an entropy-driven effect. *Biochemistry*, 56(47), 6187-6199.
- Rufer, A. C., & Hennig, M. (2020). Biophysical assessment of target protein quality in structure-based drug discovery. In: Renaud J. P. (ed) *Structural Biology in Drug Discovery: Methods, Techniques, and Practices* (pp. 143-164). Humana.
- Schuster, J., Koulov, A., Mahler, H. C., Detampel, P., Huwyler, J., Singh, S., & Mathaes, R. (2020). In vivo stability of therapeutic proteins. *Pharmaceutical Research*, 37(2), 23.
- Stourac, J., Dubrava, J., Musil, M., Horackova, J., Damborsky, J., Mazurenko, S., & Bednar, D. (2021). FireProtDB: database of manually curated protein stability data. *Nucleic Acids Research*, 49(D1), D319-D324.
- Tresnak, D. T., & Hackel, B. J. (2023). Deep antimicrobial activity and stability analysis inform lysin sequence-function mapping. *ACS Synthetic Biology*, 12(1), 249-264.
- Vetri, V., Canale, C., Relini, A., Librizzi, F., Militello, V., Gliozzi, A., & Leone, M. (2007). Amyloid fibrils formation and amorphous aggregation in concanavalin A. *Biophysical Chemistry*, 125(1), 184-190.
- Vuorinen, E., Valtonen, S., Eskonen, V., Kariniemi, T., Jakovleva, J., Kopra, K., & Harma, H. (2020). Sensitive label-free thermal stability assay for protein denaturation and protein-ligand interaction studies. *Analytical Chemistry*, 92(5), 3512-3516.
- Warrender, A. K., Pan, J., Pudney, C. R., Arcus, V. L., & Kelton, W. (2023). Constant domain polymorphisms influence monoclonal antibody stability and dynamics. *Protein Science*, 32(3), e4589.

Cite as: Yavsan, E., & Kalyoncu, S. (2023). Fluorescence-based thermal stability screening is concentration-dependent and varies with protein size. *Front Life Sci RT*, 4(2), 62-67.



Research article

Investigating the relationship between COVID-19 and total oxidative stress and antioxidant capacity in individuals

Aysegül Oglakci Ilhan¹ , Serhat Sirekbasan^{*1} , Filiz Yarimcan² , Ayse Istanbulu Tosun² 

¹ Cankiri Karatekin University, Eldivan Vocational School of Health Services, Department of Medical Laboratory Techniques, 18700, Cankiri, Türkiye

² Istanbul Medipol University, School of Medicine, Department of Medical Microbiology, 34214, Istanbul, Türkiye

Abstract

Free oxygen radicals are effective in the development and progression of viral infections. The aim of this study was to evaluate the levels of oxidative stress in individuals who have been diagnosed with COVID-19, a viral disease nowadays. The study was carried out between March 2021 and June 2021. Blood samples of 50 patients who applied to Medipol University Faculty of Medicine with suspected COVID-19 infection, whose clinical and molecular diagnoses were corrected and were taken for routine evaluations, were included in this study. In the healthy group, 50 serum samples taken before the COVID-19 pandemic were used. Total antioxidant status (TAS) and total oxidant status (TOS) levels were measured, and the data collected were then statistically compared. The TAS level in the COVID-19 group (1.470 ± 0.269) was lower than the healthy group TAS level (1.491 ± 0.286), but it was not statistically significant ($p > 0.05$). The TOS level in COVID-19 group was $13.962 (3.02 \pm 36.35)$ while it was low as $7.925 (1.19 \pm 15.03)$ in the healthy group. The high TOS value in the COVID-19 group was found to be statistically significant compared to the healthy group ($p < 0.05$). Oxidative stress index (OSI) levels, calculated from TOS/TAS , in the COVID-19 group were $9.356 (1.80 \pm 26.54)$ while they were $5.388 (0.98 \pm 10.93)$ in the healthy group. The levels of OSI were found to be significantly higher in the COVID-19 group when compared to the healthy group ($p < 0.05$). The presence of oxidative stress markers in the COVID-19 patients plays an important role in the pathological examination of cell damage. This approach may also pave the way for new therapeutic approaches.

Keywords: Antioxidant; cell damage; COVID-19; oxidative stress

1. Introduction

Coronaviruses (CoVs) are enveloped single-stranded RNA viruses. CoVs can lead to health problems ranging from the ordinary cold to fatal acute respiratory illnesses. After the COVID-19 disease was first discovered in China, there have been reports of it spreading all over the world with an increasing number of patients. The World Health Organization (WHO) proclaimed a COVID-19 infection pandemic because of this outbreak, which resulted in thousands of fatalities (Genc, 2020; Kocyyigit, 2020; Sharma et al., 2021).

The clinical spectrum of COVID-19 infection ranges from moderate respiratory tract illness to severe viral pneumonia and even death (Kocyyigit, 2020). The pathogenesis of COVID-19 infection can be impacted by various factors, such as heightened levels of inflammation, increased oxidative stress, and disruption of immune response regulation. The presence of these factors can potentially induce the excessive release of pro-inflammatory cytokines, which can result in severe complications like acute respiratory distress syndrome (ARDS), shock, and even mortality. This phenomenon, commonly referred to as a “cytokine storm”, can have significant

* Corresponding author.

E-mail address: serhatsirekbasan@gmail.com (S. Sirekbasan).

<https://doi.org/10.51753/flsrt.1210674> Author contributions

Received 27 November 2022; Accepted 02 May 2023

Available online 26 August 2023

2718-062X © 2023 This is an open access article published by Dergipark under the [CC BY](https://creativecommons.org/licenses/by/4.0/) license.

consequences. The excessive and uncontrolled release of cytokines, which can happen in response to a variety of conditions such as infections, autoimmune diseases, and cancer, results in the deadly state known as the cytokine storm. Uncontrolled immune system activation can result in the production of proinflammatory cytokines, which can cause damage to tissues and organs throughout the body. This can result in a range of symptoms, from fever and fatigue to respiratory failure and multiple organ dysfunction syndrome (MODS). The severity of the cytokine storm depends on many factors, including the type and duration of the stimulus, as well as individual differences in immune function. Supportive care and immunomodulatory medicines targeted at reducing inflammation and restoring immunological balance are frequently used in the treatment of cytokine storms. Even though there are still many unanswered questions regarding this complicated condition, ongoing research is shedding light on its underlying processes and prospective therapy targets (Delgado-Roche et al., 2020; Qin et al., 2020).

COVID-19 predominantly impacts the lungs as the primary target organ. The virus enters host cells by binding to Angiotensin-converting enzyme 2 (ACE-2) receptors located on the surface of lung alveolar cells. Subsequently, it propagates along the respiratory system, reaching the lungs. Reproducing in host cells, the virus causes severe inflammation and cellular damage (Uras, 2021).

Several studies have shown that some viruses adopt a strategy to modify the redox balance of a cell. In addition, the initiation of oxidative stress triggered by viral infection has been found to play a crucial role in the activation of innate immune responses aimed at eliminating pathogenic microbes (Kim et al., 2013; Narayanan et al., 2014; Cecchini and Cecchini, 2020).

Neutrophil infiltration and severe hypoxemia are seen in the lungs as a result of the cytokine storm caused by the illness. Organ failure and mortality, as well as oxidative stress and cell damage, are brought on by the respiratory burst mechanism, which generates a fast release of free oxygen species (ROS) in response to inflammation (Celik and Kose, 2020). Oxidative stress occurs when there is an imbalance between the processes of oxidation and antioxidation within the organism. Therefore, oxidative stress and the inflammatory response are strongly connected. Aging, some chronic diseases including diabetes mellitus, cancer, hypertension, and some diseases brought on by RNA viruses like CoV are all affected by oxidative stress (Feng et al., 2017).

Individual measurements of oxidant and antioxidant molecules are used to assess oxidative stress and antioxidant capability. However, complete measuring approaches have lately gained popularity (Erel, 2005). Total oxidant levels (TOS) and total antioxidant levels (TAS) are two metrics used to assess the overall state of oxidative stress in the body. These parameters help gauge the balance between oxidants and antioxidants, providing insights into the oxidative stress levels within the organism (Rampelotto et al., 2023).

The overall antioxidant status of the body is ascertained by TAS testing, whereas the general oxidation state is ascertained by TOS measurement. The ratio of TOS to TAS is used to compute the oxidative stress index (OSI), which measures how well the body is balancing its levels of oxidants and antioxidants (Wu et al., 2017).

Scientific studies suggested a link between oxidative stress, and mortality risk of patients infected severe acute respiratory syndrome coronavirus (SARS-CoV). However, more research is

needed to explore the potential of oxidant and antioxidant stress parameters in patients with COVID-19 (Derouiche, 2020; Zeliger and Kahaner, 2020).

In order to do this, TAS and TOS parameters and contrasted the levels of TAS and TOS in COVID-19 patients with healthy people were assessed.

2. Materials and methods

2.1. Patients

The current study was conducted from March 2021 to June 2021. In this study, 50 blood samples from patients who applied to Istanbul Medipol University's Faculty of Medicine with the suspicion of COVID-19 infection and whose diagnoses were done by Polymerase Chain Reaction (PCR) tests were used. The patients ranged in age from 10 to 88 years old. Patients who were taking antioxidant medication, were pregnant, or had autoimmune, metabolic, or systemic illnesses were excluded from the study. In addition, the healthy group consisted of 50 serum samples collected prior to the COVID-19 pandemic.

Healthy Group (n=50): Comprised of healthy individuals with negative COVID-19 results.

Patients with positive COVID-19 results consisted of the COVID-19 Group (n=50).

2.2. Procedures

The blood samples were obtained from the patients and subsequently subjected to centrifugation at a speed of 3800 rpm for a duration of 10 minutes. Afterward, samples were stored in 500 μ L aliquots at -80°C until the testing time. Then all dissolved at once and studied according to the Erel method (Erel, 2005).

The TOS and TAS levels with RelAssay® Diagnostics kits (Mega Medicine, Gaziantep, Türkiye) were measured based on the colorimetric method. The TOS results were quantified and expressed in terms of $\mu\text{mol H}_2\text{O}_2$ equivalent per liter (H_2O_2 eq/L). The TAS results were presented as mmol/L Trolox equivalent. The percent ratio of TOS to TAS level was accepted as OSI values.

2.3. Statistical analysis

Statistical analyses were performed with IBM SPSS Statistics for Windows, Version 22 package program. For data that followed a normal distribution, Student's t-test was employed, while the Mann-Whitney U test was used for data that deviated from normality. Descriptive statistics were computed, including the mean \pm standard deviation and the median values. The values were accepted as statistically significant when $p < 0.05$.

2.4. Ethics statement

The Ethics Committee of the School of Medicine at Istanbul Medipol University approved the current study (Date: 27.01.2021, Decision no: 2667). All participants received information about the study, and they all voluntarily signed and date the informed consent form. All participants in the trial, including patients and healthy volunteers, verbally consented after being fully informed. The trial was open to patients who hadn't taken any medication before to blood collection.

3. Results

The COVID-19 group consisted of 22 females and 28 males. There were 19 female and 31 male patients in healthy group. Table 1 presents the demographic data of the groups. In the COVID-19 group, the levels of TAS (1.470±0.269) were observed to be slightly lower compared to the healthy group (1.491±0.286). However, this difference was not found to be statistically significant ($p>0.05$), as depicted in Fig. 1.

Table 1
Demographic data of the groups.

Parameters	Healthy Group	COVID-19 Group	p Value
Age (Median)	35 (8-66)	36.5 (10-88)	0.535
Female / Male, n	19/31	22/28	0.544

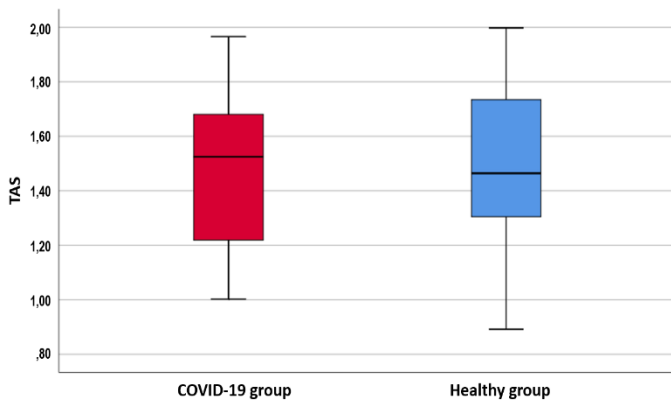


Fig. 1. TAS results.

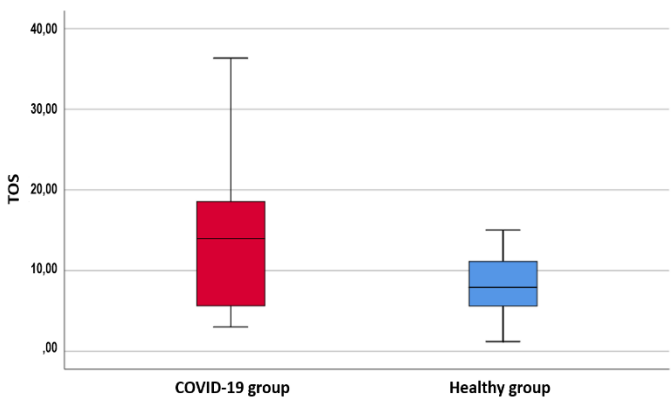


Fig. 2. TOS results.

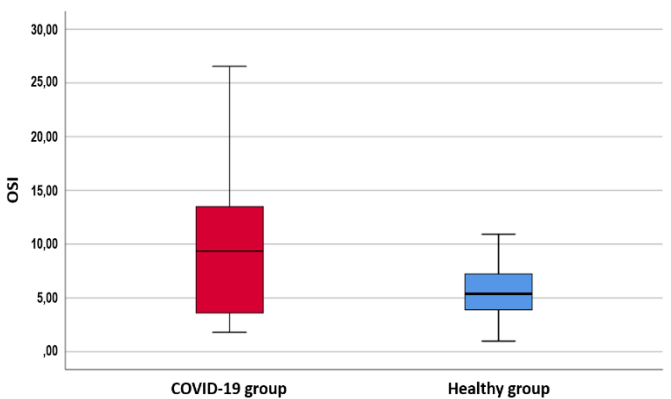


Fig. 3. OSI results.

TOS levels in the COVID-19 group 13.962 (3.02±36.35) were higher than the healthy group 7.925 (1.19±15.03) and

statistically significant ($p<0.05$) (Fig. 2). OSI levels in the COVID-19 group were measured as 9.356 (1.80±26.54) while they were measured as 5.388 (0.98±10.93) in the healthy group and this was statistically significant ($p<0.05$) (Fig. 3).

4. Discussion

This study revealed that COVID-19 patients exhibited significantly higher levels of total oxidative stress and oxidative stress index compared to healthy individuals. The total antioxidant capacity levels in the COVID-19 group were slightly lower than those in the healthy group, but the difference was not statistically significant. These findings indicate that COVID-19 induces oxidative stress within the body, potentially contributing to cellular damage and the progression of the disease.

Additionally, the oxidative stress induced by COVID-19 can result in systemic tissue damage, which is likely to hinder the proper functioning of adaptive immunity (Bakadia et al., 2021). In the prior study conducted by Lin et al., it was reported that a viral protease called SARS-CoV 3CLpro was found to boost ROS generation (Lin et al., 2006). According to the authors, the pathophysiology of SARS-COV is significantly influenced by the rise in ROS generation (Delgado-Roche et al., 2020). One of the significant risk variables linked to COVID-19 severity and mortality includes older age, ethnicity, male sex, low socioeconomic position, hyperglycemia, and obesity. Additionally, connected to elevated oxidative stress are all these risk factors. Due to all these factors is related to a number of characteristics observed in oxidative stress and COVID-19 infection (Chernyak et al., 2020).

In the study conducted by Aykac et al. (2021) the researchers measured the TOS levels in children and adult healthy individuals, as well as individuals with COVID-19. They found that the TOS levels were higher in the children and adults with COVID-19 compared to the healthy groups. This suggests that individuals with COVID-19 may experience higher levels of oxidative stress compared to healthy individuals.

Recently, researchers have shown that COVID-19 disrupts mitochondrial homeostasis. This process also causes oxidative damage in COVID-19 patients. Dagli et al. (2022) reported that the OS parameters, TAS, TOS, MDA and PC levels increased in COVID-19 patients. The elevated levels of TOS and OSI detected in patients with COVID-19 underscore the significance of antioxidant therapy as a prospective therapeutic strategy for addressing COVID-19. Antioxidants play a crucial role in neutralizing free radicals and reducing oxidative stress within the body. By counteracting the harmful effects of free radicals, antioxidants help maintain a balance between oxidation and antioxidation, thus mitigating the detrimental impact of oxidative stress. Therefore, the use of antioxidants may help to prevent or alleviate the cell damage caused by the virus. In healthy people, a boost in antioxidant defense balances off the excess ROS generation. Red blood cells peroxide when ROS generation is improperly managed in individuals with defective redox equilibrium (RBC). According to the study by Laforge et al., increased generation of oxidative stress may contribute to alveolar damage, thrombosis, and dysregulation of red blood cells in individuals with COVID-19. Their research suggests that the elevated oxidative stress levels observed in COVID-19 patients could play a role in these pathological processes (Laforge et al., 2020). According to Muhammad et al., COVID-19 patients had low plasma levels of the antioxidant vitamins A,

C, and E, but COVID-19 patients had high amounts of malondialdehyde, one of the indicators of oxidative stress. To counteract the damaging effects of free radicals, antioxidant levels are likely to decline in COVID-19 patients (Muhammad et al., 2021).

It is important to remember that ROS generation brought on by viral infection cannot be seen as a single damaging agent. Additionally, ROS is necessary for the phagocytosis of viruses by immune cells and for signal transmission between different immune cells.

Redox homeostasis for viral infection response should thus be offered. Oxidative stress and cell and tissue damage emerge when this equilibrium shifts in favor of excessive ROS generation or a deficit in the antioxidant defense system (Chernyak et al., 2020).

In general, oxidative stress impacts the development of illness in nearly all patients with viral infections, and these individuals can respond to the viral infection by maintaining their redox balance (Baloch et al., 2020).

References

- Aykac, K., Ozsurekci, Y., Yayla, B. C. C., Gurlevik, S. L., Oygur, P. D., Bolu, N. B., ... & Ceyhan, M. (2021). Oxidant and antioxidant balance in patients with COVID-19. *Pediatric Pulmonology*, 56(9), 2803-2810.
- Bakadia, B. M., Boni, B. O. O., Ahmed, A. A. Q., & Yang, G. (2021). The impact of oxidative stress damage induced by the environmental stressors on COVID-19. *Life Sciences*, 264, 118653.
- Baloch, S., Baloch, M. A., Zheng, T., & Pei, X. (2020). The coronavirus disease 2019 (COVID-19) pandemic. *The Tohoku Journal of Experimental Medicine*, 250(4), 271-278.
- Celik, D., & Kose, S. (2020). Erişkinlerde COVID-19: Klinik bulgular. *Tepecik Eğitim ve Araştırma Hastanesi Dergisi*, 30, 43-48.
- Cecchini, R., & Cecchini, A. L. (2020). SARS-CoV-2 infection pathogenesis is related to oxidative stress as a response to aggression. *Medical Hypotheses*, 143, 110102.
- Chernyak, B. V., Popova, E. N., Prikhodko, A. S., Grebenchikov, O. A., Zinovkina, L. A., & Zinovkin, R. A. (2020). COVID-19 and oxidative stress. *Biochemistry*, 85(12), 1543-1553.
- Dagli, S. N., Ozgocer, T., Celik, H., Taskin, S., Taskin, A., & Ceylan, M. R. (2022). Long-term investigation of total oxidant and antioxidant levels in COVID-19 patients. *Journal of Harran University Medical Faculty*, 19(1), 176-183.
- Delgado-Roche, L., & Mesta, F. (2020). Oxidative stress as key player in severe acute respiratory syndrome coronavirus (SARS-CoV) infection. *Archives of Medical Research*, 51(5), 384-387.
- Derouiche, S. (2020). Oxidative stress associated with SARS-Cov-2 (COVID-19) increases the severity of the lung disease-a systematic review. *Journal of Infectious Diseases and Epidemiology*, 6(3), 121-126.
- Erel O. (2005). A new automated colorimetric method for measuring total oxidant status. *Clinical Biochemistry*, 38(12), 1103-1111.
- Feng, J., Yang, Y., Wang, D., Tang, J., Xie, G., & Fan, L. (2017). Relationship between oxidative stress in patients with HBV-induced liver disease and HBV genotype/drug-resistant mutation. *Frontiers in Laboratory Medicine*, 1(4), 211-216.
- Genc, B. N. (2020). Critical management of COVID-19 pandemic in Turkey. *Frontiers in Life Sciences and Related Technologies*, 1(2), 69-73.
- Kim, H. J., Kim, C. H., Ryu, J. H., Kim, M. J., Park, C. Y., Lee, J. M., Holtzman, M. J., & Yoon, J. H. (2013). Reactive oxygen species induce antiviral innate immune response through IFN- λ regulation in human nasal epithelial cells. *American Journal of Respiratory Cell and Molecular Biology*, 49(5), 855-865.
- Kocyyigit, A. (2020). Is high dose intravenous vitamin C safe to use in SARS-CoV-2 treatment? *Bezmialem Science*, 8(3), 126-130.
- Laforge, M., Elbim, C., Frère, C., Hémedi, M., Massaad, C., Nuss, P., Benoliel, J. J., & Becker, C. (2020). Tissue damage from neutrophil-induced oxidative stress in COVID-19. *Nature Reviews. Immunology*, 20(9), 515-516.
- Lin, C. W., Lin, K. H., Hsieh, T. H., Shiu, S. Y., & Li, J. Y. (2006). Severe acute respiratory syndrome coronavirus 3C-like protease-induced apoptosis. *FEMS Immunology and Medical Microbiology*, 46(3), 375-380.
- Muhammad, Y., Kani, Y. A., Iliya, S., Muhammad, J. B., Binji, A., El-Fulaty Ahmad, A., Kabir, M. B., Umar Bindawa, K., & Ahmed, A. (2021). Deficiency of antioxidants and increased oxidative stress in COVID-19 patients: A cross-sectional comparative study in Jigawa, Northwestern Nigeria. *SAGE Open Medicine*, 9, 2050312121991246.
- Narayanan, A., Amaya, M., Voss, K., Chung, M., Benedict, A., Sampey, G., Kehn-Hall, K., Luchini, A., Liotta, L., Bailey, C., Kumar, A., Bavari, S., Hakami, R. M., & Kashanchi, F. (2014). Reactive oxygen species activate NF κ B (p65) and p53 and induce apoptosis in RVFV infected liver cells. *Virology*, 449, 270-286.
- Qin, C., Zhou, L., Hu, Z., Zhang, S., Yang, S., Tao, Y., Xie, C., Ma, K., Shang, K., Wang, W., & Tian, D. S. (2020). Dysregulation of immune response in patients with coronavirus 2019 (COVID-19) in Wuhan, China. *Clinical Infectious Diseases*, 71(15), 762-768.
- Rampelotto, P. H., Giannakos, N. R. O., Mena Canata, D. A., Pereira, F. D., Hackenhaar, F. S., Pereira, M. J. R., & Benfato, M. S. (2023). Oxidative stress and antioxidant defense in the brain of bat species with different feeding habits. *International Journal of Molecular Sciences*, 24(15), 12162.
- Sharma, A., Ahmad Farouk, I., & Lal, S. K. (2021). COVID-19: A review on the novel coronavirus disease evolution, transmission, detection, control and prevention. *Viruses*, 13(2), 202.
- Uras, M. E. (2021). *In silico* comparative analysis of SARS-CoV-2 nucleocapsid (N) protein using bioinformatics tools. *Frontiers in Life Sciences and Related Technologies*, 2(1), 1-9.
- Wu, R., Feng, J., Yang, Y., Dai, C., Lu, A., Li, J., Liao, Y., Xiang, M., Huang, Q., Wang, D., & Du, X. B. (2017). Significance of serum total oxidant/antioxidant status in patients with colorectal cancer. *PLoS One*, 12(1), e0170003.
- Zeliger, H. I., & Kahaner, H. (2020). Can the oxidative stress index predict the severity of COVID-19? COVID-19 perspective. *European Journal of Medical and Health Sciences*, 2(2), 1-5.

Cite as: Oglakci Ilhan, A., Sirekbasan, S., Yarimcan, F., & Istanbulu Tosun, A. (2023). Investigating the relationship between COVID-19 and total oxidative stress and antioxidant capacity in individuals. *Front Life Sci RT*, 4(2), 68-71.



Research article

Identification and verification of promising diagnostic genes in bisphenol A-associated breast cancer development via *in silico* analysis

Mervenur Akkus¹ , Hamid Ceylan^{*1} 

¹ Ataturk University, Faculty of Science, Department of Molecular Biology and Genetics, 25240, Erzurum, Türkiye

Abstract

Lifestyle patterns and exposure to toxic chemicals or environmental pollutants are the strongest risk factors for the chances of developing breast cancer, the leading and most lethal form of cancer in women. Bisphenol A (BPA), found in various consumer products, is known to deregulate multiple cellular signaling pathways, but its effect on cancer initiation and development in breast tissue has not yet been fully elucidated. Therefore, the identification of hub drivers is necessary to understand the molecular mechanisms underlying BPA-related malignancy and may help determine novel diagnosis and treatment strategies. This work aims at elucidating the molecular actors and mechanisms of action involved in BPA-induced breast cancer development using a bioinformatics analysis approach. A microarray dataset suitable for the study purposes was obtained from the publicly available Gene Expression Omnibus (GEO) repository, followed by DEG (differentially expressed genes) extraction, enrichment, and protein-protein interaction analyses to identify the hub genes. Expressional patterns, prognostic potentials, and immune infiltration levels of identified targets were tested and validated *in silico* using GEPIA2 and KM-plotter tools. According to PPI network results, *CCNA2* and *CCNB1* were identified as critical hub genes. Validation analyses clearly indicated that the identified genes are extremely critical in BPA-associated breast cancer processes. Findings from this study revealed that *CCNA2* and *CCNB1*, two cell cycle signaling-related hub genes that are overexpressed as a consequence of BPA exposure, are strongly associated with breast cancer.

Keywords: Biomarker; BPA; breast cancer; cell cycle signaling; DEGs

1. Introduction

Breast cancer is a lethal and common type of cancer in women and affects daily life in different ways. The disease emerges in the epithelium of the lobules or ducts (85%) in the glandular parts of the breast (Nardin et al., 2020). Initially, cancer has minimal potential for spread and generally causes no symptoms. However, cancer may progress over time and invade the surrounding breast tissue. Firstly, it spreads to the lymph nodes and then to other organs in the body (Zhou et al., 2021). World Health Organization (WHO) reports and GLOBOCAN cancer incidence and mortality estimates revealed that this cancer accounts for 11.7% of all cancer cases, with

approximately 2.5 million cases in 2020 (Sung et al., 2021; WHO, 2023). Since it is a polygenic and multifactorial cancer, it includes complex mechanisms, signaling pathways, and cellular activities. The most critical issue in the treatment of the disease is diagnosing it at advanced stages due to the lack of sensitive biomarkers and effective treatment (Pei et al., 2020). Therefore, identifying the critical factors for this complicated type of cancer is very important, both to determine valuable diagnostics actors that can also be used in the treatment and to fully understand the molecular mechanism underlying the malignancy.

Bisphenol A (BPA) is an intermediate compound with a massive production volume worldwide, especially in

* Corresponding author.

E-mail address: hamid.ceylan@atauni.edu.tr (H. Ceylan).

<https://doi.org/10.51753/flsrt.1223888> Author contributions

Received 25 December 2022; Accepted 23 May 2023

Available online 26 August 2023

2718-062X © 2023 This is an open access article published by Dergipark under the [CC BY](https://creativecommons.org/licenses/by/4.0/) license.

polycarbonate and epoxy manufacture (Fauconnier et al., 2023). It is widely preferred in daily used storage containers, bottles, and other packaging items that are frequently used in daily life (Dehdashti et al., 2023). BPA can be released into the environment during the entire production and disposal processes of these products. The United States Environmental Protection Agency (EPA) statistics show annual environmental BPA leaks are almost 400,000 tons (EPA, 2023).

Preclinical studies have found that bisphenol exposure elevates breast cancer risk (Stillwater et al., 2020; Kwon, 2022). Novel research has shown that endocrine-disrupting chemicals (EDCs), including bisphenols, trigger breast cancer-associated genes and cell proliferation via binding to estrogen receptors (ERs) (Castillo-Sanchez et al., 2020). Impairments in the endocrine system in complex diseases such as birth defects and obesity caused by BPA have been partially clarified (Priyadarshini et al., 2023). However, it is unclear how BPA affects the onset and progression of cancer in the breast. Therefore, understanding the exact biological effects of endocrine disruptors is essential. This study aims to identify hub factors and pathways involved in BPA-associated breast cancer formation and progression via a bioinformatics approach.

2. Materials and methods

2.1. Collection and pre-processing of transcriptomic data

The mRNA expression dataset (GSE32158), which includes MCF-10F cells exposed to 10 μ M BPA for two weeks and non-treated cells, was obtained from the GEO repository (Barrett et al., 2013) of NCBI. Next, DEGs between BPA-treated and control group cells were identified using the GEO2R web tool (GEO2R, 2023). Next, DEGs between BPA-treated and control cells were identified according to $|\log_{2}FC| > 2.0$ and p -value < 0.05 criteria using the GEO2R web tool (Fig. 1).

2.2. Enrichment analyses of the DEGs

To identify the biological and molecular functional processes and significantly enriched pathways of the DEGs, the DAVID tool was used (Huang et al., 2009; DAVID, 2023).

2.3. Protein-protein interaction (PPI) network analysis

Co-expression relationship between DEGs was determined through the PPI network created using STRING (Jensen et al., 2009; STRING, 2023). The confidence score cutoff value was set at 0.7. Then, the cytoHubba plug-in of Cytoscape (Shannon et al., 2003) was used to extract the hub genes using five widely preferred algorithms: Maximal Clique Centrality (MCC), Maximum Neighborhood Component (MNC), Degree, Eccentricity, and Closeness. The first fifteen genes of each algorithm result were ranked, and aligned genes were chosen as hub genes.

2.4. Data validation

The mRNA profiles of the core genes between tumor and healthy tissues in breast invasive carcinoma (BRCA) were verified using different sources and tools. Cumulative mRNA expressions of the hub genes in breast cancer patients and healthy individuals were analyzed using the GEPIA2 platform (Tang et al., 2019; GEPIA2, 2023) was used.

The association between the expression of hub genes and the clinical stage of the disease was analyzed using the UALCAN web portal (Chandrashekar et al., 2017; UALCAN, 2023) and the prognostic outputs of these genes on the overall survival of breast cancer patients were evaluated using the KM-plotter platform (Gyorffy, 2021; KM-plotter, 2023). The expression correlations of hub genes in breast cancer and the tumor infiltration level of immune cells were visualized by the TIMER2.0 database (Li et al., 2020; TIMER2.0, 2023). Finally, to determine whether the identified hub genes were among the genes interacting with BPA, the CTD database was used (Davis et al., 2021; CTD, 2023).

3. Results

3.1. DEGs

Based on the findings, a total of 1814 DEGs (976 up- and 838 down-regulated) were identified ($|\log_{2}FC| > 2$ and $p < 0.05$).

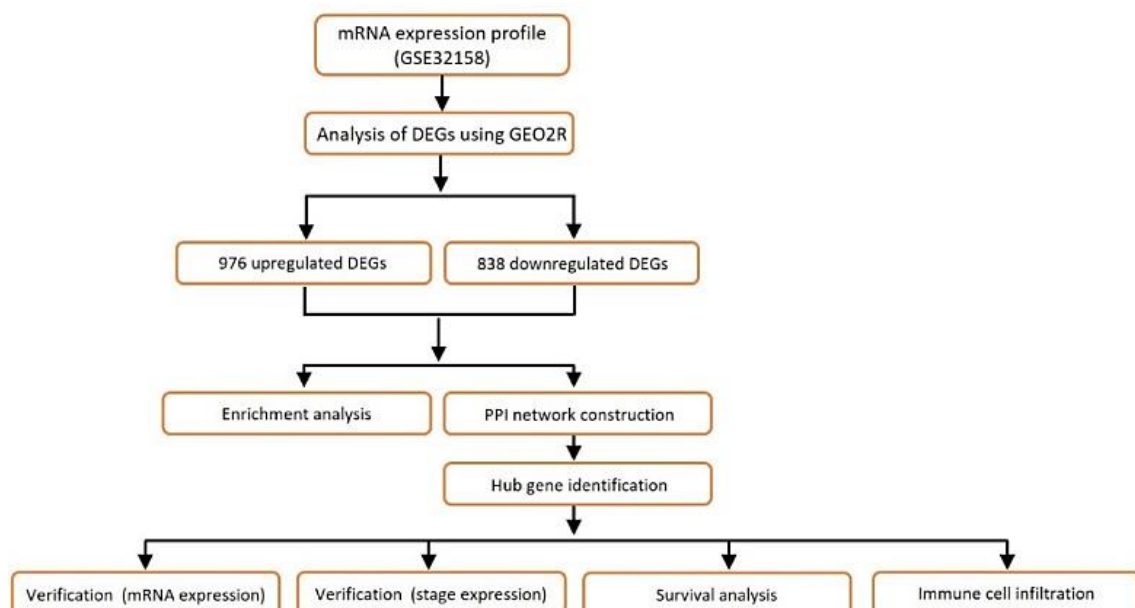


Fig. 1. The overall workflow of the study.

3.2. Functional characterization of DEGs

To further investigate the biological themes and pathways including the DEGs, GO and KEGG pathway enrichment analyses were performed. The first fifty down and upregulated DEGs were used for this analysis. Based on the DEGs annotation, it was found that the upregulated genes were significantly enriched in several GO terms, such as regulation of cell proliferation, cell surface, and DNA helicase activity. Downregulated genes were significantly enriched in transport, oxidation-reduction processes, and cytokine receptor activity. According to pathway enrichment results, while upregulated DEGs are importantly enriched in ECM-receptor interaction, downregulated DEGs are enriched in the complement and coagulation cascades (Supplementary Table 1 and 2).

3.3. Protein interaction network and hub gene detection

The PPI network constructed using the STRING (Fig. 2) was further analyzed with Cytoscape software. Next, network properties were analyzed by MCC, MNC, Degree, EcCentricity, and Closeness algorithms of the Cytohubba plug-in of Cytoscape. The genes that are the intersection of the first-ranked 15 genes with the highest score in these five algorithms were identified through the Venn diagram. Finally, *CCNA2* and *CCNB1* were identified as hub genes (Table 1 and Fig. 3).

3.4. Validation and analysis of hub genes

Firstly, GEPIA2 was used to confirm the mRNA expression patterns of two genes. It was determined that the mRNA levels of the two identified genes were notably elevated in tumor tissues compared to healthy tissues (Fig. 4a and Fig. 4d). Then, subgroup analysis was performed using UALCAN to uncover the expression changes of *CCNA2* and *CCNB1* genes in tumor stages. The results revealed that the relative expression of *CCNA2* and *CCNB1* increased significantly in advanced tumor stages (Fig. 4b and Fig. 4e). To further investigate the clinical importance and prognostic impacts of these hub genes in breast cancer, overall survival (OS) analysis was performed using the KM-plotter. The results showed that an increased *CCNA2* expression (HR 1.48 [1.34–1.64], $P=1.9e-14$) and *CCNB1* (HR 1.89 [1.71–2.1], $P<1e-16$) was significantly related to a poor OS in patients diagnosed with cancer (Fig. 4c and Fig. 4f).

The hub gene expression with immune infiltration level in breast cancer correlation was detected using the TIMER gene module. Results showed that there was a positive correlation between the expression of *CCNA2* and the infiltration of purity, B cells, CD4+ T cells, CD8+ T cells, dendritic cells, and neutrophils (Fig. 5a). In addition, there was a correlation between the *CCNB1* expression and the infiltration of purity, B cells, and neutrophils (Fig. 5b).

These findings clearly propose that *CCNA2* and *CCNB1*

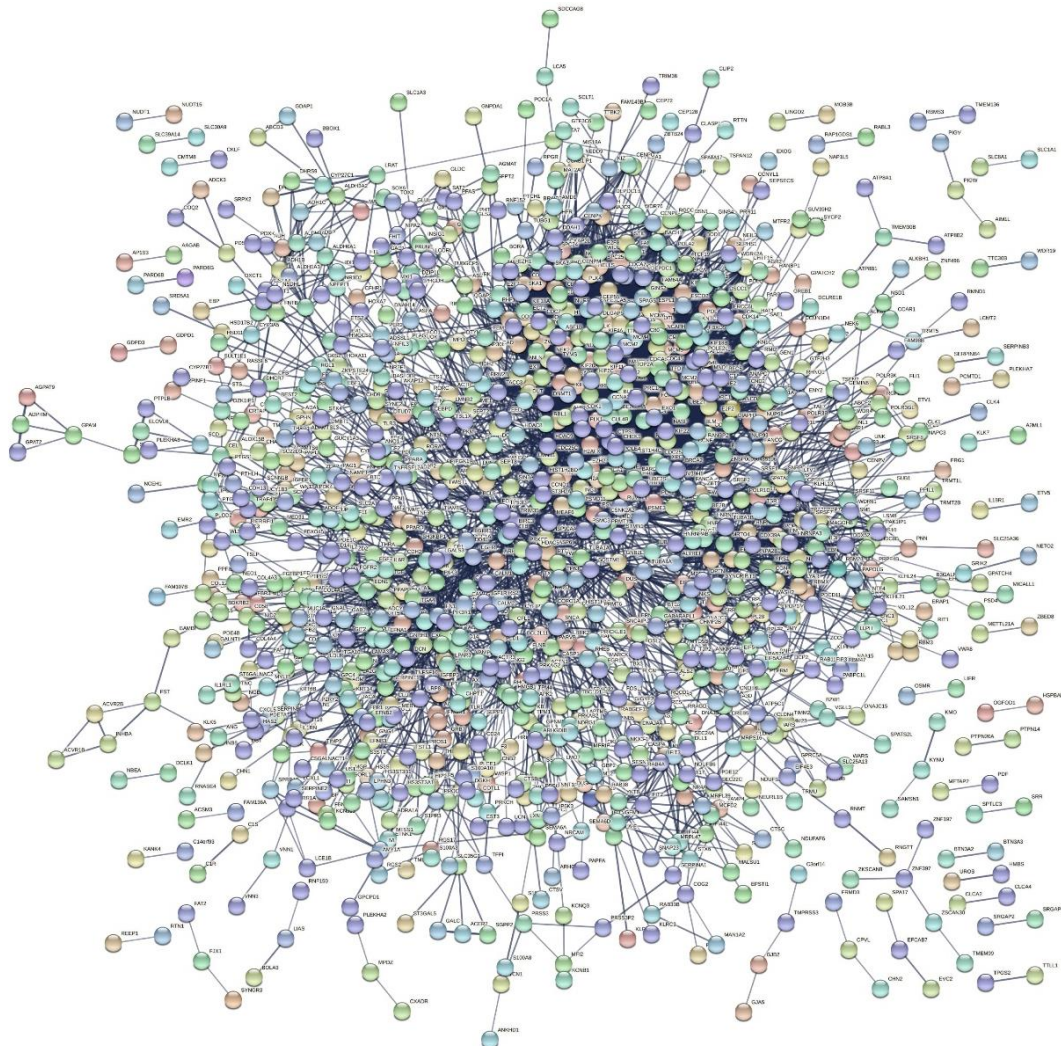


Fig. 2. PPI network of DEGs constructed by STRING database.

Table 1

Top 15 genes ranked by five different cytoHubba computational algorithms. The intersection genes are highlighted in bold.

Genes	MCC Score	Genes	MNC Score	Genes	Degree Score	Genes	EcCentricity Score	Genes	Closeness Score
<i>CCNB1</i>	9,22E+28	<i>CDK1</i>	181.0	<i>CDK1</i>	181.0	<i>EGFR</i>	0.15373	<i>CDK1</i>	516.93
<i>CCNA2</i>	9,22E+28	<i>CCNB1</i>	155.0	<i>CCNB1</i>	156.0	<i>CCNB1</i>	0.13177	<i>CCNB1</i>	491.55
<i>AURKB</i>	9,22E+28	<i>CCNA2</i>	154.0	<i>CCNA2</i>	154.0	<i>CCNA2</i>	0.13177	<i>CCNA2</i>	489.26
<i>BUB1</i>	9,22E+28	<i>BUB1</i>	149.0	<i>BUB1</i>	149.0	<i>BIRC5</i>	0.13177	<i>AURKB</i>	476.64
<i>PLK1</i>	9,22E+28	<i>BUB1B</i>	143.0	<i>NCAPG</i>	144.0	<i>CHEK1</i>	0.13177	<i>HSP90AA1</i>	473.56
<i>BUB1B</i>	9,22E+28	<i>AURKB</i>	142.0	<i>BUB1B</i>	143.0	<i>TYMS</i>	0.13177	<i>BUB1</i>	473.41
<i>CHEK1</i>	9,22E+28	<i>NCAPG</i>	142.0	<i>AURKB</i>	143.0	<i>BRCA1</i>	0.13177	<i>EGFR</i>	471.33
<i>AURKA</i>	9,22E+28	<i>TOP2A</i>	140.0	<i>KIF11</i>	142.0	<i>CDC25C</i>	0.13177	<i>ACTB</i>	470.02
<i>TOP2A</i>	9,22E+28	<i>KIF11</i>	140.0	<i>TOP2A</i>	140.0	<i>ACTB</i>	0.13177	<i>PLK1</i>	469.49
<i>BRCA1</i>	9,22E+28	<i>CCNB2</i>	136.0	<i>CCNB2</i>	136.0	<i>HSP90AA1</i>	0.13177	<i>BUB1B</i>	468.55
<i>CCNB2</i>	9,22E+28	<i>MAD2L1</i>	131.0	<i>MAD2L1</i>	131.0	<i>CCND1</i>	0.13177	<i>CHEK1</i>	467.38
<i>NCAPG</i>	9,22E+28	<i>CDC20</i>	129.0	<i>CDC20</i>	129.0	<i>PIK3R1</i>	0.13177	<i>AURKA</i>	467.30
<i>RRM2</i>	9,22E+28	<i>NDC80</i>	126.0	<i>NDC80</i>	126.0	<i>H2AFX</i>	0.13177	<i>TOP2A</i>	464.78
<i>KIF11</i>	9,22E+28	<i>TTK</i>	124.0	<i>PLK1</i>	125.0	<i>FN1</i>	0.13177	<i>BRCA1</i>	463.13
<i>MAD2L1</i>	9,22E+28	<i>ASPM</i>	123.0	<i>AURKA</i>	125.0	<i>H2AFV</i>	0.13177	<i>CCNB2</i>	462.39

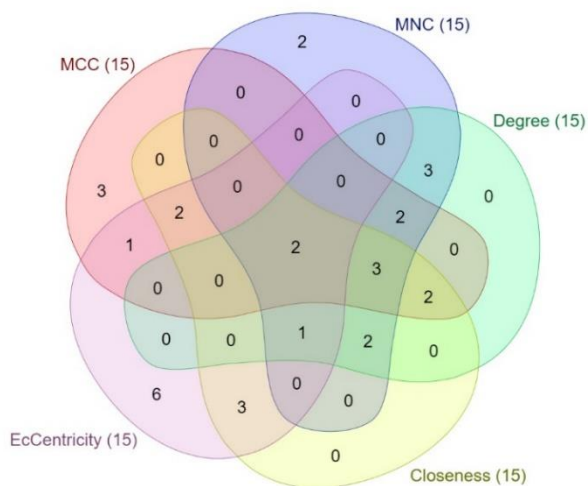


Fig. 3. Venn diagram of the intersecting genes derived using five algorithms.

may play an essential role in immune cell infiltration in patients with breast cancer. It is well that known genes with co-expression patterns are co-regulated or functionally related (Kustatscher et al., 2017). Therefore, to determine the mRNA expression correlation of hub genes in breast cancer the correlation module of TIMER was used. Consequently, it was found that *CCNA2* and *CCNB1* expressions were highly correlated with each other in BRCA (Fig. 6a). Finally, the CTD analysis tool MyGeneVenn was used to determine whether hub genes are among the genes regulated in response to BPA. Intersection analysis of a set of genes curated by CTD and hub genes from this study showed that *CCNA2* and *CCNB1* were predicted to be targeted by BPA (Fig. 6b).

4. Discussion

The causes of polygenic diseases are blurry due to their complex nature, which complicates the detection of the contributing factors (Ceylan et al., 2019; Ritchie et al., 2021). Therefore, changes in the whole genome should be considered to elucidate the pathophysiology of multifactorial diseases such as breast cancer and thus determine effective therapy strategies

(Ceylan, 2022). Identification of central genes through the bioinformatics-based transcriptome analysis approach is widely recognized in the scientific community and provides a molecular basis for related biological questions (Ceylan, 2021). The present study aimed to determine the carcinogenic properties of BPA in breast cancer and accurate targets for future therapy through the analysis of transcriptome data from BPA-treated human breast epithelial cells MCF-10F. Based on the integrated bioinformatics analysis, two hub genes (*CCNA2* and *CCNB1*) have been identified in this study. The mRNA expression of these two genes was dysregulated (over 12 and 32-fold changes, respectively) in the BPA-treated MCF-10F cells compared to non-treated cells.

The cell cycle is regulated tightly because perturbations in this operation can lead to crucial complications such as tumor development mediated by uncontrolled cell division and inappropriate cell proliferation (Pekarek et al., 2023). Dysregulation of the expression of related drivers that control the transitional stages of the cell cycle is well-documented in multiple cancers (García-Gutiérrez et al., 2019; Yesilkent and Ceylan, 2022). CDKs (cyclin-dependent kinases) are regulate cell cycle checkpoints in response to intracellular and extracellular signals (Niu et al., 2019). As a result, it is not surprising that abnormalities or impairment of CDKs and CDK-mediated pathways are characteristic of cancers and initiate a chain of events that prime cancer (Ding et al., 2020). Recent research has shown that these cyclins are raised in breast cancer and are related with worse clinical outcomes (Cai et al., 2023). *CCNA2* (also known as cyclinA2) is a type of cyclin protein and is expressed in nearly all tissues (Zhang et al., 2023). Numerous reports have reported that *CCNA2* is overexpressed in different cancer types and is markedly related with bad prognosis (Dong et al., 2019). Similarly, unscheduled expression of *CCNB1* (cyclin B1) has also been shown to be associated with uncontrolled cell-cycle progression in several cancers (Zuryn et al., 2019). Therefore, targeting these factors, especially in breast cancer, can be an ideal strategy to prevent tumor development and increase the effectiveness of chemotherapy.

Although the relationship of BPA with global health challenges such as diabetes and heart disorders has been largely proven, the mechanisms and key drivers of BPA-induced breast cancer are still not fully elucidated. Most EDCs stimulate

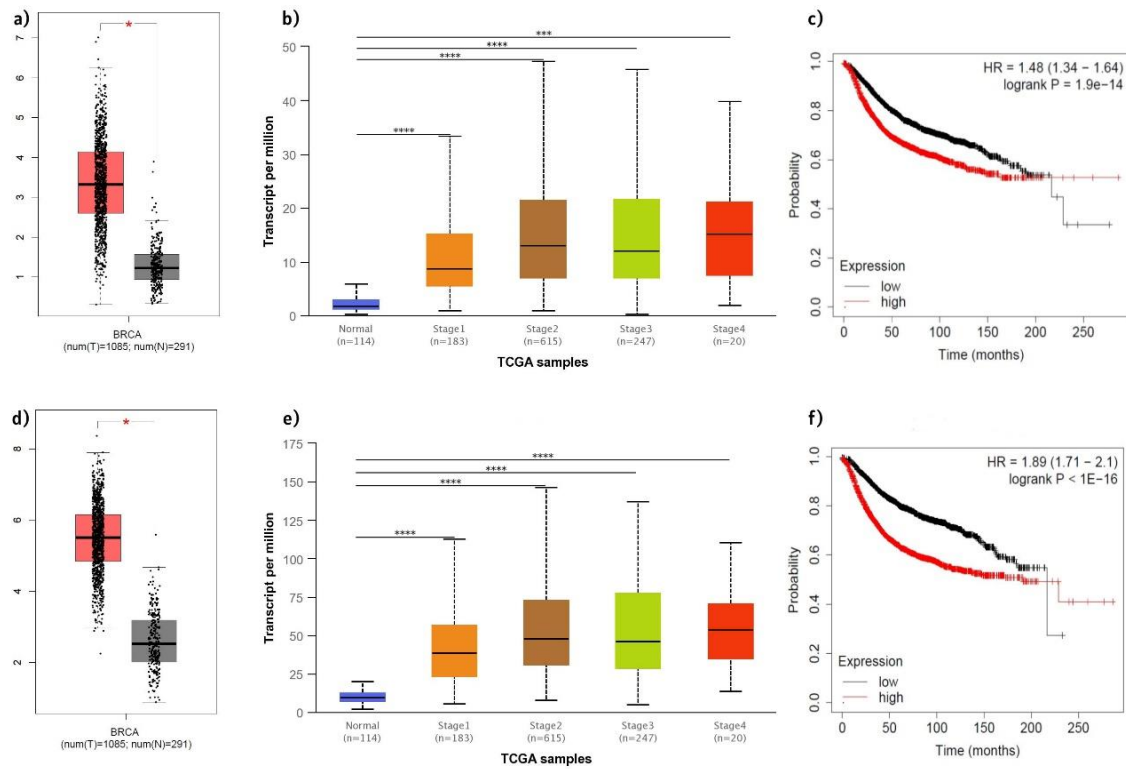


Fig. 4. The expression validation and analysis of hub genes. The expression profiles of *CCNA2* (a) and *CCNB1* (d) genes in breast cancer within GEPIA database. Red asterisk on top of the boxplot denotes the statistically significant difference. mRNA expression patterns of the hub genes in breast cancer patients with cancer stages (b-e). *p*-values < *0.05, **0.01, ***0.001, ****0.0001. Overall survival (OS) analysis of hub genes in BRCA patients (c-f).

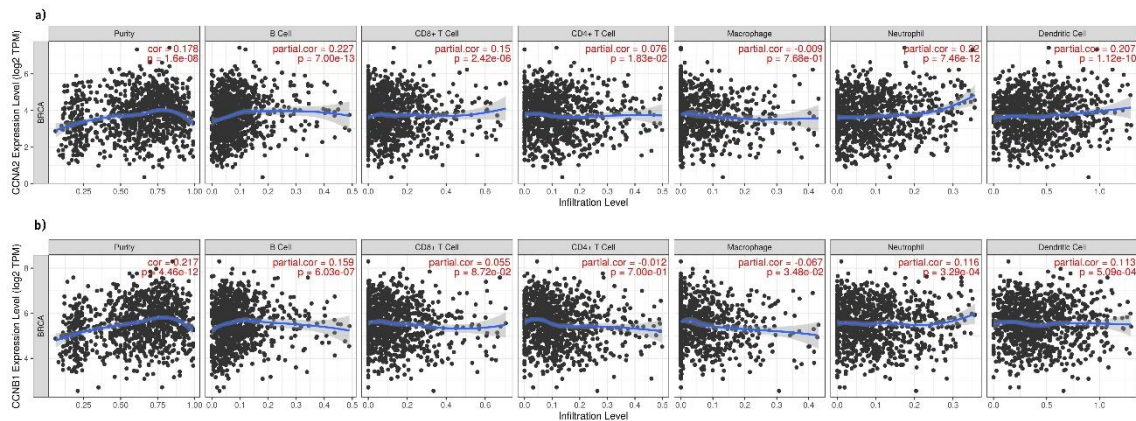


Fig. 5. *CCNA2* (a) and *CCNB1* (b) expressional correlation and abundance of tumor-infiltrating immune cells.

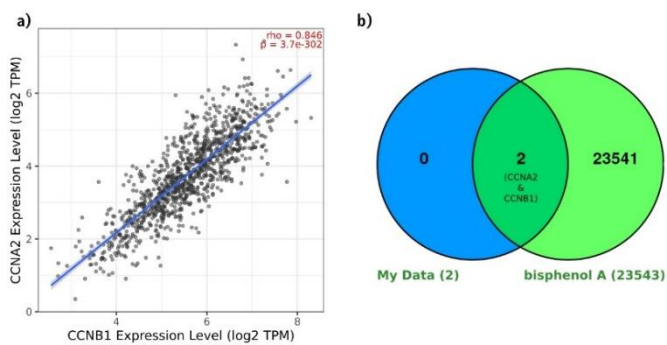


Fig. 6. Correlation of mRNA expression of *CCNA2* and *CCNB1* in patients with breast invasive carcinoma (a). Comparative toxicogenomic analysis and target verification in response to BPA (b).

estrogen-related responses by binding to estrogen receptors

(ERs), resulting in gene expression remodeling in the target tissue (Bondar et al., 2009). Among EDCs, BPA, as an estrogenic compound that has shared structural characteristics with ERs, can stimulate cellular responses and cell function through its strong estrogenic activity and can cause very critical undesirable effects on the health (Almeida et al., 2018).

Several reports have revealed that due to its endocrine disrupting nature, BPA is associated with numerous principal non-communicable diseases (NCDs) such as obesity (Hong et al., 2023), infertility (Yadav et al., 2023), diabetes (Hwang et al., 2018), and cancer (Li et al., 2023a).

BPA's potential influence on cancer initiation and progression, especially in estrogen-related cases, is intriguing, stemming from research connecting BPA exposure to intricate molecular pathways in cancer development and spread (Ogawa et al., 2023). It has been demonstrated that normal ER signaling supports benign functions such as differentiation and

development in healthy breast tissue. However, numerous studies have proven that the abnormal activity of ER signaling triggers tumor formation in breast tissue (Xue et al., 2019). ER-alpha (α) and ER-beta (β) are two estrogen receptor subgroups that are thought to be the primary targets of BPA (Li et al., 2023b). A study reported that ER α moderates cell proliferation in breast cancer by modulating the cell cycle checkpoints (JavanMoghadam et al., 2016). Another report has indicated that the ER α agonistic activity of BPA triggers the development of ER-dependent cancer by activating the estrogen response element (ERE) promoter (Tillett, 2009). Taken together, tuning both ER signaling, and cell cycle control appear to be synchronized mechanisms underlying the biological effect exerted by BPA in breast cancer formation.

References

- Almeida, S., Raposo, A., Almeida-Gonzalez, M., & Carrascosa, C. (2018). Bisphenol A: Food exposure and impact on human health. *Comprehensive Reviews in Food Science and Food Safet*, 17(6), 1503-1517.
- Barrett, T., Wilhite, S. E., Ledoux, P., Evangelista, C., Kim, I. F., Tomashevsky, M., ... & Soboleva, A. (2012). NCBI GEO: archive for functional genomics data sets-update. *Nucleic Acids Research*, 41(D1), D991-D995.
- Bondar, G., Kuo, J., Hamid, N., & Micevych, P. (2009). Estradiol-induced estrogen receptor-alpha trafficking. *Journal of Neuroscience*, 29(48), 15323-15330.
- Cai, Z., Wang, J., Li, Y., Shi, Q., Jin, L., Li, S., ... & Liu, Q. (2023). Overexpressed cyclin D1 and CDK4 proteins are responsible for the resistance to CDK4/6 inhibitor in breast cancer that can be reversed by PI3K/mTOR inhibitors. *Science China Life Sciences*, 66(1), 94-109.
- Castillo-Sanchez, R., Ramirez-Ricardo, J., Martinez-Baeza, E., Cortes-Reynosa, P., Candanedo-Gonzales, F., Gomez, R., & Salazar, E. P. (2020). Bisphenol A induces focal adhesions assembly and activation of FAK, Src and ERK2 via GPER in MDA-MB-231 breast cancer cells. *Toxicology In Vitro*, 66, 104871.
- Ceylan, H. (2021). Identification of hub genes associated with obesity-induced hepatocellular carcinoma risk based on integrated bioinformatics analysis. *Medical Oncology*, 38(6), 63.
- Ceylan, H. (2022). Integrated bioinformatics analysis to identify alternative therapeutic targets for Alzheimer's disease: Insights from a synaptic machinery perspective. *Journal of Molecular Neuroscience*, 72(2), 273-286.
- Ceylan, H., Budak, H., Kocpinar, E. F., Baltaci, N. G., & Erdogan, O. (2019). Examining the link between dose-dependent dietary iron intake and Alzheimer's disease through oxidative stress in the rat cortex. *Journal of Trace Elements in Medicine and Biology*, 56, 198-206.
- Chandrashekar, D. S., Bashel, B., Balasubramanya, S. A. H., Creighton, C. J., Ponce-Rodriguez, I., Chakravarthi, B., & Varambally, S. (2017). UALCAN: A Portal for facilitating tumor subgroup gene expression and survival analyses. *Neoplasia*, 19(8), 649-658.
- CTD, (2023). Official Website of The Comparative Toxicogenomics Database, <https://ctdbase.org/>, Last accessed on August 10, 2023.
- DAVID, (2023). Official Website of The Database for Annotation, Visualization and Integrated Discovery, <https://david.ncifcrf.gov/>, Last accessed on August 10, 2023.
- Davis, A. P., Grondin, C. J., Johnson, R. J., Sciaky, D., Wieggers, J., Wieggers, T. C., & Mattingly, C. J. (2021). Comparative Toxicogenomics Database (CTD): update 2021. *Nucleic Acids Research*, 49(D1), D1138-D1143.
- Dehdashti, B., Nikaen, M., Amin, M. M., & Mohammadi, F. (2023). Health risk assessment of exposure to Bisphenol A in polymeric baby bottles. *Environmental Health Insights*, 17, 11786302231151531.
- Ding, L., Cao, J., Lin, W., Chen, H., Xiong, X., Ao, H., Yu, M., Lin, J., & Cui, Q. (2020). The roles of cyclin-dependent kinases in cell-cycle progression and therapeutic strategies in human breast cancer. *International Journal of Molecular Sciences*, 21(6), 1-28.
- Dong, S., Huang, F., Zhang, H., & Chen, Q. (2019). Overexpression of BUB1B, CCNA2, CDC20, and CDK1 in tumor tissues predicts poor survival in pancreatic ductal adenocarcinoma. *Bioscience Reports*, 39(2), BSR20182306.
- EPA. (2023). United States Environmental Protection Agency. <https://www.epa.gov/>. Last accessed on August 10, 2023.
- Fauconnier, M. B., Albert, C., Tondreau, A., Maumy, L., Rouzier, R., & Bonneau, C. (2023). Bisphenol A and breast cancer: State of knowledge and meta-analysis. *Bulletin du Cancer*, 110(2), 151-159.
- García-Gutiérrez, L., Bretones, G., Molina, E., Arechaga, I., Symonds, C., Acosta, J. C., ... & León, J. (2019). Myc stimulates cell cycle progression through the activation of Cdk1 and phosphorylation of p27. *Scientific Reports*, 9(1), 18693.
- GEO2R, (2023). Gene Expression Omnibus, <https://www.ncbi.nlm.nih.gov/geo/geo2r/>, Last accessed on August 10, 2023.
- GEPIA2, (2023). Gene Expression Profiling Interactive Analysis, <http://gepia2.cancer-pku.cn/#index>, Last accessed on August 10, 2023.
- Gyorffy, B. (2021). Survival analysis across the entire transcriptome identifies biomarkers with the highest prognostic power in breast cancer. *Computational and Structural Biotechnology Journal*, 19, 4101-4109.
- Hong, X., Zhou, Y., Zhu, Z., Li, Y., Li, Z., Zhang, Y., ... & Shen, T. (2023). Environmental endocrine disruptor bisphenol A induces metabolic derailment and obesity via upregulating IL-17A in adipocytes. *Environment International*, 172, 107759.
- Huang, D. W., Sherman, B. T., & Lempicki, R. A. (2009). Systematic and integrative analysis of large gene lists using DAVID bioinformatics resources. *Nature Protocols*, 4(1), 44-57.
- Hwang, S., Lim, J. E., Choi, Y., & Jee, S. H. (2018). Bisphenol A exposure and type 2 diabetes mellitus risk: a meta-analysis. *BMC Endocrine Disorders*, 18(1), 81.
- JavanMoghadam, S., Weihua, Z., Hunt, K. K., & Keyomarsi, K. (2016). Estrogen receptor alpha is cell cycle-regulated and regulates the cell cycle in a ligand-dependent fashion. *Cell Cycle*, 15(12), 1579-1590.
- Jensen, L. J., Kuhn, M., Stark, M., Chaffron, S., Creevey, C., Muller, J., ... & von Mering, C. (2009). STRING 8-a global view on proteins and their functional interactions in 630 organisms. *Nucleic Acids Research*, 37(suppl_1), D412-D416.
- KM-plotter, (2023). Official Website of The Kaplan Meier plotter, <https://kmplot.com/analysis/>, Last accessed on August 10, 2023.
- Kustatscher, G., Grabowski, P., & Rappsilber, J. (2017). Pervasive coexpression of spatially proximal genes is buffered at the protein level. *Molecular Systems Biology*, 13(8), 937.
- Kwon, Y. (2022). Potential pro-tumorigenic effect of bisphenol A in breast cancer via altering the tumor microenvironment. *Cancers*, 14(12), 3021.
- Li, T., Fu, J., Zeng, Z., Cohen, D., Li, J., Chen, Q., Li, B., & Liu, X. S. (2020). TIMER2.0 for analysis of tumor-infiltrating immune cells. *Nucleic Acids Research*, 48(W1), W509-W514.
- Li, L., Wang, M. Y., Jiang, H. B., Guo, C. R., Zhu, X. D., Yao, X. Q., Zeng, W. W., Zhao, Y., & Chi, L. K. (2023a). Bisphenol A induces testicular oxidative stress in mice leading to ferroptosis. *Asian Journal of Andrology*, 25(3), 375-381.
- Li, C., Sang, C., Zhang, S., Zhang, S., & Gao, H. (2023b). Effects of bisphenol A and bisphenol analogs on the nervous system. *Chinese*

- Medical Journal*, 136(3), 295-304.
- Nardin, S., Mora, E., Varughese, F. M., D'Avanzo, F., Vachanaram, A. R., Rossi, V., Saggia, C., Rubinelli, S., & Gennari, A. (2020). Breast cancer survivorship, quality of life, and late toxicities. *Frontiers in Oncology*, 10, 864.
- Niu, Y., Xu, J., & Sun, T. (2019). Cyclin-dependent kinases 4/6 inhibitors in breast cancer: Current status, resistance, and combination strategies. *Journal of Cancer*, 10(22), 5504-5517.
- Ogawa, M., Kitamoto, J., Takeda, T., & Terada, M. (2023). Bisphenol A prevents MCF-7 breast cell apoptosis via the inhibition of progesterone receptor transactivation. *Journal of Biochemical and Molecular Toxicology*, e23367.
- Pei, J., Wang, Y., & Li, Y. (2020). Identification of key genes controlling breast cancer stem cell characteristics via stemness indices analysis. *Journal of Translational Medicine*, 18(1), 74.
- Pekarek, L., Torres-Carranza, D., Fraile-Martinez, O., García-Montero, C., Pekarek, T., Saez, M. A., ... & Ortega, M. A. (2023). An Overview of the Role of MicroRNAs on Carcinogenesis: A Focus on Cell Cycle, Angiogenesis and Metastasis. *International Journal of Molecular Sciences*, 24(8), 7268.
- Priyadarshini, E., Parambil, A. M., Rajamani, P., Ponnusamy, V. K., & Chen, Y. H. (2023). Exposure, toxicological mechanism of endocrine disrupting compounds and future direction of identification using nano-architectonics. *Environmental Research*, 225, 115577.
- Ritchie, S. C., Lambert, S. A., Arnold, M., Teo, S. M., Lim, S., Scepanovic, P., ... & Inouye, M. (2021). Integrative analysis of the plasma proteome and polygenic risk of cardiometabolic diseases. *Nature Metabolism*, 3(11), 1476-1483.
- Shannon, P., Markiel, A., Ozier, O., Baliga, N. S., Wang, J. T., Ramage, D., Amin, N., Schwikowski, B., & Ideker, T. (2003). Cytoscape: a software environment for integrated models of biomolecular interaction networks. *Genome Research*, 13(11), 2498-2504.
- Stillwater, B. J., Bull, A. C., Romagnolo, D. F., Neumayer, L. A., Donovan, M. G., & Selmin, O. I. (2020). Bisphenols and risk of breast cancer: A narrative review of the impact of diet and bioactive food components. *Frontiers in Nutrition*, 7, 581388.
- STRING, (2023). Protein-Protein Interaction Networks Functional Enrichment Analysis, <https://string-db.org/>, Last accessed on August 10, 2023.
- Sung, H., Ferlay, J., Siegel, R. L., Laversanne, M., Soerjomataram, I., Jemal, A., & Bray, F. (2021). Global cancer statistics 2020: GLOBOCAN estimates of incidence and mortality worldwide for 36 cancers in 185 countries. *CA: A Cancer Journal for Clinicians*, 71(5), 209-249.
- Tang, Z., Kang, B., Li, C., Chen, T., & Zhang, Z. (2019). GEPIA2: an enhanced web server for large-scale expression profiling and interactive analysis. *Nucleic Acids Research*, 47(W1), W556-W560.
- TIMER2.0, (2023). Tumor IMMune Estimation Resource, <http://cistrome.org/TIMER/>, Last accessed on August 10, 2023.
- Tillett, T. (2009). Bisphenol A, chapter 2: new data shed light on exposure, potential bioaccumulation. *Environmental Health Perspectives*, 117(5), A210.
- UALCAN, (2023). The University of ALabama at Birmingham Cancer Data Analysis Portal, <https://ualcan.path.uab.edu/>, Last accessed on August 10, 2023.
- WHO, (2023). Official Website of World Health Organization, <https://www.who.int/health-topics/cancer/>, Last accessed on August 12, 2023.
- Xue, M., Zhang, K., Mu, K., Xu, J., Yang, H., Liu, Y., ... & Zhuang, T. (2019). Regulation of estrogen signaling and breast cancer proliferation by an ubiquitin ligase TRIM56. *Oncogenesis*, 8(5), 30.
- Yadav, S. K., Bijalwan, V., Yadav, S., Sarkar, K., Das, S., & Singh, D. P. (2023). Susceptibility of male reproductive system to bisphenol A, an endocrine disruptor: Updates from epidemiological and experimental evidence. *Journal of Biochemical and Molecular Toxicology*, 37(4), e23292.
- Yesilkent, E. N., & Ceylan, H. (2022). Investigation of the multi-targeted protection potential of tannic acid against doxorubicin-induced kidney damage in rats. *Chemico-Biological Interactions*, 365, 110111.
- Zhang, X., Yang, L., Huang, B., Yin, J., & Wei, Y. (2023). Identification and validation of Cyclin A2 and Cyclin E2 as potential biomarkers in small cell lung cancer. *Oncol Res Treat*, 46(6), 246-258.
- Zhou, H., Lei, P. J., & Padera, T. P. (2021). Progression of metastasis through lymphatic system. *Cells*, 10(3), 627.
- Zuryn, A., Krajewski, A., Klimaszewska-Wisniewska, A., Grzanka, A., & Grzanka, D. (2019). Expression of cyclin B1, D1 and K in nonsmall cell lung cancer H1299 cells following treatment with sulforaphane. *Oncology Reports*, 41(2), 1313-1323.

Cite as: Akkus, M., & Ceylan, H. (2023). Identification and verification of promising diagnostic genes in bisphenol A-associated breast cancer development via *in silico* analysis. *Front Life Sci RT*, 4(2), 72-78.

Supplementary

Suppl. Table 1. GO and KEGG pathways enrichment analysis for **upregulated DEGs**.

Category	Term	PValue	Genes
BP	GO:0008284~positive regulation of cell proliferation	1,10E-03	<i>FGFBP1, TNC, LAMC2, SOX9, THBS1, PTHLH, CXCL5</i>
BP	GO:0008544~epidermis development	1,30E-03	<i>KRT14, LAMC2, CST6, PTHLH</i>
BP	GO:0000281~mitotic cytokinesis	2,50E-03	<i>KIF23, CEP55, ZNF365</i>
BP	GO:0030198~extracellular matrix organization	1,40E-02	<i>TNC, LAMC2, SOX9, THBS1</i>
BP	GO:0008608~attachment of spindle microtubules to kinetochore	2,30E-02	<i>KNL1, NDC80</i>
BP	GO:0007267~cell-cell signaling	2,70E-02	<i>FGFBP1, INHBA, PTHLH, CXCL5</i>
BP	GO:0000082~G1/S transition of mitotic cell cycle	2,80E-02	<i>RRM2, MCM10, INHBA</i>
BP	GO:0007062~sister chromatid cohesion	2,90E-02	<i>KNL1, NDC80, ZWINT</i>
BP	GO:0071397~cellular response to cholesterol	3,00E-02	<i>INHBA, LRP8</i>
BP	GO:0006271~DNA strand elongation involved in DNA replication	3,80E-02	<i>GINS1, GINS2</i>
BP	GO:0032270~positive regulation of cellular protein metabolic process	3,80E-02	<i>UHRF1, INHBA</i>
BP	GO:0042493~response to drug	4,30E-02	<i>INHBA, THBS1, LRP8, DUSP6</i>
CC	GO:0005615~extracellular space	4,30E-03	<i>FGFBP1, TCN1, LIPG, TNC, LAMC2, THBS1, CST6, F3, PTHLH, CXCL5</i>
CC	GO:0000811~GINS complex	7,20E-03	<i>GINS1, GINS2</i>
CC	GO:0005576~extracellular region	1,30E-02	<i>FGFBP1, TCN1, LIPG, TNC, LAMC2, INHBA, THBS1, LRP8, PTHLH, CXCL5</i>
CC	GO:0031298~replication fork protection complex	1,70E-02	<i>GINS2, MCM10</i>
CC	GO:0000777~condensed chromosome kinetochore	1,90E-02	<i>KNL1, NDC80, ZWINT</i>
CC	GO:0031012~extracellular matrix	3,40E-02	<i>TNC, THBS1, EDIL3, F3</i>
CC	GO:0009986~cell surface	4,10E-02	<i>FGFBP1, LIPG, THBS1, F3, PROM2</i>
MF	GO:0008201~heparin binding	7,30E-03	<i>FGFBP1, LIPG, LAMC2, THBS1</i>
MF	GO:0043138~3'-5' DNA helicase activity	1,70E-02	<i>GINS1, GINS2</i>
MF	GO:0005200~structural constituent of cytoskeleton	3,10E-02	<i>KRT14, NDC80, KRT6B</i>
KEGG_PATHWAY	hsa04512:ECM-receptor interaction	8,1E-03	<i>TNC, LAMC2, THBS1</i>
KEGG_PATHWAY	hsa04510:Focal adhesion	4,1E-03	<i>TNC, LAMC2, THBS1</i>

Suppl. Table 2. GO and KEGG pathways enrichment analysis for **downregulated DEGs**.

Category	Term	PValue	Genes
BP	GO:0006956~complement activation	1,70E-02	<i>C1S, C1R, CFB</i>
BP	GO:0043030~regulation of macrophage activation	2,00E-02	<i>RORA, SLC7A2</i>
BP	GO:0006809~nitric oxide biosynthetic process	2,90E-02	<i>RORA, SLC7A2</i>
BP	GO:0016601~Rac protein signal transduction	4,20E-02	<i>CDH13, RHOU</i>
BP	GO:0006810~transport	4,40E-02	<i>CLCA2, LAPTM5, ABCG1, SLC7A2</i>
BP	GO:0055114~oxidation-reduction process	4,40E-02	<i>SDR16C5, DHRS9, MAOA, HSD17B2, CYP4B1</i>
BP	GO:0010906~regulation of glucose metabolic process	4,90E-02	<i>PDK4, RORA</i>
CC	GO:0005886~plasma membrane	7,70E-03	<i>KLRC2, PLCL1, FHL1, CXCR4, SLC7A2, GHR, IL1RL1, CLEC2B, GPNMB, BASP1, CLCA2, CDH13, RHOU, IL6R, GPM6B, ABCG1, CFB, GHR, CLEC2B, GPNMB, KLRC2, CLCA2, LAPTM5, GPR137B, ABCG1, SLC7A2</i>
CC	GO:0005887~integral component of plasma membrane	9,10E-03	<i>SDR16C5, RTN1, DHRS9, HSD17B2, CYP4B1, ABCG1</i>
CC	GO:0005789~endoplasmic reticulum membrane	3,60E-02	<i>C1S, C1R, CFB</i>
CC	GO:0072562~blood microparticle	4,20E-02	<i>GHR, IL1RL1, IL6R</i>
MF	GO:0004896~cytokine receptor activity	2,70E-03	<i>CLEC2B, KLRC2, GALNT15, CHI3L1</i>
MF	GO:0030246~carbohydrate binding	8,30E-03	<i>DHRS9, HSD17B2</i>
MF	GO:0047035~testosterone dehydrogenase (NAD+) activity	1,50E-02	<i>SDR16C5, DHRS9</i>
MF	GO:0004745~retinol dehydrogenase activity	3,80E-02	<i>SDR16C5, DHRS9, ADH1B</i>
KEGG_PATHWAY	hsa00830:Retinol metabolism	1,30E-02	<i>C1S, C1R, CFB</i>
KEGG_PATHWAY	hsa04610:Complement and coagulation cascades	1,50E-02	<i>C1S, C1R, CFB</i>



Research article

Structural, thermoelectric, and magnetic properties of pure and Ti-doped $\text{Ca}_3\text{Co}_4\text{O}_9$ ceramic compounds

Cihat Boyraz^{*1} ¹ Marmara University, Faculty of Technology, Department of Mechanical Engineering, 34854, Istanbul, Türkiye

Abstract

The effect of the Ti element on the incommensurately layered thermoelectric oxide material $\text{Ca}_3\text{Co}_4\text{O}_9$ is investigated. This study compares the structural, morphological, thermoelectric, and magnetic properties of $\text{Ca}_3(\text{Co}_{3.7}\text{Ti}_{0.3})\text{O}_9$ composition to the pristine $\text{Ca}_3\text{Co}_4\text{O}_9$. No significant enhancement of the Seebeck coefficient compared to $\text{Ca}_3\text{Co}_4\text{O}_9$ is observed in the Ti-doped sample. The magnetic properties of the pristine and Ti-doped $\text{Ca}_3\text{Co}_4\text{O}_9$ are detailed, and the possible correlations between pristine and Ti-doped $\text{Ca}_3\text{Co}_4\text{O}_9$ are established. In M-H measurements, the effect of Ti in low temperatures revealed a magnetic phase transition due to two sublattices exhibiting wavy behavior. For each sample, magnetic inhomogeneity in the long-range ferromagnetic ordering, which is clear almost before 19 K, is observed through FC and ZFC curves. The findings on the physical properties of both samples are discussed, considering the previously published results.

Keywords: Structural and magnetic properties; thermoelectricity; Ti-doped $\text{Ca}_3\text{Co}_4\text{O}_9$

1. Introduction

More The reduction of natural energy sources and the high demand for these resources make it crucial to develop new and alternative energy sources. For example, converting waste heat directly into electricity is an economical, environmentally friendly, efficient alternative. Moreover, materials with thermoelectric properties, like double-stranded DNA, are used in life sciences and various biotechnological applications (Yueqi et al., 2016; Heussman et al., 2022; Mogheiseh et al., 2023). The molecular resistance has a linear relationship with length due to the thermoelectric effect in both the tunneling and hopping regimes, in which electrons or holes move sequentially along molecules from one end to the other through many steps in biology (Yueqi et al., 2016; Kun et al., 2019; Li et al., 2019; Chen et al., 2021; Seif et al., 2021).

Studying the thermoelectric effect in single molecules can be used for various purposes, including evaluating the alignment of the molecular orbitals, comprehending the energy conversion

mechanism connected to charge transport, and figuring out whether electrons or holes are responsible for charge transport. Thermoelectric (TE) devices which are low-cost, pollution and maintenance-free, allow for the harvest of waste energy. Various sources such as gasoline-fueled internal combustion engines, power generators (the Seebeck effect), and coolers (the Peltier effect) (Ohtaki et al., 1996; Zang et al., 2020; Ruan et al., 2021; Amaveda et al., 2022) are presently available. But to be efficient, TE devices need to exhibit stable high thermal and chemical properties at elevated temperatures in the air. For practical industrial purposes, thermoelectric materials' performance and relative utility can be evaluated by the figure of merit ZT which is required to be >1 . So far, some oxide systems have been investigated, such as $(\text{Zn}, \text{Al}) \text{O}$ (Ohtaki et al., 1996), La_2CuO_4 (Liu et al., 2022), and In_2O_3 (Klich et al., 2021).

Recently studies at ambient temperature for nano-structured Bi_2Te_3 - Bi_2Se_3 superlattices have yielded a promising high TE figure of merit $Z_T > 2$ (Ozkendir et al., 2022). However, the effectiveness of these systems is incomparable, even with

* Corresponding author.

E-mail address: cboyraz@marmara.edu.tr (C. Boyraz).<https://doi.org/10.51753/flsrt.1249167> Author contributions

Received 08 February 2023; Accepted 11 July 2023

Available online 26 August 2023

2718-062X © 2023 This is an open access article published by Dergipark under the [CC BY](https://creativecommons.org/licenses/by/4.0/) license.

alloys and semiconductors. Even if the popularity of the ongoing research on TE devices has tended to quantum dots or nanowires, such systems are both toxic and unstable at high temperatures. Oxide materials such as NaCo_2O_4 (Perac et al., 2022) and $\text{Ca}_3\text{Co}_4\text{O}_9$ (Klie et al., 2012) have been revealed to possess high thermoelectric properties, which are still not well understood and probably related to the correlation between the behavior of the electrons and phonons in anisotropic phase environments and the low dimensionality of the crystal structure. However, due to the distribution of grains' random orientation in the ceramics, polycrystalline $\text{Ca}_3\text{Co}_4\text{O}_9$ shows a relatively low figure of merit (grain boundary scattering leading to enhanced electrical resistivity). Therefore, the homogeneity of composition during the ceramic sintering process controlling grain growth and different dopants' effects are essential to improve this figure of merit.

Among the layered oxides, increasing attention has been given to $\text{Ca}_3\text{Co}_4\text{O}_9$ as one of the most promising thermoelectric materials (Shi et al., 2021). The crystal structure of $\text{Ca}_3\text{Co}_4\text{O}_9$ can be viewed as rocksalt-type Ca_2CoO_3 layers with a CdI_2 -like CoO_2 layer stacked (Amaveda et al., 2022). Many dopants have been utilized by choosing different kinds of ions at various ratios to improve and optimize thermoelectric performance (Li et al., 2022). Other atomic substitutions for the Ca-site in the rock-salt type Ca_2CoO_3 layers of $\text{Ca}_3\text{Co}_4\text{O}_9$ revealed a practical enhancement in the Seebeck coefficient and texture (Shi et al., 2021). This improvement should be the reason for an increase in carrier mobility due to the effect of the different sizes of atoms in the $\text{Ca}_3\text{Co}_4\text{O}_9$ system. Pristine and elemental substituted Ca-Co-O systems are expected to exhibit a high Seebeck coefficient by optimizing texture, the control of carrier density, and mobility.

In this study, Ti substituted $\text{Ca}_3\text{Co}_4\text{O}_9$ sample, synthesized by solid-state reaction method to figure out the structural and magnetic effects of Ti atom in the $\text{Ca}_3\text{Co}_4\text{O}_9$ system, was investigated. The enhancement of TE performance, which is related to the induced Co spin-entropy via the Ti doping effect in $[\text{Ca}_2\text{CoO}_3]$ and $[\text{CoO}_2]$ sublayers, was exhibited by revealing the Seebeck coefficients of both $\text{Ca}_3\text{Co}_4\text{O}_9$ and $\text{Ca}_3(\text{Co}_{3.7}\text{Ti}_{0.3})\text{O}_9$. The magnetic effect of Ti ions on the $\text{Ca}_3\text{Co}_4\text{O}_9$ system was demonstrated, and the results were compared by $\text{Ca}_3\text{Co}_4\text{O}_9$ composition.

2. Materials and methods

In this study, the powders were synthesized using a solid-state reaction technique with sub-micrometer particle size and the same (99.9% Stream Chemicals) purity. All samples were prepared from CaCO_3 , Co_3O_4 , and TiO_2 from reagent-grade powders. These powders in specific proportions were weighed to obtain the nominal composition of $\text{Ca}_3(\text{Co}_{3.7}\text{Ti}_{0.3})\text{O}_9$ and $\text{Ca}_3\text{Co}_4\text{O}_9$ separately. In an agate mortar, the stoichiometric mixtures of oxides were homogenized and mixed by a stirrer in an isopropyl alcohol medium ($\text{C}_3\text{H}_8\text{O}$) for five h at 230 rpm. The compound was calcinated at (950°C) for 12-24 h in the air to activate phase transition and form.

The samples were cooled to room temperature and ground to obtain high-quality homogenized mixtures and recalinated at (950°C) for 24 h in air. The weight difference in all cases was negligible. 1000 Mpa uniaxial pressure was applied to the pellets, and after that, the pellets were sintered at 950°C for 24h in an air furnace. The crystalline phase and the oxides were analyzed by θ - 2θ two-circle XRD setup (Bruker AXS D8

Advance) using a Cu $K\alpha$ source. The size of the grains and the elemental compositions of the obtained samples were determined by SEM and an in-situ attachment of EDX with the model of JOEL 7000 FE and INCA (Oxford Instrument) software. As a function of magnetic field and temperature, the static magnetization measurements were conducted by a vibrating Sample Magnetometer. Quantum Design PPMS was equipped with a thermal transport option for the in-plane Seebeck coefficient measurements.

3. Results

3.1. Structural and morphological analysis

Crystal properties were investigated by XRD. Fig. 1 shows the XRD patterns of pure $\text{Ca}_3\text{Co}_4\text{O}_9$ and Co-site Ti-doped $\text{Ca}_3\text{Co}_4\text{O}_9$ powder samples produced under the same conditions. A wide range of sintering temperatures (800-950 °C) was used to test the convenient sintering temperature of $\text{Ca}_3\text{Co}_4\text{O}_9$. The decomposition phase of $\text{Ca}_3\text{Co}_4\text{O}_9$ is $\text{Ca}_3\text{Co}_2\text{O}_6$, of which peaks were marked with the # symbol in Fig. 1. At 950°C sintering temperature, the decomposition reaction rarely occurs. It is known in the literature that at over 1200°C, the decomposition reaction of $\text{Ca}_3\text{Co}_4\text{O}_9$ more extensively yields $\text{Ca}_3\text{Co}_2\text{O}_6$ and CoO peaks (Woermann et al., 1970). When lowering the calcinating and sintering temperatures below 750°C, the intensity deteriorates due to the insufficient crystallization phase (Tongfang et al., 2010).

The effects of Ti doping into the $\text{Ca}_3\text{Co}_4\text{O}_9$ depict no clear evidence about the positional shifts of the peaks. However, as shown in Fig. 1, some extra ignorable peaks reveal due to Ti doping. Cohen's method was used to determine the lattice parameters of both $\text{Ca}_3\text{Co}_4\text{O}_9$ and its Ti-doped form (Sari et al., 2023). One such promising material, $\text{Ca}_3\text{Co}_4\text{O}_9$, is incommensurately composed of rocksalt-type Ca_2CoO_3 layers sandwiched between two hexagonal CdI_2 -like CoO_2 layers. The lattice parameters shared by both subystems are $a = 4.8339 \text{ \AA}$, $c = 10.8436 \text{ \AA}$, and $b_1/b_2 = 1.618$ with $\beta = 98.14^\circ$. The $\text{Ca}_3(\text{Co}_{3.7}\text{Ti}_{0.3})\text{O}_9$ composition has the same structural system with the lattice parameters of $a = 4.8332 \text{ \AA}$, $c = 10.8438 \text{ \AA}$, and $b_1/b_2 = 1.617$.

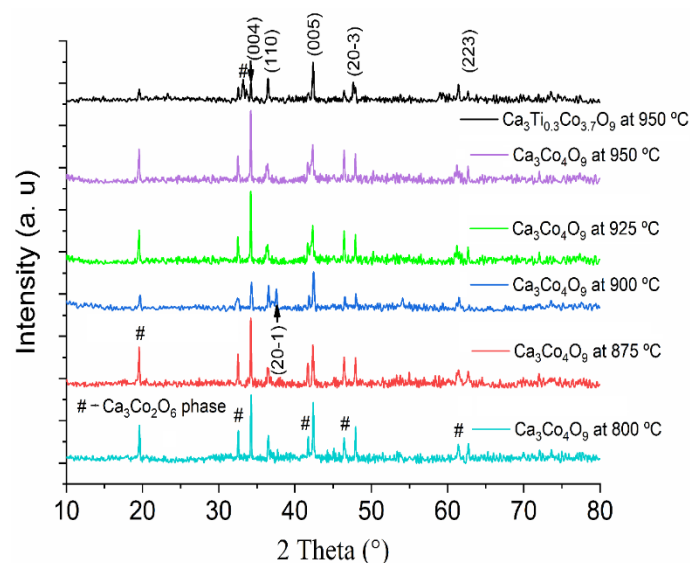


Fig. 1. XRD pattern of $\text{Ca}_3\text{Co}_4\text{O}_9$ at varying annealing temperatures and Ti-doped $\text{Ca}_3\text{Co}_4\text{O}_9$ sample annealed at 950°C are summarized.

The SEM photos of $\text{Ca}_3\text{Co}_4\text{O}_9$ [in (a) and (c)] and $\text{Ca}_3(\text{Co}_{3.7}\text{Ti}_{0.3})\text{O}_9$ [in (b) and (d)] sintered at 950°C for 2 and $5\ \mu\text{m}$ magnifications are shown in Fig. 2. Due to the optimum 950°C (24 h) sintering temperature, porous pellets were minimally formed. This reveals that sintering temperatures below 950°C are insufficient to produce dense $\text{Ca}_3\text{Co}_4\text{O}_9$ and $\text{Ca}_3(\text{Co}_{3.7}\text{Ti}_{0.3})\text{O}_9$ ceramics. A scanning electron microscope study indicated that at high sintering temperature regimes (970 – 1000°C), also many pores were present, and a larger grain size of about $2\ \mu\text{m}$ forms. Over 1000°C sintering temperature, the surface of the grains became even smoother, and grains coarsened (Dos Santos et al., 2020). The observed physical view of the grains should be an indicator of partially melted surface grains (Koshibae et al., 2000; Yang et al., 2009; Dos Santos et al., 2020). The EDX measurement was performed to quantify the elemental composition of the pellet samples. Quantitative texture analysis of the bulk ceramic materials showed only the composition material peaks of $\text{Ca}_3\text{Co}_4\text{O}_9$ and $\text{Ca}_3(\text{Ti}_{0.3}\text{Co}_{3.7})\text{O}_9$. As seen in Table 1 and Table 2, a convenient compositional quantify with the stoichiometry in the EDX analysis was exhibited for $\text{Ca}_3\text{Co}_4\text{O}_9$ and $\text{Ca}_3(\text{Co}_{3.7}\text{Ti}_{0.3})\text{O}_9$ samples.

Table 1

The EDX measurement results of the $\text{Ca}_3\text{Co}_4\text{O}_9$ sample in K shell energies are depicted.

Element	Weight %	Atomic %	Net Int.	Net Int. Error
O K	30.63	54.44	1081.11	0.01
Ca K	23.22	18.57	4376.83	0.01
Co K	46.15	26.99	1690.21	0.01

Table 2

The EDX measurement results of the Ti-doped $\text{Ca}_3\text{Co}_4\text{O}_9$ sample in K shell energy levels are summarized.

Element	Weight %	Atomic %	Net Int.	Net Int. Error
O K	24.78	50.08	566.3	0.01
Ca K	26.47	21.35	1808.31	0.01
Ti K	10.48	5.77	730.04	0.01
Co K	38.27	22.8	630.9	0.01

The Heikes formula (Eq. 1) is useful for determining the Seebeck coefficient in strongly correlated oxide materials (Shi et al., 2021).

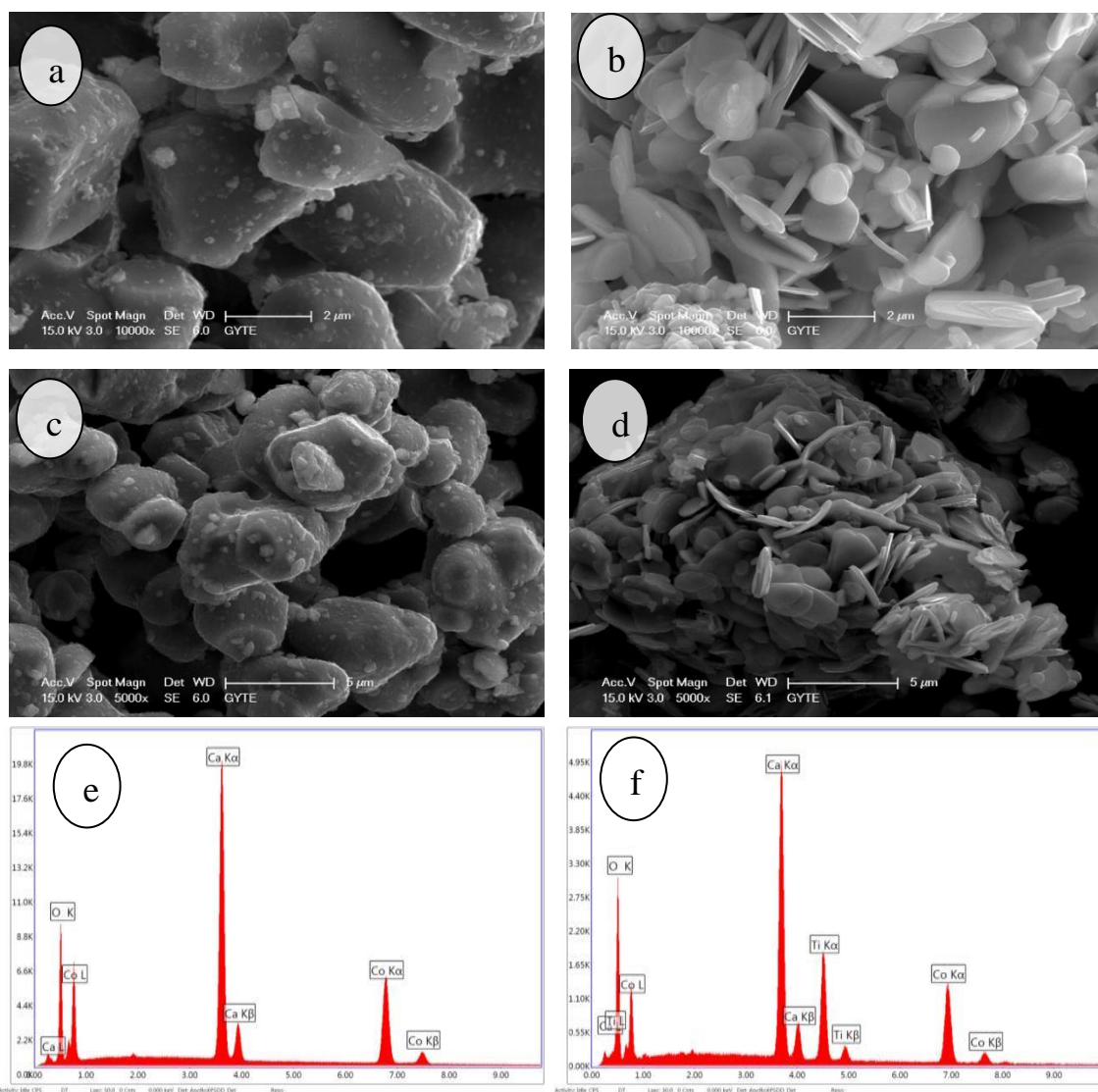


Fig. 2. The SEM images of $\text{Ca}_3\text{Co}_4\text{O}_9$ in (a), (c), and Ti-doped $\text{Ca}_3\text{Co}_4\text{O}_9$ in (b) and (d) both annealed at 950°C are summarized. In (e) and (f), the EDX measurement results are depicted for $\text{Ca}_3\text{Co}_4\text{O}_9$ and Ti-doped $\text{Ca}_3\text{Co}_4\text{O}_9$ samples, respectively.

3.2. Thermoelectric analysis

$$S = -\frac{k_B}{e} \ln\left(\frac{g_3}{g_4} \frac{1-x}{x}\right) \tag{Eq. 1}$$

In Eq. 1, Co^{4+} concentration is shown by x , k_B is the Boltzmann constant, e is the electronic charge, and the orbital degeneracies of Co^{3+} and Co^{4+} in the CoO_2 layer are given by g_3 and g_4 , respectively. In the literature, $x=0.5$ has been found as a critical concentration value of Co^{4+} in the CoO_2 layers, which results in a Co-valence state of + 3.5 (Li et al., 2022). A possibility of this mixed-valence state in the CoO_2 layer is assumed for the large S . At room temperature, the Seebeck coefficients of pristine bulk $\text{Ca}_3\text{Co}_4\text{O}_9$ and Ti-doped $\text{Ca}_3\text{Co}_4\text{O}_9$ were measured to be $S = 130 \mu\text{V}/\text{K}$ and $S = 136 \mu\text{V}/\text{K}$, respectively. Thus, a slight increment in the Seebeck coefficient of Ti-doped $\text{Ca}_3\text{Co}_4\text{O}_9$ was observed within the experimental uncertainty of the transport measurement setup (Hu et al., 2016).

Similar results for the thin-film form of the Ti-doped $\text{Ca}_3\text{Co}_4\text{O}_9$ were found in the literature (Hu et al., 2016). Some nanoparticle systems also exhibit similar thermoelectric behavior, and those are used in life science (Aksu et al., 2022; Boyraz et al., 2022; Chein et al., 2022; Hinterdinget al., 2022; Boyraz et al., 2023).

3.3. Magnetic analysis

Magnetic field-dependent magnetization measurements

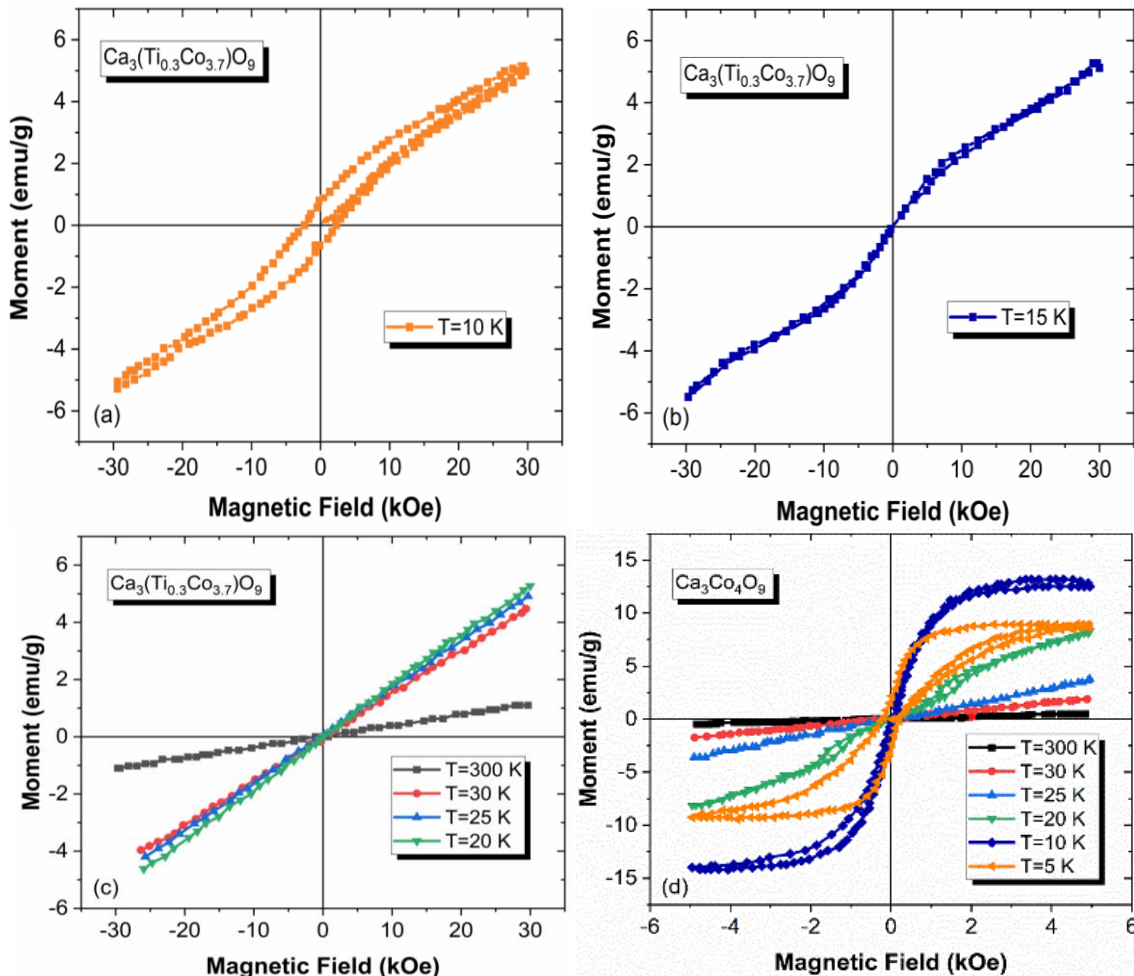


Fig. 3. The magnetic field-dependent magnetization of CTCO in (a), (b), and (c) and CCO in (d) at the given temperatures were exhibited.

conducted for CCO and CTCO samples in a wide temperature range of ($T=5, 10, 20, 25, 30,$ and 300 K) and ($T=10, 15, 20, 25, 30,$ and 300 K) in Fig. 3 respectively. As seen in (a) and (b), the $\text{Ca}_3(\text{Co}_{3.7}\text{Ti}_{0.3})\text{O}_9$ sample exhibits ferromagnetic behavior at 10 and 15 K.

It is known that the crystal structure of $\text{Ca}_3\text{Co}_4\text{O}_9$ can be viewed as rocksalt-type Ca_2CoO_3 layers with CdI_2 -like stacked CoO_2 layer. The wavy behavior in (b) should be the reason for the magnetic phase transition due to two sublattices (Klie et al., 2012). Hence, these two layers provide two sub-lattices with different Curie temperatures (T_c). Similar wavy behavior was observed for CCO at 20 K in Fig. 3 (d). The wavy behavior in low temperatures should not be attributed to the change in the domain structure. Fig. 3 (c) illustrates that $\text{Ca}_3(\text{Co}_{3.7}\text{Ti}_{0.3})\text{O}_9$ and $\text{Ca}_3\text{Co}_4\text{O}_9$ structures show an apparent paramagnetic behavior above 15 K and 20 K, respectively.

Temperature evaluation of magnetization (M) in a field of 50 Oe (FC) and after cooling the sample in ZFC conditions was depicted in Fig. 4 (a) and (b) for the samples $\text{Ca}_3\text{Co}_4\text{O}_9$ and $\text{Ca}_3(\text{Co}_{3.7}\text{Ti}_{0.3})\text{O}_9$ respectively. As seen in Fig. 4 (a) and (b), there is a magnetic phase transition in both $\text{Ca}_3\text{Co}_4\text{O}_9$ (at 20 K) and $\text{Ca}_3(\text{Co}_{3.7}\text{Ti}_{0.3})\text{O}_9$ (at 18.9 K). These magnetic phase transitions have been attributed to the ferr-to-ferromagnetic transitions below Neel temperature. In pristine and Ti-doped CCO, the existence of magnetic inhomogeneity in the long-range ferromagnetic ordering is clear almost before 19 K for each sample due to the separation of each ZFC and FC curve (Hira et al., 2019).

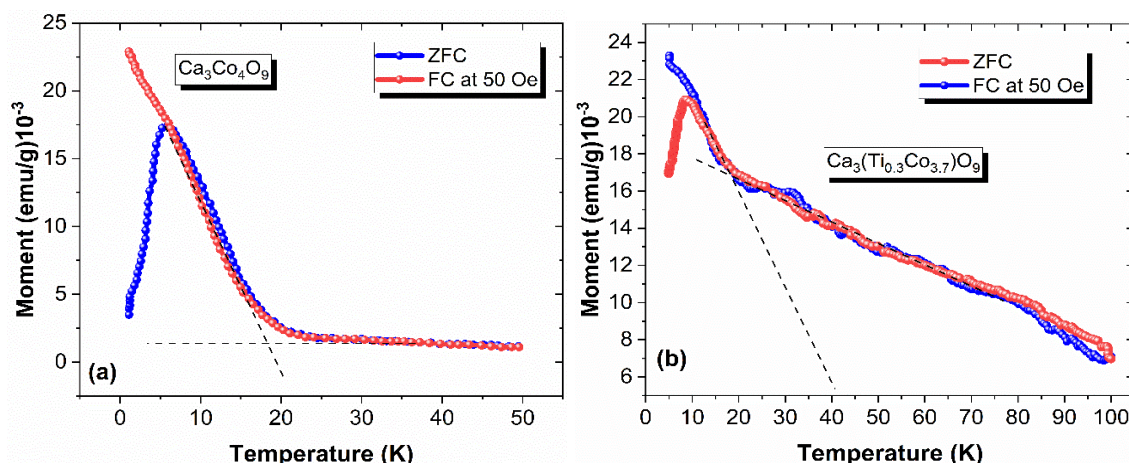


Fig. 4. The temperature-dependent zero-field-cooled (ZFC) and field-cooled (FC) magnetizations for $\text{Ca}_3\text{Co}_4\text{O}_9$ and $\text{Ca}_3(\text{Co}_{3.7}\text{Ti}_{0.3})\text{O}_9$ in (a) and (b) respectively.

4. Conclusion

The pristine and Ti-doped CCO samples were fabricated by the solid-state reaction method. The structural and magnetic characteristics of pure and Ti-doped CCO were compared. The structural effect of Ti in pristine CCO was revealed by calculating lattice parameters indicating a very small variation in the Ti-doped sample. In the literature, the Seebeck coefficient of $\text{Ca}_3\text{Co}_{3.8}\text{Ti}_{0.2}\text{O}_9$ was measured as $S = 135 \mu\text{V}/\text{K}$ which is very close to our measurement result $S = 136 \mu\text{V}/\text{K}$ for $\text{Ca}_3(\text{Co}_{3.7}\text{Ti}_{0.3})\text{O}_9$ (Hu et al., 2016).

In M-H measurements, the effect of Ti in low temperatures revealed itself as a magnetic phase transition due to two sublattices exhibiting wavy behavior.

The separation of each ZFC and FC curve indicates magnetic inhomogeneity in the long-range ferromagnetic ordering, which is clear almost before 19 K for each sample. An increment in the

Seebeck coefficient was observed due to Ti substitution, which also brought inhomogeneity to the pristine CCO. Especially in powder form, the thermoelectric effect provides a new field of study in transport properties in DNA studies. Thus, CCO may be a suitable candidate for molecular studies in life science.

Acknowledgments: This work was supported by the Marmara University BAPKO unit with project number FYL-2022-10334.

Conflict of interest: The author declares that he has no conflict of interests.

Informed consent: The author declares that this manuscript did not involve human or animal participants and informed consent was not collected.

References

- Amaveda, H., Mora, M., Dura, O. J., Torres, M. A., Madre, M. A., Marinel, S., & Sotelo, A. (2022). Influence of ceramic particles additions on the properties of $\text{Ca}_3\text{Co}_4\text{O}_9$. *SN Applied Sciences*, 4(4), 159.
- Boyraz, C., Aksu, P., Guler, A., Arda, L. (2022). The effect of defects formed under pressure on CuCrO_2 delafossite. *SN Applied Sciences*, 4(7), 193.
- Boyraz, C., Aksu, P., Guler, A., Oner, Y., & Fujioka, M. (2023). Short-range magnetic order at low temperatures, exchange bias, and negative magnetization in undoped CuCrO_2 . *Journal of Electronic Materials*, 1-9.
- Boyraz, C., Guler, A., Karatas, O., Aksu, P., Alphan, M. C., & Arda, L. (2022). The investigation of effect of defects on the structural, optical, and magnetic properties of CuAlO_2 . *Acta Physica Polonica A*, 142(4), 464-472.
- Chen, H., & Fraser Stoddart, J. (2021). From molecular to supramolecular electronics. *Nature Reviews Materials*, 6, 804-828.
- Chien, C. W., Chung, L. Y., Subramanian, S., Chia, Y., Chen, T., & Yung, S. F. (2022). Preparation and characterization of CuCrO_2 - CeO_2 nanofibers by electrospinning method. *Journal of Materials Science: Materials in Electronics*, 33, 1091-1100.
- Dos Santos, A. M., Thomazini, D., & Gelfuso, M. V. (2020). Cold sintering and thermoelectric properties of $\text{Ca}_3\text{Co}_4\text{O}_9$ ceramics. *Ceramics International*, 46(9), 14064-14070.
- Heussman, D., Kittell, J., von Hippel, P. H., & Marcus, A. H. (2022). Temperature-dependent local conformations and conformational distributions of cyanine dimer labeled single-stranded-double-stranded DNA junctions by 2D fluorescence spectroscopy. *The Journal of Chemical Physics*, 156(4).
- Hinterding, R., Rieks, D., & Feldhoff, A. (2022). Reaction sintering of $\text{Ca}_3\text{Co}_4\text{O}_9$ with BiCuSeO nanosheets for high-temperature thermoelectric composites. *Journal of Electronic Materials*, 51(2), 532-542.
- Hira, U., Grivel, J. C., Christensen, D. V., Pryds, N., & Sher, F. (2019). Electrical, magnetic and magnetotransport properties of Na and Mo doped $\text{Ca}_3\text{Co}_4\text{O}_9$ materials. *Royal Society of Chemistry Advances*, 9, 31274.
- Hu, X., Phillips, P. J., Mazumdar, D., Carlos, J., Kolesnik, I. S., Gupta, A., Ogut, S., & Klie, R. F. (2016). Atomic and electronic structure of Ti substitution in $\text{Ca}_3\text{Co}_4\text{O}_9$. *Journal of Applied Physics*, 120, 205105.
- Klich, W., & Ohtaki, M. (2021). Thermoelectric properties of Mo-doped bulk In_2O_3 and prediction of its maximum ZT. *Ceramics International*, 47(13), 18116-18121.
- Klie, R. F., Qiao, Q., Paulauskas, T., Gulec, A., Rebola, A., Ogut, S., Prange, M. P., Boyraz, C., Ozdemir, M., Mazumdar, D., & Gupta, A. (2012). Observations of Co^{4+} in a higher spin state and the increase in the seebeck coefficient of thermoelectric $\text{Ca}_3\text{Co}_4\text{O}_9$. *Physical Review Letters*, 108(19), 196601.
- Koshibae, W., Tsutsui, K., & Maekawa, S. (2000). Thermopower in cobalt oxides. *Physical Review B*, 62, 6869.
- Kun, W., Edgar, M., & Pramod, R. (2019). Thermal and thermoelectric properties of molecular junctions. *Advanced Functional Materials*, 30, 1904534.
- Li, Y. N., Wu, P., & Wang, L. (2022). Enhanced thermoelectric properties of $\text{Ca}_3\text{Co}_4\text{O}_9$ by adding nano MoS_2 . *Ceramics International*, 48(22), 33967-33975.
- Li, Y., Buerkle, M., & Li, G. (2019). Gate controlling of quantum interfe-


- rence and direct observation of anti-resonances in single molecule charge transport. *Nature Materials*, 18, 357-363.
- Liu, S., Qin, B. C., Wang, D. Y., & Zhao, L. D. (2022). Investigations on the thermoelectric transport properties in the hole-doped La_2CuO_4 . *Zeitschrift für Anorganische und Allgemeine Chemie*, 648(15).
- Mogheiseh, M., Etemadi, E., & Hasanzadeh Ghasemi, R. (2023). Design, molecular dynamics simulation, and investigation of the mechanical behavior of DNA origami nanotubes with auxetic and honeycomb structures. *Journal of Biomolecular Structure and Dynamics*, 1-10.
- Ohtaki, M., Ogura, D., Eguchi, K., & Arai, H. (1996). High temperature thermoelectric properties ($\text{Zn}_{1-x}\text{Al}_x$)O. *Journal of Applied Physics*, 79, 1816-1818.
- Ozkendir, O. M., Miyazaki, H., & Gunaydin, S. (2022). Traces of thermoelectric properties on XAFS spectra. *Journal of Electronic Materials*, 51(4), 1740-1751.
- Perac, S., Savic, S. M., Brankovic, Z., Bernik, S., Radojkovic, A., Kojic, S., Vasiljevic, D., & Brankovic, G. (2022). Microstructural, thermoelectric and mechanical properties of Cu substituted NaCo_2O_4 . *Materials*, 15(3), 4470.
- Ruan, C. C., Song, H. Z., & Liu, S. H. (2021). Enhancement of $\text{Ca}_3\text{Co}_4\text{O}_9$ +delta thermoelectric properties by dispersing SiC nanoparticles. *Ceramics International*, 47(5), 6548-6553.
- Sari, Y. W., Tsalsabila, A., Saputra, A., Nuzulia, N. A., & Herbani, Y. (2023). Hydroxyapatite nucleation and growth modulated by amino acid-capped gold nanoparticles: An in vitro study. *Ceramics International*, 49(11), 17166-17173.
- Seif, A., & Yonatan, D. (2021). Spinterface origin for the chirality-induced spin-selectivity effect. *Journal of the American Chemical Society*, 143(35), 14235-14241.
- Shi, Z. M., Cao, S. Y., Araujo, J. M., Zhang, P., Lou, Z. H., Qin, M. J., Xu, J., & Gao, F. (2021). Plate-like $\text{Ca}_3\text{Co}_4\text{O}_9$: A novel lead-free piezoelectric material. *Applied Surface Science*, 536, 1-5.
- Tongfang, Y., Dawei, L., Yun, O., Feiyue, M., Shuhong, X., Li, J. F., & Jiangyu, L. J. (2010). Nanocrystalline thermoelectric $\text{Ca}_3\text{Co}_4\text{O}_9$ ceramics by sol-gel based electrospinning and spark plasma sintering. *The Journal of Physical Chemistry C*, 114, 10061-10065.
- Woermann, E., & Muan, A. (1970). Phase equilibria in the system CaO-Cobalt oxide in air. *Journal of Inorganic and Nuclear Chemistry*, 32, 1455-1459.
- Yang, G., Ramasse, Q., & Klie, R. F. (2009). Direct measurement of Co-ion spin-state transitions in $\text{Ca}_3\text{Co}_4\text{O}_9$ using variable-temperature electron energy-loss spectroscopy. *Applied Physics Letters*, 94, 093112.
- Yueqi, L., Limin, X., Julio, L., Palma, Y. A., & Nongjian, T. (2016). Thermoelectric effect and its dependence on molecular length and sequence in single DNA molecules. *Nature Communications*, 7, 11294.
- Zhang, L., Liu, Y. C., & Li, S. (2020). Thermoelectric performance enhancement by manipulation of Sr/Ti doping in two sublayers of $\text{Ca}_3\text{Co}_4\text{O}_9$. *Journal of Advanced Ceramics*, 9(6), 769-781.

Cite as: Boyraz, C. (2023). Structural, thermoelectric, and magnetic properties of pure and Ti-doped $\text{Ca}_3\text{Co}_4\text{O}_9$ ceramic compounds. *Front Life Sci RT*, 4(2), 79-84.



Research article

Identification of phenolic content, antibacterial and antioxidant activities of *Lonicera caucasica* PALLAS subsp. *orientalis* leaves

Mehmet Emin Seker^{*1} 

¹ Giresun University, Espiye Vocational School, Department of Medicinal and Aromatic Plants, 28600, Giresun, Türkiye

Abstract

Phenolic compounds, which are a prevalent type of secondary metabolite, are responsible for the antioxidant and antimicrobial properties found in the extracts. To contribute new knowledge to scientific literature, it is essential to study the phenolic content and bioactivity of plant parts that have not been previously studied or are unknown. *Lonicera caucasica* PALLAS subsp. *orientalis* is an endemic species that grows in a few cities in Türkiye. The study involved extracting *L. caucasica* leaves using methanol. The resulting fraction was then analyzed using Liquid Chromatography-High Resolution Mass Spectrometry (LC-HRMS) to determine the phenolic content of the extract. The quantities of 22 out of the 67 phenolic compounds that were identified were determined. Among these, the top three in terms of quantity are chlorogenic acid, with a concentration of $2.223 \pm 0.065 \text{ mg g}^{-1}$, followed by quinic acid at $2.163 \pm 0.057 \text{ mg g}^{-1}$, and syringic acid at $1.192 \pm 0.036 \text{ mg g}^{-1}$. The antioxidant activities of the extracts were determined using the ABTS•+, DPPH (SC50, mg/mL) and FRAP (μM , TEAC) methods. The values were calculated to be 0.0135 ± 0.0001 , 0.0136 ± 0.0001 , and 2368.88 ± 2.94 , respectively. Furthermore, the extracted substance was subjected to tests against three gram-negative bacteria (*Pseudomonas aeruginosa*, *Klebsiella aerogenes*, and *Escherichia coli*) and three gram-positive bacteria (*Enterococcus faecalis*, *Bacillus megaterium*, and *Streptococcus pyogenes*). The outcomes of the tests were documented. The highest level of antibacterial activity was found to be against *P. aeruginosa*. Based on the findings, it has been determined that the leaves of *L. caucasica* contain a considerable amount of phenolic content, exhibit exceptional antioxidant activity, and display a strong antibacterial effect.

Keywords: Antimicrobial activity; antioxidant activity; phenolic content; total phenolic content

1. Introduction

Polyphenols, one of the largest classes of secondary metabolites, include a variety of molecules in the plant kingdom that have at least one aromatic ring replaced by one or more hydroxyl groups (Ferrazzano et al., 2009). Polyphenols have recently attracted the interest of scientists from a variety of disciplines due to the discovery of their extremely advantageous health benefits. Its health benefits are particularly significant in terms of its protective effects against serious diseases such as cardiovascular diseases, diabetes, neurodegenerative diseases, and cancer. Many of these benefits have been partially attributed

to polyphenols' antioxidant properties (Petti and Scully, 2009).

Lonicera caucasica PALLAS subsp. *orientalis* (Lam.) Oda. et Long (Caprifoliaceae, MARE 13533) is a member of the Caprifoliaceae family (Dogan and Tuzlaci, 2015). Additionally, *Lonicera* is a genus of the Caprifoliaceae family and includes several endemic species that are classified as being at risk (Iskender et al., 2006). *Lonicera* typically grows in elevated locations over 500-2790 meters, and it is a 15-19 cm tall plant with a 25-35 cm diameter (Palabas et al., 2005; Dogan, 2014; Tunckol et al., 2020). During May and July, it undergoes blooming and is commonly found in both coniferous and deciduous forests, as well as shrub habitats.

* Corresponding author.

E-mail address: mehmetemin_seker@hotmail.com (M. E. Seker).

<https://doi.org/10.51753/flsrt.1286886> Author contributions

Received 24 April 2023; Accepted 03 June 2023

Available online 26 August 2023

2718-062X © 2023 This is an open access article published by Dergipark under the [CC BY](https://creativecommons.org/licenses/by/4.0/) license.

The genus comprises approximately 180 species native to North Africa, Asia, Europe, and North America (Iskender et al., 2006; Tomaszewski et al., 2019). Registered provinces in Türkiye: Trabzon, Giresun, Sivas, Rize, Kayseri, Hatay, Kastamonu, Ankara, Bolu, Amasya, and Tunceli (endemic). Its local name is Ivy (Sarmaşık). It has two locally known uses (Dogan, 2014).

a) The decoction prepared from its leaves is used internally as an expectorant.

b) The decoction prepared from its fruits is used externally against acne.

The information in the literature is very limited and entirely related to the definition of the genre. Other studies on *Lonicera* in the literature are associated with *Lonicera japonica*. This species' various parts were extracted, analysed, and their bioactivities investigated. *L. japonica*'s flowers, leaves, and branches (Caprifoliaceae) Thumb are widely used as traditional teas and medicines in numerous Far Eastern nations. These plant parts have been used to treat various diseases in these regions for centuries. However, studies on the antioxidant activities of even *L. japonica* are still insufficient (Byun et al., 2004a,b). There is no study in the literature regarding the chemical analysis and bioactivity of *L. caucasica*. Giresun Şebinkarahisar region is of great importance in terms of some endemic species. The aim of this study is to obtain more information about the phenolic content, antioxidant activity, total phenolic content, and antimicrobial properties of *L. caucasica*, an endemic species collected from Şebinkarahisar. This is the first study on the chemical composition and biological activity of *L. caucasica* leaves, as no previous research has been conducted on this plant's leaves.

2. Materials and methods

2.1. Chemicals and reagents

Both sodium sulfate and sodium chloride were obtained from Merck in Darmstadt, which is located in Germany. Trolox® and 2,4,6-Tripyridyl-s-Triazine (TPTZ) were provided by Sigma Aldrich in Munich, Germany. HPLC syringe filters made of 0.45 µm polyvinylidene difluoride (PVDF) were provided by ISOLAB (Germany). The standards used in the analysis were all purchased from Sigma Aldrich in Steinheim, Germany. Merck (Darmstadt, Germany) supplied the extraction with HPLC grade methanol.

2.2. Sampling area

Samples of *L. caucasica* PALLAS subsp. *orientalis* plant leaves were collected from the Şebinkarahisar neighborhood in Giresun. Dr. Rena Huseyinoglu was responsible for identifying these species. These plants' leaves were dried in an oven at 40°C for 48 hours.

2.3. Extraction of phenolic compounds

The leaves of *L. caucasica* were extracted using Soxhlet extraction. To do this, each sample was ground into a powder and then put into a Soxhlet cartridge at a mass of 5 grams. The powdered leaves were extracted with 150 mL of methanol. After being filtered, the solvent was evaporated in a rotary evaporator at a temperature of 40°C and a pressure of 175 millibars. Following dissolution in methanol, the samples were kept at a

temperature of -20 degrees Celsius for Liquid Chromatography-High Resolution Mass Spectrometry (LC-HRMS) analysis.

2.4. Analysis of phenolic compounds with liquid chromatography-high resolution mass spectrometry

LC-HRMS analyses were performed at Bingöl University (BUMLAM), using a high-resolution MS composite of the DIONEX UltiMate 3000 RS pump, the DIONEX UltiMate 3000 RS autosampler, and the LC system with the DIONEX UltiMate 3000 RS column furnace and Exactive Plus Orbitrap (Thermo Fisher Scientific) with a heated electrospray ionization interface.

The analyses were performed on a Phenomenex® Gemini® 3 µm NX-C18 110 Å (100 mm × 2mm) column. The temperature of the column furnace was maintained at 30°C. For the elution gradient, the mobile A phase was prepared by adding 2% (v/v) glacial acetic acid to ultrapure water obtained through an ultrapure water system (GFL 2004/Human Power 1). For the mobile B phase, LC-MS grade methanol was used that is 99.9% pure from Sigma-Aldrich, Germany. The separation was carried out according to the conditions indicated in Table 1, with the sample injection volume of 20.0 µL and the gradient elution conditions at a flow rate of 0.3 mL/min. The analysis time was set to a total of 20 minutes.

Apigenin standard concentration for phytochemical compounds of the LC-Orbitrap HRMS analysis method 10 - 20 - 40 - 60 - 80 - 100 - 200 - 300 - 400 - 500 µg L⁻¹ was prepared and injected three times each.

Table 1

Gradient conditions following elution.

	Retention Time (min.)	Flow Rate (ml/min.)	Mobile Phase A%	Mobile Phase B%
1	0	0.3	100	0
2	0	0.3	100	0
3	2	0.3	100	0
4	13	0.3	2	98
5	15.9	0.3	2	98
6	16	0.3	100	0
7	19	0.3	100	0

2.5. Methodologies for measuring antioxidant activity

The iron (III) reduction/antioxidant strength (FRAP), ABTS, and DPPH radical scavenging methods, which are widely used in the literature, were used to determine the antioxidant activity in plant extracts. In addition, the total phenolic substance determination in the extracts was determined by the Folin-Ciocalteu method. The analyses were carried out in three replications.

2.5.1. Iron (III) reduction / antioxidant power (FRAP) method

Later-developed absorbance measurement of the TPTZ-Fe(II) complex forms the basis of this study's methodology (Benzie and Strain, 1999). A calibration chart with Trolox concentrations from 31.25 to 1000 µM measured all sample activities as micromolar TEAC (Trolox Equivalent Antioxidant Capacity). The FRAP values for all samples were determined to be 5 mg mL⁻¹. An absorbance reading of 595 nm was obtained following a 20-minute incubation at room temperature with 50 µL of plant extract and 1.5 mL of FRAP reagent (acetate buffer,

TPTZ, and $\text{FeCl}_3 \cdot 6\text{H}_2\text{O}$ solutions) (Karacelik et al., 2021a). Each tube's absorbance was evaluated in comparison to distilled water.

2.5.2. ABTS radical scavenging method

The ABTS $\bullet+$ radical scavenging technique is based on the method modified by Re et al. (1999). In brief, ABTS was dissolved in a mixture of ethanol and water (5:1) to make a 7 mM stock solution of ABTS. To create ABTS radical cation (ABTS $\bullet+$), the stock solution of ABTS was mixed with 2.45 mM potassium persulfate in a 1:3 ethanol/water mixture. The mixture was then left at room temperature and in dark for 16-20 hours. With 0.70 (± 0.02) absorption at 734 nm, a 1:40 dilution of 60-40% ethanol-water was used to dilute a ready-to-use blue-green ABTS $\bullet+$ radical solution. Each sample's and standard's concentration were run three times in parallel. For each concentration of the sample/standard, a blank was also read. At a wavelength of 734 nm, after 20 minutes incubation at room temperature. Plots of concentrations corresponding to the discovered absorbance were made, and SC_{50} values in mg mL^{-1} were computed (Karacelik et al., 2015).

2.5.3. DPPH radical scavenging activity

DPPH was used to test radical scavenging (Cuendet et al., 1997). All samples were pre-tested to determine the working range, and standards (BHT, Trolox) were prepared at various concentrations. Once samples were pipetted into the necessary tubes, a 750 μL solution of 100 μM methanolic DPPH was added and vortexed. The mixture was then incubated for 50 minutes at room temperature. The absorbances were measured at the end of the period at 517 nm, which is where DPPH \bullet had the highest absorbance. The calculations involved averaging the parallels and then subtracting the blind values. SC_{50} values were calculated in mg mL^{-1} by plotting concentrations against the corresponding absorbances. Lower SC_{50} values indicate greater radical scavenging capacity (Turkucar et al., 2021).

2.5.4. Determination of total phenolic content (TPC)

The total phenolic content of *L. caucasica* extracts was quantified using a modified Slinkard and Singleton (1977) method with Folin-Ciocalteu reagent, gallic acid, and catechin as standards. The analytical concentration for each sample was 5 mg mL^{-1} . To a final volume of 50 μL , deionized water (2.5 mL) was added to the sample solution, followed by 250 μL of 0.2 N Folin-Ciocalteu reagent. The mixture was vortexed once more and 750 μL of Na_2CO_3 (7.5%) was added after 3 minutes of incubation and vortexing. In addition to this, each sample as well as the standard concentration had blank samples and reagents analyzed. The absorbance at 765 nm was measured following an incubation period of two hours at room temperature. The total phenolic content is given in gram gallic acid equivalents per mL of sample. This is done by drawing separate calibration graphs for gallic acid and catechin standards in the range of 15.63-1000 g mL^{-1} (Karacelik et al., 2021b).

2.6. Determination of antibacterial activity of the extracts

L. caucasica subsp. *orientalis* was tested for three Gram-negative bacteria: *Pseudomonas aeruginosa* (ATCC27853), *Enterobacter aerogenes* (ATCC 3048), and *Escherichia coli*

(ATCC 25922). Also, *L. caucasica* was tested on three Gram-positive bacteria: *Enterococcus faecalis* (ATCC 29212), *Bacillus megaterium* (ATCC 6633), and *Streptococcus pyogenes* (ATCC 19615). The bacteria were supplied by the Molecular Biology and Genetics Laboratory at Erzurum Technical University. The bacteria were aerobically grown on Mueller Hinton Agar (MHA, Merck 1.05437) at 37°C. Disc diffusion and minimum dilution techniques were used to measure antimicrobial activity and minimum inhibitory concentrations (MIC) utilizing the technique described by Seker et al. (2021). The extract was diluted to a concentration of 39-4.8 mg mL^{-1} with 20% DMSO. Ofloxacin (10 g disc^{-1}), netilmicin (30 g disc^{-1}), and sulbactam (SCF) were positive and were used as positive controls for disc diffusion test and Maxipim (Bristol-Myers Squibb, New York, NY, USA) at concentration of 7.81 to 500 g mL^{-1} were used as positive controls for minimum dilution method. 10 μL of 20% DMSO was the negative control for both tests. MIC values were checked by the minimum dilution test. All of the experiments were conducted for three times.

3. Results and discussion

The leaves of *L. caucasica* were screened for eighty-two phenolic compounds, and the presence of fifty-six of them was determined. All substances sought and identified are listed in Table 2. Table 3 lists the determined concentrations of seventeen of these compounds.

Table 2

Phenolic compounds, retention times and mass load ratios used in the determination of phenolic compounds.

Phenolic Compounds	RT (min.)	Quan Peak
Benzoic acid	6.86	121.02950 mz
4-Hydroxybenzoic acid	6.21	137.02442 mz
Salicylic acid	9.95	137.02442 mz
3-hydroxybenzoic acid (3-HBA)	7.17	137.02442 mz
3-hydroxyphenylacetic acid (3-HPA)	<LOD	107.05053 mz
Syringic acid	7.78	197.04555 mz
Gallic acid	0.78	169.01425 mz
Protocatechuic acid	4.30	153.01933 mz
Protocatechuic acid ethyl ester	9.19	181.05063 mz
Protocatechuic aldehyde	5.66	137.02442 mz
2,4-dihydroxybenzoic acid (beta-Resorcylic acid)	7.33	153.01933 mz
Vanillic acid	7.30	167.03498 mz
Homovanillic acid	7.11	181.05063 mz
Vanillin	7.66	151.04007 mz
Gentisic acid	6.43	153.01933 mz
3,4-Dihydroxyphenylacetic acid (DOPAC, Homoprotocatechuic acid)	7.3	167.03498 mz
trans Cinnamic acid	10.33	147.04515 mz
Coumaric acid (trans-3-Hydroxycinnamic acid)	8.29	163.04007 mz
Caffeic acid	7.24	179.03498 mz
Caffeic acid phenyl ester (CAPE)	12.08	283.09758 mz
Ferulic acid	8.54	193.05063 mz
Sinapic acid	8.69	223.06120 mz
Chlorogenic acid	7.07	353.08781 mz
Quinic acid	1.14	191.05611 mz
3-(4-Hydroxyphenyl) propionic acid	<LOD	165.05572 mz

α -Cyano-4-hydroxycinnamic acid	9.23	188.03532 mz
Catechin (Cianidanol)-p	<LOD	289.07176 mz
Epigallocatechin	<LOD	305.06668 mz
Epigallocatechin gallate	<LOD	457.07763 mz
Chrysin	12.25	253.05063 mz
Apigenin	11.39	269.04555 mz
Acacetin	12.48	283.06120 mz
Rhoifolin (Apigenin 7-O-neoheperidoside)	9.49	577.15692 mz
Vicenin 2	<LOD	593.15119 mz
Apigenin 7-glucuronide	10.42	445.07763 mz
Apigenin 7-glucoside	9.64	431.09837 mz
Genkwanin (4',5-Dihydroxy-7-methoxyflavone, Apigenin 7-O-methyl ether)	12.48	283.06120 mz
Apiin (Apigenin-7-(2-O-apiosylglucoside)	9.38	563.14075 mz
Vitexin (Apigenin 8-C-glucoside)	<LOD	431.09837 mz
Schaftoside	8.40	563.14063 mz
Rutin trihydrate M-3H ₂ O	9.24	609.14611 mz
Rutin hydrate M-OH ₂	9.24	609.14611 mz
Luteolin	10.85	285.04046 mz
Luteolin-7-O-glucuronide	9.80	461.07255 mz
Diosmetin (Luteolin 4'-methyl ether)	11.4	299.05611 mz
Orientin	<LOD	447.09328 mz
Isoorientin	<LOD	447.09328 mz
Luteoloside (Luteolin 7-glucoside)	9.03	449.10784 mz
Luteolin 7-rutinoside	9.03	595.16364 mz
Galangin	12.41	269.04555 mz
Quercetin	10.54	301.03538 mz
Isoquercitrin (Quercetin 3-glucoside)	9.30	463.08820 mz
Narcissin (Narcissoside, Isorhamnetin 3-rutinoside)	9.85	623.16176mz
Quercetin 3-rutinoside 7-glucoside	<LOD	771.20374 mz
Isorhamnetin (Quercetin 3'-methyl ether)	11.33	315.05103 mz
Hyperoside (Quercetin 3-D-galactoside)	9.30	463.08820 mz
Kaempferol	10.32	287.05350 mz
Afzelin (Kaempferol 3-rhamnoside)	10.40	431.09837 mz
Kaempferide	<LOD	299.05611 mz
Kaempferitrin	9.50	579.17083 mz
Nicotiflorin (Kaempferol 3-rutinoside, Kaempferol 3-O- β -rutinoside)	9.78	593.15106mz
Astragaln (Kaempferol 3-glucoside)	9.81	447.09328 mz
Tiliroside	10.67	595.14264 mz
Leucoside (Kaempferol 3-sambubioside)	9.84	289.06924 mz
Myricetin	<LOD	319.04291 mz
Fisetin hydrate	9.80	285.04046 mz
Naringin	<LOD	609.18390mz
Naringenin	10.13	271.06120 mz
Sakuranetin (Naringenin 7-O-methyl ether)	11.91	285.07685 mz
Narirutin (Narirutinsa, Naringenin rutinoside)	<LOD	579.17193 mz
Taxifolin	<LOD	305.06558 mz
Taxifolin M+3H	<LOD	308.09012 mz
Hesperidin	<LOD	609.18249 mz
Neohesperidin	<LOD	609.18249 mz

Eriodictyol (3,4,5,7-Tetrahydroxyflavanone)	<LOD	287.05501 mz
Eriocitrin	8.33	595.16684 mz
Liquiritigenin	9.88	255.06628 mz
Liquiritin (4',7-Dihydroxyflavanone 4'-glucoside)	<LOD	417.11911 mz
Genistein	10.95	269.04555 mz
Daidzin	8.24	255.06433 mz
Formononetin (Neochanin)	11.47	267.06628 mz
Kuromanine (Cyanidin 3-glucoside chloride)	9.16	447.09328 mz
Ellagic acid	9.49	300.99899 mz
Esculin hydrate	6.24	339.07216 mz
Phloridzin	9.40	435.12967 mz
Rosmarinic acid	<LOD	359.07724 mz
Glabridin	<LOD	323.12888 mz
Arbutin	<LOD	271.08233 mz
Emodin	13.48	269.04555 mz
Etoposide	<LOD	383.11053 mz
Procyanidin B2	<LOD	577.13515 mz
Doxorubicin Hydrchloride	<LOD	544.18134 mz
Ethylgallate	7.78	197.04555 mz

RT: Retention Time, mz: mass divided by charge number, LOD: Limit of Dedection

Table 3

The amount of some phenolic compounds in the leaves of *L. caucasica* and the detection limits of the instrument.

Phenolic Compound	Detected amount of dry extract (mg g ⁻¹)	LOD ($\mu\text{g kg}^{-1}$)	LOQ ($\mu\text{g kg}^{-1}$)
Gallic Acid	0.011 \pm 0.0003	0.04	0.13
Benzoic acid	0.468 \pm 0.014	0.7	2.7
Syringic Acid	1.192 \pm 0.036	0.6	1.8
Protocatechuic Acid	0.072 \pm 0.0020	0.3	0.9
Protocatechuic Aldehyde	0.029 \pm 0.0012	1.5	5.1
Sesamol	0.009 \pm 0.0003	0.5	1.6
Vannilin	0.003 \pm 0.0001	1.0	3.3
p_coumaric acid	0.013 \pm 0.0003	0.3	0.9
Caffeic Acid	0.044 \pm 0.0013	0.2	0.6
Luteolin	0.088 \pm 0.0024	1.3	4.4
Chlorogenic acid	2.223 \pm 0.065	1.2	3.9
Quinic acid	2.163 \pm 0.057	0.3	0.9
Rutin	0.041 \pm 0.001	0.5	1.7
Luteoloside	0.440 \pm 0.011	4.4	14.7
Luteolin 7-rutinoside	0.315 \pm 0.010	0.5	1.6
Kaempferitrin	0.160 \pm 0.005	0.7	2.2
Apigenin	0.019 \pm 0.0004	0.9	2.9
Rhoifolin	0.026 \pm 0.0005	3.8	12.7
Apigenin 7-glucoside	0.074 \pm 0.0013	0.5	1.5
Tiliroside	0.037 \pm 0.0008	0.5	1.6
Hyperoside (Quercetin 3-D-galactoside)	0.060 \pm 0.0012	0.2	0.8
Kuromanine (Cyanidin 3-glucoside chloride)	0.874 \pm 0.019	0.5	1.6

LOQ: Limit of Quantitation

When the results are examined, benzoic acid (0,468 \pm 0,014), syringic acid (1.192 \pm 0,036), chlorogenic acid (2,223 \pm 0,065), quinic acid (2,163 \pm 0,057), luteoloside (0,440 \pm 0,011),

luteolin 7-rutinoside ($0,315 \pm 0,010$) and kuromanine ($0,874 \pm 0,019$) amounts are higher than the other phenolic compounds found in the leaves. Since the results are presented in milligrams per gram, they are usually considered high. The extract contains significant amounts of chlorogenic acid and quinic acid.

Studies in the literature are generally related to different species such as *L. japonica* Thunb., *Lonicera maackii* and *Lonicera nummularifolia*. In the study conducted with *L. nummularifolia* in Iran, the total phenolic, antioxidant and antibacterial activities of this species were examined, but detailed chemical analyses were not performed. (Farboodnia Jahromi et al., 2020). In a study performed in Ohio, United States, the chemical content of *L. maackii* leaves was investigated, and the presence of quinic acid, coumaric acid hexoside, chlorogenic acid, eriodictyol hexoside, luteolin diglycoside, luteolin-7-glucoside, apigenin-7-glucoside, luteolin, and apigenin was detected. Among them, the amount of chlorogenic acid was determined as 0.737 mg g^{-1} , Apigenin as 0.109 mg g^{-1} , Apigenin-7-Glucoside as 0.652 mg g^{-1} , Luteolin as 1.044 mg g^{-1} and Luteolin-7-Glucoside as 7.036 mg g^{-1} . In this study, it was found that Luteoloside (also known as Luteolin 7-glucoside) has a value of 0.440 ± 0.01 , and Luteolin has a value of $0.088 \pm 0.0024 \text{ mg g}^{-1}$. These values are lower compared to those obtained from *L. maackii*. The amount of Luteolin discovered is considerably lower when compared to *L. maackii*. Interestingly, the leaves of *L. caucasica* contain a significantly higher amount of chlorogenic acid ($2,223 \pm 0.065 \text{ mg g}^{-1}$) compared to the leaves of *L. maackii*. Research conducted in the United States detected the presence of quinic acid, but the concentration was not determined (Cipollini et al., 2008). However, further research indicates that the value is $2,163 \pm 0.057 \text{ mg g}^{-1}$.

In a research project that was carried out in Korea using the leaves of *L. japonica*, the presence of 25 different types of phenolic compounds was discovered (Seo et al., 2012). The derivatives of caffeoylquinic acid appear to be more prevalent than the other phenolics. No common phenolic compounds were analyzed for comparison between the two studies. Recently, research has been conducted on the potential benefits of using *L. japonica* Thunb, a plant from the Caprifoliaceae family, as a supplement to enhance the antioxidant power of cookies. This is

due to the plant's high polyphenolic content, as reported by Cao et al. (2022). Phenolic content was investigated in the berries of some *L. caerulea* cultivars collected from Canada (Yemis et al., 2022). Based on the findings, the concentration of chlorogenic acid ranged from 2.77-3.07 mg per gram, while routine was detected between 1.51-1.96 mg per gram. Quinic acid was also present at a concentration of 9.7-13 mg per gram. From these results, the levels of routine and quinic acid are higher than our previous findings, but the amount of chlorogenic acid is almost identical to what was discovered before. However, it should be noted that this study was conducted on a different species and fruit of *Lonicera*. A recent study by Orsavová et al. (2022) examined the presence of phenolic compounds in the culture fruits of *L. caerulea* L. var. *kamtschatica* collected from various regions. Based on the findings, the levels of gallic acid fall within the range of $0.011\text{-}0.038 \text{ mg g}^{-1}$, rutin falls within $0.02\text{-}0.150 \text{ mg g}^{-1}$, syringic acid falls within $0.001\text{-}0.009 \text{ mg g}^{-1}$, protocatechuic acid falls within $0.022\text{-}0.196 \text{ mg g}^{-1}$, caffeic acid falls within $0.022\text{-}0.226 \text{ mg g}^{-1}$, and chlorogenic acid falls within $2.12\text{-}4.77 \text{ mg g}^{-1}$. Since there is no study to compare the content of *L. caucasica* leaves, a comparison can be made with the leaf of a different species with high phenolic content collected from the Şebinkarahisar region. Comparing the phenolic compounds found in the leaves of *L. caucasica* with those found in the leaves of *Geranium ibericum* subsp. *jubatum*, another endemic species collected around Şebinkarahisar, it is notable that *Geranium* has higher levels of gallic, protocatechuic, and ellagic acid (Seker et al., 2021). On the contrary, *Lonicera* leaves have higher amounts of chlorogenic acid, coumaric acid, and rutin.

Aside from analyzing the chemicals found in *L. caucasica* leaf extracts, its TPC and AA content was also evaluated. The results are presented in Table 4. The results show that *L. caucasica* leaf extracts have strong antioxidant activity. Based on the results, the ABTS^{•+} analysis of the leaf extract displayed lower antioxidant effects when compared to Trolox and BHT. However, DPPH[•] results showed different results. Particularly, DPPH[•] tests demonstrated that leaf extracts possess greater antioxidant activity than BHT. ABTS^{•+} analysis results also indicate that leaf extracts have good antioxidant activity, albeit less than the antioxidant standards BHT and Trolox. These outcomes were roughly 4.3 times stronger than the antioxidant

Table 4

The antioxidant activity and total phenolic content of a phenolic mixture isolated from *L. caucasica* leaves.

Sample	ABTS ^{•+} (SC ₅₀ , mg/mL)	DPPH [•] (SC ₅₀ , mg/mL)	FRAP (µM, TEAC)	Total phenolic content (TPC) (GAE, µg/mL)
<i>L. caucasica</i> leaves	0.0135±0.0001	0.0136±0.0001	2368.88±2.94	808.34±4.40
BHT	0.0005±0.0001	0.0146±0.0004	ND	ND
Trolox	0.0032± 0.0002	0.0029±0.0001	ND	ND

N.D.: not detected.

Triple measurements are represented as means ±SD (standard deviation).

Table 5

The inhibition effects of methanol extract of *L. caucasica* subsp. *orientalis* on various bacteria.

Bacterium	39.0 mg mL ⁻¹	19.5 mg mL ⁻¹	9.75 mg mL ⁻¹	4.8 mg mL ⁻¹	NET 30 µg disc ⁻¹	MIC **Con/**DD	DMSO (%10)
<i>P. aeruginosa</i>	19.33±0.33 ^a	10±1.52 ^b	8.33±0.33 ^b	-	17.3±0.5 ^b	9.75	-
<i>E. aerogenes</i>	8.33±0.33 ^a	7.33±0.33 ^a	9.66±0.33 ^b	8.33±0.33 ^a	20.6±0.5 ^b	4.8	-
<i>E. coli</i>	8.66±0.33 ^a	18.66±0.33 ^d	17±0.57 ^c	11.66±0.33 ^b	18.2± ^b 1	4.8	-
<i>E. faecalis</i>	13±0.57 ^b	16±0.57 ^c	13±0.57 ^b	11±0.57 ^a	19.3±0.5 ^b	4.8	-
<i>B. megaterium</i>	6.33±0.33 ^a	8.66±0.33 ^b	6.66±0.33 ^a	-	15.4±0.5 ^b	9.75	-
<i>S. pyogenes</i>	-	8.66±0.33 ^a	8.66±0.33 ^b	-	18±0.5 ^b	9.75	-

Duncan's multiple range test shows that, at the *p* 0.05 significance level, the means of each line that ends with the same letter are not significantly different from each other.

DD, Diameter of the inhibition zone (mm/sensitive strains), **Con: Concentration

activity of *L. japonica* leaves (Dung et al., 2011).

According to the results, the methanol extract of *L. caucasica* has shown antibacterial effects against both Gram-positive and Gram-negative bacteria. The most antibacterial activity was observed against *P. aeruginosa* and the least antibacterial activity was observed against *B. megaterium* and *S. pyogenes*. Although there was a decrease in the zones due to the decreasing dose for *P. aeruginosa*, this effect was not observed in the other bacteria that were tested. In contrast, dose-independent zones were observed for all other bacteria. It was determined that the extracts caused significant statistical differences compared to the positive control of the netilmicin antibiotic. Netilmicin was chosen because of its inhibitory activity against both Gram-positive and Gram-negative bacteria. Only significant differences were detected between all doses against *E. coli*. According to the obtained results, it can be concluded that the Gram-negative bacteria were more sensitive than the Gram-negative bacteria against the methanol extract of *L. caucasica* subsp. *orientalis*. The results are given in Table 5. There are just a few studies about the various parts of honeysuckle. According to the literature, the plant is traditionally used for colds, stomach problems (Sakinoglu-Oruc and Oruc, 2017), kidney pains (Mehrnia et al., 2021), and as a disinfectant or wound-washing solution (Asaadi, 2021). Examining the literature, it was discovered that the number of studies on this species was limited, and the majority of the existing studies were the plant's taxonomic, systematic, and ethnobotanical studies. This is the first antibacterial record of *L. caucasica* subsp. *orientalis*. Compared to the ethanol extract of *L. nummularifolia* leaves, the antibacterial effects of the methanol extract of *L. caucasica* leaves appear to be nearly identical (Farboodniay Jahromi et al., 2020). The antibacterial

activity of the plant could be associated with its chemical compounds with have various biological activities.

4. Conclusion

In this investigation, chemical analyses of *L. caucasica* leaves were performed for the first time. Phenolic content, total phenolic content amounts, antioxidant and antibacterial effects were measured. Consequently, 67 phenolic compounds were identified in the leaf extracts obtained via methanolic extraction, and the amounts of 22 of these compounds were determined. It has been determined that the extract has strong antibacterial and antioxidant properties. Considering that this plant is used to treat a number of human diseases, it is possible that these treatments result from the leaves' phenolic compounds, antioxidant properties, and bacteria-killing ability. Further exploration of this plant, which can be found in multiple cities across Türkiye, can enhance the general comprehension of the plant and provide scientists with insights into the regional diversity of its chemical composition.

Acknowledgment: This study was supported in 2022 by Giresun University's Commission for Scientific Research Projects, in accordance with the project number FEN-BAP-A-240222-44.

Conflict of interest: The author declares that he has no conflict of interests.

Informed consent: The author declares that this manuscript did not involve human or animal participants and informed consent was not collected.

References

- Asaadi, A. M. (2021). Study of medicinal herbs used by Kurmanjis Kurdish of Bojnourd in North Khorasan province of Iran. *Journal of Ethno-Pharmaceutical Products*, 2(2), 21-34.
- Benzie, I. F., & Strain, J. J. (1999). [2] Ferric reducing/antioxidant power assay: direct measure of total antioxidant activity of biological fluids and modified version for simultaneous measurement of total antioxidant power and ascorbic acid concentration. In: Packer L. (ed) *Methods in Enzymology* (Vol. 299, pp. 15-27). Academic Press.
- Byun, M. W., Jo, C., Jeon, T. W., & Hong, C. H. (2004a). Effects of gamma irradiation on color characteristics and biological activities of extracts of *Lonicera japonica* (Japanese honeysuckle) with methanol and acetone. *LWT-Food Science and Technology*, 37(1), 29-33.
- Byun, M. W., Jo, C., Lee, J. W., Jo, S. K., & Kim, K. S. (2004b). Application of radiation technology to develop green tea leaf as a natural resource for the cosmetic industry. *Radiation Physics and Chemistry*, 71(1-2), 487-489.
- Cao, W., Chen, J., Li, L., Ren, G., Duan, X., Zhou, Q., ... & Liu, X. (2022). Cookies fortified with *Lonicera japonica* Thunb. extracts: Impact on phenolic acid content, antioxidant activity and physical properties. *Molecules*, 27(15), 5033.
- Cipollini, D., Stevenson, R., Enright, S., Eyles, A., & Bonello, P. (2008). Phenolic metabolites in leaves of the invasive shrub, *Lonicera maackii*, and their potential phytotoxic and anti-herbivore effects. *Journal of Chemical Ecology*, 34, 144-152.
- Cuendet, M., Hostettmann, K., Potterat, O., & Dyatmiko, W. (1997). Iridoid glucosides with free radical scavenging properties from *Fagraea blumei*. *Helvetica Chimica Acta*, 80(4), 1144-1152.
- Dogan, A. (2014). Pertek (Tunceli) yöresinde etnobotanik arařtırmalar, Doctoral dissertation, (pp. 1-459). Marmara Üniversitesi, Türkiye.
- Dogan, A., & Tuzlaci, E. (2015). Tunceli'nin bazı yöresel bitki adları. *Avrasya Terim Dergisi*, 3(2), 23-33.
- Dung, N. T., Bajpai, V. K., Rahman, A., Yoon, J. I., & Kang, S. C. (2011). Phenolic contents, antioxidant and tyrosinase inhibitory activities of *Lonicera japonica* Thumb. *Journal of Food Biochemistry*, 35(1), 148-160.
- Farboodniay Jahromi, M. A., Emami, A., Nazeri, R., & Pirbonyeh, N. (2020). Antibacterial and antioxidant activity of extract and fractions of *Lonicera nummularifolia* Jaub & Spach. *Trends in Pharmaceutical Sciences*, 6(2), 131-142.
- Ferrazzano, G. F., Amato, I., Ingenito, A., De Natale, A., & Pollio, A. (2009). Anti-cariogenic effects of polyphenols from plant stimulant beverages (cocoa, coffee, tea). *Fitoterapia*, 80(5), 255-262.
- Iskender, E., Zeynalov, Y., Ozaslan, M., Incik, F., & Yayla, F. (2006). Investigation and introduction of some rare and threatened plants from Turkey. *Biotechnology & Biotechnological Equipment*, 20(3), 60-68.
- Karacelik, A. A., Kucuk, M., Iskefiyeli, Z., Aydemir, S., De Smet, S., Miserez, B., & Sandra, P. (2015). Antioxidant components of *Viburnum opulus* L. determined by on-line HPLC-UV-ABTS radical scavenging and LC-UV-ESI-MS methods. *Food Chemistry*, 175, 106-114.
- Karacelik, A. A., & Sahin, H. (2021a). Determination of chemical compositions, antioxidant and enzyme inhibitory activities of naturally growing *Chenopodium album* subsp. *iranicum* Aellen. *Journal of the Institute of Science and Technology*, 11(3), 2091-2101.
- Karacelik, A. A., Kucuk, M., Efe, D., Cakir, V., & Biyiklioglu, Z. (2021b). Carbonic anhydrase inhibition potential and some bioactivities of the peripherally tetrasubstituted cobalt (II), titanium (IV), manganese (III) phthalocyanines. *Letters in Drug Design & Discovery*, 18(4), 365-371.
- Mehrnia, M., Akaberi, M., Amiri, M. S., Nadaf, M., & Emami, S. A. (2021). Ethnopharmacological studies of medicinal plants in central Zagros, Lorestan Province, Iran. *Journal of Ethnopharmacology*, 280, 114080.
- Palabas, S., Uzun, A., Terzioğlu, S., & Ansin, R. (2005). Trabzon ilinin korunan doğal alanları ve bitkisel tür zenginliği. *Korunan Doğal Alanlar Sempozyumu*, Isparta, Türkiye. 63-65.
- Petti, S., & Scully, C. (2009). Polyphenols, oral health and disease: A review. *Journal of Dentistry*, 37(6), 413-423.
- Orsavová, J., Sytařová, I., Mlček, J., & Miřurcová, L. (2022). Phenolic

- compounds, vitamins C and E and antioxidant activity of edible honeysuckle berries (*Lonicera caerulea* L. var. *kamtschatica* Pojark) in relation to their origin. *Antioxidants*, 11(2), 433.
- Re, R., Pellegrini, N., Prottogente, A., Pannala, A., Yang, M., & Rice-Evans, C. (1999). Antioxidant activity applying an improved ABTS radical cation decolorization assay. *Free Radical Biology and Medicine*, 26(9-10), 1231-1237.
- Sakinoglu-Oruc, F. Ç., & Oruc, S. H. (2017, May). Ethnobotanical aspects of some species in Düzce and its vicinity. *I. International Congress on Medicinal and Aromatic Plants*, Konya, Türkiye. 391-399.
- Seo, O. N., Kim, G. S., Park, S., Lee, J. H., Kim, Y. H., Lee, W. S., ... & Shin, S. C. (2012). Determination of polyphenol components of *Lonicera japonica* Thunb. using liquid chromatography-tandem mass spectrometry: contribution to the overall antioxidant activity. *Food Chemistry*, 134(1), 572-577.
- Slinkard, K., & Singleton, V. L. (1977). Total phenol analysis: automation and comparison with manual methods. *American Journal of Enology and Viticulture*, 28(1), 49-55.
- Seker, M. E., Ay, E., Karacelik, A. A., Huseyinoglu, R., & Efe, D. (2021). First determination of some phenolic compounds and antimicrobial activities of *Geranium ibericum* subsp. *jubatum*: A plant endemic to Turkey. *Turkish Journal of Chemistry*, 45(1), 60-70.
- Tomaszewski, D., Byalt, A., & Gawlak, M. (2019). Leaf and stem epicuticular wax structures in *Lonicera* species (Caprifoliaceae). *Nordic Journal of Botany*, 37(5).
- Tunckol, B., Yasayacak, H., & Aksoy, N. (2020). Distribution patterns of rare *Kitaibela vitifolia* Willd in Turkey: Taxonomy, chorology, and conservation. *Modern Phytomorphology*, 14(1).
- Turkucar, S. A., Karacelik, A. A., & Karakose, M. (2021). Phenolic compounds, essential oil composition, and antioxidant activity of *Angelica pur-purascens* (Avé-Lall.) Gill. *Turkish Journal of Chemistry*, 45(3), 956-966.
- Yemis, G. P., Yemis, O., Drover, J. C., & Delaquis, P. (2022). Antibacterial activity of a polyphenol-rich haskap (*Lonicera caerulea* L.) extract and tannic acid against *Cronobacter* spp. *Food Control*, 140, 109120.

Cite as: Seker, M. E. (2023). Identification of phenolic content, antibacterial and antioxidant activities of *Lonicera caucasica* PALLAS subsp. *orientalis* leaves. *Front Life Sci RT*, 4(2), 85-91.



Research article

Automated comet assay segmentation using combined dot enhancement filters and extended-maxima transform watershed segmentation

Lavdie Rada Ulgen^{*1} ¹ Bahcesehir University, Faculty of Engineering and Natural Sciences, Department of Mathematics, 34353, Istanbul, Türkiye

Abstract

The comet assay, also known as single-cell gel electrophoresis, is a widely used and reliable method for assessing DNA damage and repair in individual cells. It plays a crucial role in the assessment of genetic damage potential and human biomonitoring studies in the medical and biological fields. Ensemble of comet assay individual cells and establishing accurate information on the occurrence of cellular injury followed by the process of cellular restoration is a challenging task. This paper introduces an algorithm for the detection of a distinct head, composed of undamaged DNA, and a tail, comprising damaged or fragmented DNA, in genotoxicity testing images, and provides information on the region properties of such images. The proposed approach combines a dot enhancement filter to distinguish and help in the detection of the head in each cell combined with a multilevel segmentation approach consisting of a watershed-geodesic active contour model that is capable to refine the tail estimation. The effectiveness of the suggested algorithm is quantitatively evaluated with annotation data provided by biologists, and its results are compared with those obtained from previous works. The proposed system exhibits comparable or superior performance to the existing systems while avoiding excessive computational costs.

Keywords: Comet assay; dot enhancement filters; extended-maxima transform; image processing; segmentation; single cell gel; watershed

1. Introduction

DNA, the fundamental blueprint of life, contains all the necessary information for the construction and maintenance of our bodies. However, DNA is constantly subjected to various harmful factors that can lead to its degradation and result in genetic alterations (Chatterjee and Walker, 2017). To effectively study and understand these alterations, reliable techniques are needed to detect and quantify DNA damage at the level of individual cells. A notable method in biological research for evaluating DNA damage is the single-cell gel electrophoresis (SCGE) assay, commonly referred to as the comet assay (Singh et al., 1988; Uthirapathy, 2023). This technique provides a visual, sensitive, fast, and reliable approach to analyzing DNA damage, as introduced by Ostling and Johanson (1984). In this

method, individual cells are embedded in a thin agarose gel on a microscope slide as explained by Fairbairn et al. (1995). The resulting image resembles a comet, with a distinct head composed of intact DNA and a tail consisting of damaged or broken DNA fragments (Fig. 1). The extent of DNA released from the comet's head during electrophoresis correlates with the level of damage inflicted.

Early computational systems developed to segment comet assay cells were predominantly semi-automatic and relied heavily on thresholding-based methods, which made them highly dependent on maximum brightness pixel values (Helmma and Uhl, 2000; Ruz-Suarez et al., 2022). Subsequently, Gyori et al. (2014), introduced OpenComet, an automatic and freely available software system that employs adaptive thresholding to segment comets and identifies their heads based on intensity

* Corresponding author.

E-mail address: lavdie.rada@bau.edu.tr (L. Rada Ulgen).

<https://doi.org/10.51753/flsrt.1319546> Author contributions

Received 24 June 2023; Accepted 27 July 2023

Available online 26 August 2023

2718-062X © 2023 This is an open access article published by Dergipark under the [CC BY](https://creativecommons.org/licenses/by/4.0/) license.

profile analysis. However, this tool struggles to recognize overlapping and heavily damaged comets. In a similar vein, Lee et al. (2018), presented HiComet, a system that employs histogram thresholding for automatic comet cell segmentation, albeit without directly obtaining the segmentation of the comet's head (only head center and radius). Furthermore, this approach encounters difficulties in partitioning overlapping comets. Although these existing comet analysis systems have facilitated detection and segmentation to some extent, they rely on handcrafted image features, making them less effective in noisy backgrounds or when distinguishing individual cells within overlapped regions (Ruz-Suarez et al., 2022).

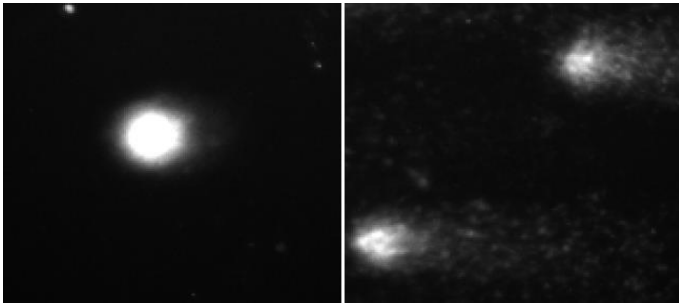


Fig. 1. Different imaging of comet assay cell with low level of DNA damage on the left and high level of DNA damage on the right.

The rapid advancement of machine learning and deep learning techniques has led to a shift in solving the segmentation of the comet assay, prioritizing these methods over fully exploring traditional image processing techniques. One of the first such methods was CometQ, proposed by Ganapathy et al. (2016), utilizes classical machine learning algorithms for the detection and quantification of DNA damage in comet assay images. Nevertheless, its segmentation results require a high amount of trained data, and unfortunately, the program is currently unavailable for download. This method was further followed by other works such as Afiahayati et al. (2022) proposed a CNN model for five-level classification of comet cells, adapting pre-processing image processing techniques and machine learning one. Similarly, Hafiyani et al. (2021), improved upon their previous work by incorporating a hybrid CNN and Extreme Learning Machine (ELM) method for comet classification on buccal mucosa cells, but manual interaction was still required. Lastly, Ruz-Suarez et al. (2022), proposed a system called U-NetComet, which is a fully convolutional neural network-based approach. The purpose of U-NetComet is to automate the segmentation of comets, reducing the need for user intervention and ensuring consistent and reproducible measurements. While the system can be regarded as state-of-the-art, comparable to other machine learning and deep learning algorithms mentioned earlier, its performance is dependent on a few factors. Firstly, it relies on a large and high-quality collection of trained data, which can be resource-intensive to gather. Additionally, tuning the hyperparameters of the system is crucial for optimal results, requiring careful optimization. Lastly, the system demands on machines with large memory capacity, which can limit its application in scenarios with limited resources (Taye, 2023).

In light of the limitations already known for machine learning and deep learning techniques, the author of this study believe that there is an unfilled gap that should be further investigated with the help of image processing techniques. This paper proposes a novel approach for comet segmentation by

utilizing dot enhancement-like structures, and adaptive histogram, which will improve image saturation, in combination with extended-maxima transform watershed segmentation to accurately identify the head and tail of comets, as well as extract essential cell properties for further analysis. The proposed system is a fully automated tool that can effectively segment individual cells in single-cell gel electrophoresis assay images.

The experiments are based on free available data taken from the website <https://www.clir-lab.org/u-netcomet> and some more data provided by Dr. Elda Pacheco-Pantoja from Mexico Medicine School, Health Sciences Division, Universidad Anahuac Mayab.

2. Materials and methods

2.1. Proposed method overall

The proposed method used two separate image processing algorithms to distinguish between comet heads and tails. The reason for such split is due to the fact that the head is a bright circular object whereas the tail is a fuzzy intensity spread in the surrounding of the head that easily can be mixed as a noise. The segmentation module determines whether each pixel belongs to the head or the tail of a comet. To easily follow the way the algorithm has been constructed readers can refer to the diagram of the model shown in Fig. 2.

The proposed identification and extraction of cells head comet assays combine a dot enhancement filter to distinguish and help in the detection of the head in each cell combined with simple threshold technique and refinement, which will avoid the low contrast circle-like structures of the background. Through experiments, it can be seen that the proposed algorithm it is robust compared to the other methods proposed in the literature and can detect hard cases where overlapping comets and heads, which are closed by, are observed and cannot be distinguished easily. The proposed method will mostly define accurately the head contours of such cases.

On the other hand, segmenting the tail of the comets is a real challenge and the existing method such as simple threshold, watershed, and region based would fail. In this work, a watershed segmentation technique based on an extended-maxima transform of the image is proposed, capable to capture corn-like structures, similar to how the tail of comets looks in general. The watershed segmentation based on the above idea might produce structures, which are part of the background. To refine it, segmented object that has a head as the center of the structure are considered.

The most challenging part of such work refers to nearby comets. In cases where nearby comets lack distinct boundaries, a distance function can be utilized to separate the tails. However, it is important to note that this approach may not provide high accuracy. Furthermore, obtaining opinions or expert input from specialists may be challenging due to the limited information available for such specific cases. The proposed system in this research provides a mathematical solution that depends on the circle-like property of the head of the comets.

The proposed algorithm provides two outputs: the original input image with additional contours, indicating the comet region and its head; and a file containing all the mathematical properties, such as head center, head and tail area, head and tail length, extracted from each segmented image.

2.2. Database

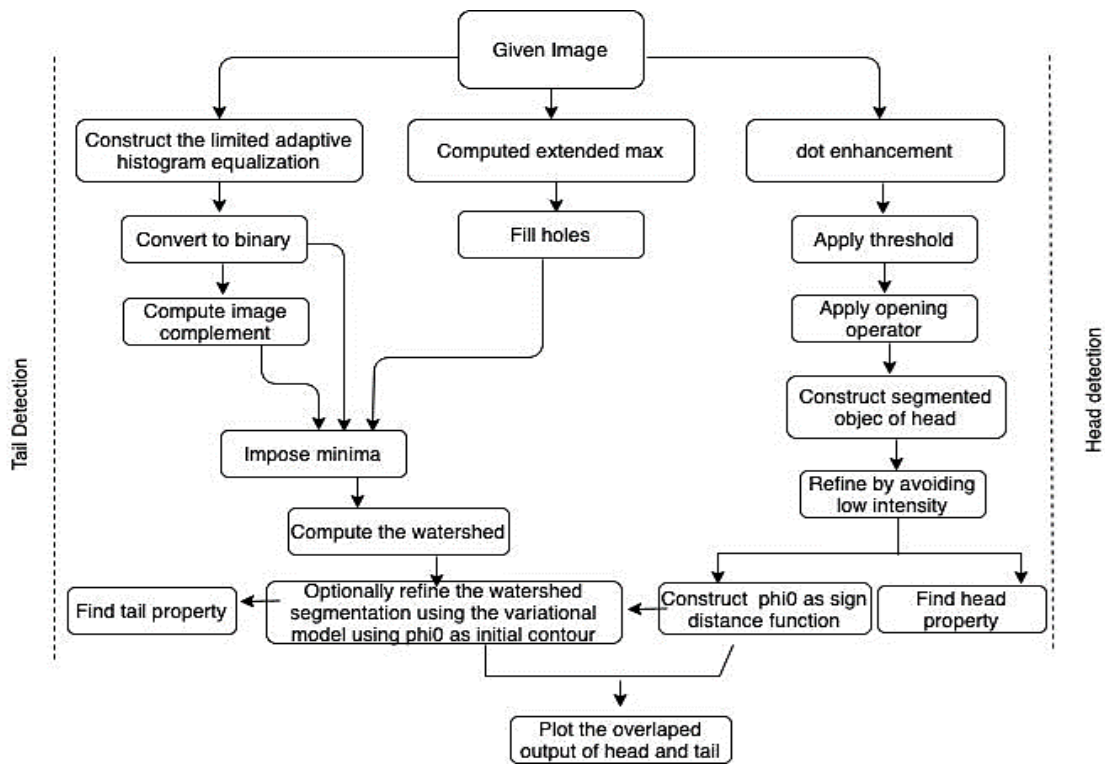


Fig. 2. The diagram of the proposed image processing system.

The initial data set comprises 140 grayscale images of comet assays, with a resolution of 1388×1038 pixels and 288×288 cropped from the original image size 1388×1038 . 1388×1038 pixels are original images taken from experiments whereas the 288×288 images are used for the training and validation of the UNetComets (2022) machine learning system application.

The small-size images have been provided as crop images by the specialist together with a boundary annotation. These images contain cells exhibiting varying degrees of damage, as well as different shapes and sizes due to the magnifying lens used (Fig. 3-9). The images in this research were processed as provided without any resizing or cropping as already used in

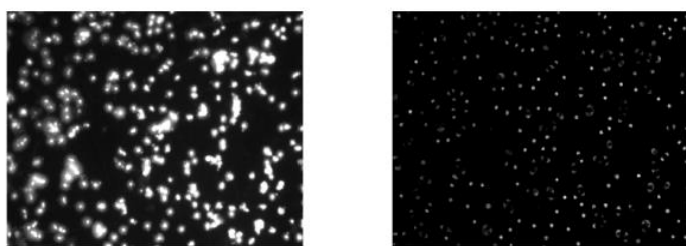


Fig. 3. Original image on left and dot enhanced image on the right.

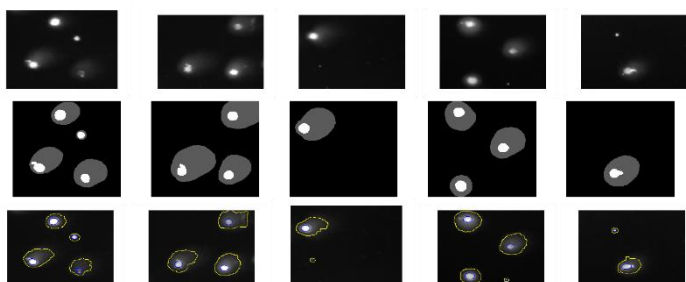


Fig. 4. Test of the proposed algorithm in cases where the comets are separated from each-other. The first row shows the original image, the second row the annotation of the head and the tail by experts and the last row the segmentation with the proposed algorithm.

machine learning techniques. The proposed algorithm can be further improved in the future to archive better accuracy but at this stage, it can be proved that there is no need for costly machine-learning techniques for such problems. Image processing can be a great alternative to solve them.

2.3. Comets head segmentation through dot enhancement filter

Dot enhancement filters are highly effective for circular-like structure detection; as is the segmentation of the assay images head; due to their ability to sensitively respond to dots while maintaining specificity by avoiding the generation of non-dot shapes. In difference with a simple threshold method based on the image intensity, the nearby comets, which are hard to be processed, can be split and as for the knowledge of the author, there is no such work that can properly segment such cases. The approach in this paper combines dot enhancement filters with a watershed-region-based segmentation technique segmentation for the tail of the comets. In this subsection, a concise overview of dot and line enhancement filters in the 2D domain is provided.

Dot and line enhancement filters operate by analyzing the eigenvalues of the 2D Hessian matrix at each location in the image space. Adopting the parameter-free techniques introduced acts as filter enhancement method. These techniques have shown improved sensitivity in nodule detection compared to previous methods. The output, denoted as $z(\lambda_1, \lambda_2)$, from the dot enhancement filters (or line enhancement filters) described in (Li et al., 2003), is obtained as the product of a magnitude function, g_{dot} (or g_{line} for line enhancement), and a likelihood function, k_{dot} (or k_{line} for line enhancement). In the following a brief explanation of these functions has been provided. Consider an image represented as $I(x, y)$, in a 2D domain, its second derivatives can be expressed as I_{xx} , I_{yy} , and I_{xy} . Now, let's assume that a line, denoted as $l(x, y)$, and a dot, denoted as $d(x, y)$, are fuzzy continuous shapes and second-order differentiable functions. The line $l(x, y)$ is oriented along the y-axis, allowing

any line parallel to the x-axis to be represented by a one-dimensional Gaussian function. On the other hand, the dot $d(x,y)$ is characterized by a fuzzy dot shape and can be represented by a 2D Gaussian function. Accordingly, a line and a dot can be described as follows:

$$l(x,y) = \exp\left\{-\frac{x^2}{2\sigma^2}\right\} \quad (1)$$

$$d(x,y) = \exp\left\{-\frac{x^2 + y^2}{2\sigma^2}\right\} \quad (2)$$

where σ the Gaussian parameter it determines the spread or width of the Gaussian function, indicating the size of the dot or the thickness of the line. For the center of a dot, the mixed second derivative I_{xy} is equal to zero. As a result, the dot enhancement filter relies solely on the two eigenvalues of the Hessian matrix namely λ_1 and λ_2 ;

$$\lambda_1 = K + \sqrt{K^2 - Q^2}, \lambda_2 = K - \sqrt{K^2 - Q^2}, \quad (3)$$

where $K = (I_{xx} + I_{yy})/2$, and $Q = I_{xx} I_{yy} - I_{xy} I_{yx}$. To maintain generality and without sacrificing its essence, making the assumption that λ_1 is the largest eigenvalue, satisfying the condition $|\lambda_1| \geq |\lambda_2|$. If this condition is not met, the values of λ_1 and λ_2 has been changed, making λ_1 the larger eigenvalue and λ_2 the smaller eigenvalue.

2.3.1. Construction of the likelihood functions, k_{dot} and k_{line}

The likelihood functions are directly associated with the sensitivity of indicating the probability that a pixel belongs to either a dot or a line. In order to enhance bright objects against a dark background, the sign of the second derivatives should be considered negative. Specifically, for a dot or a nodule-like object, one can anticipate that:

$$\lambda_1 \approx \lambda_2 = -1/\sigma^2 < 0. \quad (4)$$

The output $z(\lambda_1, \lambda_2)$ of the dot enhancement filters, as discussed in Li et al. (2003), is determined by the product of the magnitude function and the likelihood function. The likelihood of a dot can be defined as $e_2 = |\lambda_2|/|\lambda_1|$. Thus, the previously mentioned conditions (4) can be expressed in the following manner:

$$\begin{aligned} \text{dot: } k_{dot}(\lambda_1, \lambda_2) &= e_2 = |\lambda_2|/|\lambda_1|, \\ \text{line: } k_{line}(\lambda_1, \lambda_2) &= 1 - e_2 = (|\lambda_1| - |\lambda_2|)/|\lambda_1|. \end{aligned}$$

Each of the two likelihood functions produces an output value of 1 for a particular shape and an output value of 0 for the other shape.

2.3.2. Construction of the magnitude functions, g_{dot} and g_{line}

For the dot enhancement filter, a suitable choice for the magnitude function is to utilize the value of λ_2 . This is because λ_2 yields a value greater than 0 for a dot and a value of 0 for a line. Therefore, one can define the magnitude function for the dot enhancement filter as $g_{dot} = |\lambda_2|$. Similarly, for the line enhancement filter, the magnitude function can be defined as $g_{line} = |\lambda_1|$. This choice allows us to obtain a value greater than 0 for a line and a value of 0 for a dot. By incorporating the two fundamental criteria of sensitivity and specificity, one can

achieve a high-quality output for the enhanced filter.

$$z_{dot}(\lambda_1, \lambda_2) = \begin{cases} |\lambda_2|^2/|\lambda_1| & \text{for } \lambda_1 < 0, \lambda_2 < 0 \\ 0 & \text{otherwise.} \end{cases} \quad (5)$$

$$z_{line}(\lambda_1, \lambda_2) = \begin{cases} |\lambda_1| - |\lambda_2| & \text{for } \lambda_1 < 0, \lambda_2 < 0 \\ 0 & \text{otherwise.} \end{cases} \quad (6)$$

To fully utilize the filter described in equations (5) and (6), it is beneficial to consider the influence of noise and the scale of objects, which necessitates a multiscale enhancement approach. In order to enhance objects across a range of scales $[d_0, d_1]$, a two-step process can be followed. First, a Gaussian smoothing filter is applied within the scale range of $[d_0/4, d_1/4]$. Subsequently, the dot enhancement filter, as described earlier, is applied, following the methodology outlined in Li et al. (2003) and Lindeberg (1998). This combination of Gaussian smoothing and dot enhancement filters enables the effective enhancement of objects at various scales, taking into account both noise reduction and object scale considerations. The enhancement filters involve two steps that need to be repeated N times, with each repetition increasing the smoothing scale. This repetition helps generate N-enhanced images with progressively smoother scales. The selection of N discrete smoothing scales can be determined using the following approach: $\sigma_1 = d_0/4, \sigma_2 = r\sigma_1, \dots, \sigma_N = r^{N-1}\sigma_1 = d_1/4$, where $r = (d_1/d_0)^{1/(N-1)}$. To obtain the final output and enhance or extract features at multiple scales in an image the maximum value from the N individual filters has been selected. This approach allows us to achieve a dot-enhanced structure and suppress lines-looking structure, see Fig. 3. The dot enhancement image provides boundaries of all the heads as a threshold operator is applied. On the other side, as the dot enhancement operator does not depend on the image intensity to about circle-like structures which are not part of the foreground, the image intensity inside the boundaries of the obtained objects was considered and then refine the head output by avoiding low-intensity circle-like structures. After the refinement, all the properties of the segmented heads, such as perimeters, center, area, etc., has been found. On the other hand, the segmented image of the heads can be used as an initial level set for the next step where a variational model optionally is applied to refine the watershed segmentation output of the comet's tail.

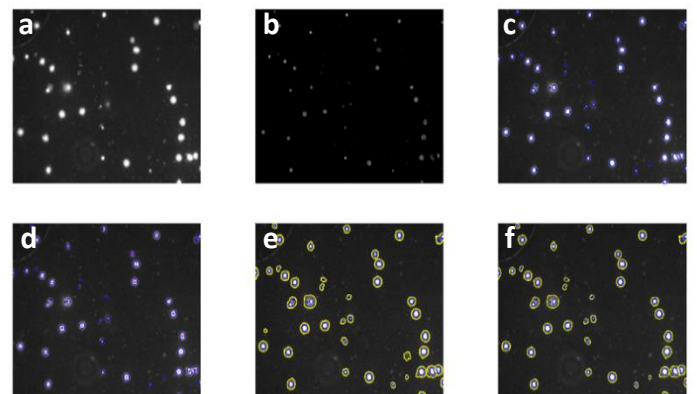


Fig. 5. Comet assay dataset samples from the original size image without cropping as commonly would be used for machine learning techniques. (a) Original image, (b) Dot enhanced image, (c) Threshold of the dot enhanced image, (d) Head center detection, (e) Segmentation of the heads, (f) Final output after refinement.

In order to proceed and get the second level of segmentation; involving the information of the tail; a standard

threshold for the obtained image followed by an opening operator with a disc structuring element of radius 3 has been used. In this way, in the case of nearby comets, one will be able to have some information on each of them separately.

2.4. Comets tail segmentation through an extended-maxima transform watershed segmentation

To perform the segmentation of the tail detection for each head, a multi-level segmentation algorithm, inspired by the work of Qin et al. (2013) and Rada et al. (2014), has been employed. The work of Rada et al. (2014), accurately delineates and separate the detected spines, circular-like structures from the background and other structures present in the image, whereas the work of Qin et al. (2013), separates the touching corn kernels used in the watershed segmentation into individual segments by enabling better analysis and measurement of each kernel. In difference with this work, the minima between the extended-maxima transform of the image and the background has been imposed. To achieve this, the extended-maxima transform of the image and the background is computed.

It is important to note that in general, the watershed algorithm tends to produce larger boundaries than the actual boundaries in case of the presence of noise. Therefore, to achieve accurate segmentation of the tail regions, a variational-based algorithm can be employed to refine the edges. This can be easily decided by the user as he evaluated the noise range of the given data.

2.4.1. Extended-maxima transform

The extended-maxima transform as a variation of the H-maxima transform in mathematical morphology is shortly summarized in the following: The H-maxima transform is used to suppress pixels above a certain intensity and extract local maxima related to target objects from a grayscale image. The Extended-Maxima Transform can calculate the regional maximum and create a binary image. In the H-maxima transformation, all maxima whose depth (intensity) is below or equal to a given threshold h are suppressed. This is achieved by performing the reconstruction of the grayscale image f from $f - h$ using dilation. Mathematically, the $HMAX_h(f)$ is defined as:

$$HMAX_h(f) = R_f^{\delta}(f - h),$$

where f represents the grayscale of the original image and h is the threshold value.

The Extended-Maxima Transform, denoted as $EMAX_h(f)$, is minima of the corresponding H-maxima transformation, which is obtained by applying regional maximum:

$$EMAX_h(f) = RMAX[H, MAX_h(f)].$$

In order to label the segments obtained from the watershed algorithm as either part of the comet assay or not, the information of the center of each comet head obtained from the previous step over the binary image has been used. Moreover, to get better information on the range of the intensity of the comet's tail, for each watershed segment image intensity of the region without the intensity of the head already segmented in the previous step has been considered. This will allow the evolution of the refinement of the variational model to find the largest region where the tail takes place.

2.4.2. Optional refinement with geodesic active contour model

In this approach, the variational function combines an edge detection function inspired by the Le Guyader and Gout (2008) approach with a region-based function similar to the Chan-Vese (CV) model proposed by Chan and Vese (2001). The level-set formulation of this variational function can be expressed as:

$$\delta_{\epsilon}(\phi(x)) \left\{ \mu \nabla \cdot \left(g(x) \frac{\nabla \phi(x)}{|\nabla \phi(x)|} \right) - \lambda ((I(x) - c_1)^2 - (I(x) - c_2)^2) \right\} = 0,$$

with μ and λ constants, $g(x)$ an edge detection image, c_1 and c_2 are the mean intensity of the image foreground and background, respectively, computed as follows:

$$g(x) = \frac{1}{1 + |\nabla I(x)|^2} \quad c_1 = \frac{\int_{\Omega} f(x) H_{\epsilon}(\phi(x))}{\int_{\Omega} H_{\epsilon}(\phi(x))} \quad c_2 = \frac{\int_{\Omega} f(x) (1 - H_{\epsilon}(\phi(x)))}{\int_{\Omega} (1 - H_{\epsilon}(\phi(x)))} dx$$

where H_{ϵ} and δ_{ϵ} represent the regularized Heaviside and the corresponding Delta function, respectively, that guarantee the derivation continuity at perpendicular jumps. In this paper, the approximation for the Heaviside and delta function is given as:

$$H_{\epsilon} = \frac{1}{2} \left(1 + \frac{\delta}{\pi} \arctan\left(\frac{x}{\epsilon}\right) \right) \quad \text{and} \quad \delta_{\epsilon} = \frac{d}{dt} H_{\epsilon}(x) = \frac{\epsilon}{\pi(\epsilon^2 + x^2)}$$

while as the first initial level set ϕ_0 it is a distance function obtained from the binary image of the head segmentation.

3. Results and discussion

In this section, the results of the output experiments that showcase the performance of the proposed comet segmentation and property extraction algorithm has been shown. Demonstrating the effectiveness of the proposed algorithm and its segmentation accuracy has been first shown. The experiments were run over the dataset provided by free available from the website <https://www.clir-lab.org/u-netcomet> and some new data by Dr. Elda Pacheco-Pantoja from Mexico Medicine School, Health Sciences Division, Universidad Anahuac Mayab. To evaluate the proposed approach, the obtained results were compared with those obtained from existing noncommercial software OpenComet (Gyori et al., 2014), and UNetComet (Ruz-Suarez et al., 2022).

The primary objective of this study is to detect heads of comets with an already-known diameter ranging from 4(d0) to 32(d1). To achieve this, dot filters with varying smoothing scales, ranging from 1 to 8, were applied across all of the experiments. The dilation and opening operator uses a standard disk structuring element size 3. The threshold used while applying the imposed minima between the extended-maxima transform of the image and the background has a value of 40. In case the variational model will be activated for the refinement, the parameters used are set to specific values: $\mu = 500$, $\lambda = 1$, and $\epsilon = 1$. The optimization of these parameters is a subject for future work and remains to be explored. Fig. 4 depicts a successful segmentation of a head and the tail of different images taken from the set of 288×288 images, achieved through the dot-enhancement-based comets-dissemble technique. The accuracy of the proposed segmentation algorithm was assessed by comparing its results with manual delineations provided by a domain expert. To measure the similarity between the

algorithm's output and the manual delineations, the Dice coefficient, as introduced by Dice et al. in 1945, has been employed. Dice coefficient ranges from 0 to 1, with 1 indicating a perfect match. After evaluating 40 different comets, their respective Dice coefficients were calculated. On average, the algorithm achieved a Dice coefficient of 0.843, with a minimum value of 0.671 and a maximum value of 0.986. The results show a high segmentation accuracy, with the algorithm closely matching the expert manual delineations.

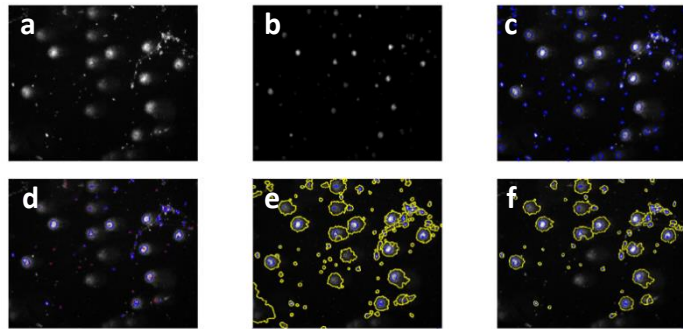


Fig. 6. Second example of comet assay dataset samples from the original size image without cropping as commonly would be used for machine learning techniques. (a) Original image, (b) Dot enhanced image, (c) Threshold of the dot-enhanced image, (d) Head center detection, (e) Segmentation of the tail, (f) Final output after refinement.

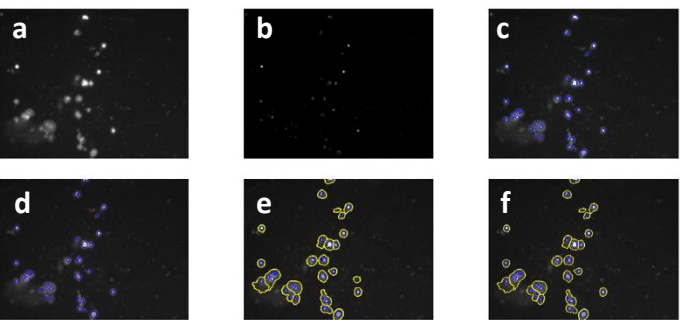


Fig. 7. Third example of comet assay dataset samples from the original size image without cropping as commonly would be used for machine learning techniques. (a) Original image, (b) Dot enhanced image, (c) Threshold of the dot-enhanced image, (d) Head center detection, (e) Segmentation of the tail, (f) Final output after refinement.

Fig. 5 - 7 are showcases of the qualitative segmentation outputs obtained by the proposed model during the validation phase. The samples are the originally taken images without cropping as commonly would be used for machine learning techniques. It can be observed that pixels for the head and the tail of the comets are classified accurately. All those figures provide examples demonstrating the successful partitioning of two overlapping comets which other methods will fail as shown in the following. In all the figures the original image (a), dot enhancement output (b) followed by the head segmentation, and head center detection (d), which will play a role in the refinement of the tails as part of a comet or not, tail segmentation using extended-maxima transform watershed segmentation (e), and the last figure showing the accurate segmentation of the tail and head of comets has been shown.

It can be easily seen from those figures that the proposed model does not have difficulty running with a high accuracy in each of the images. The time to process each image is at most 20 seconds per image.

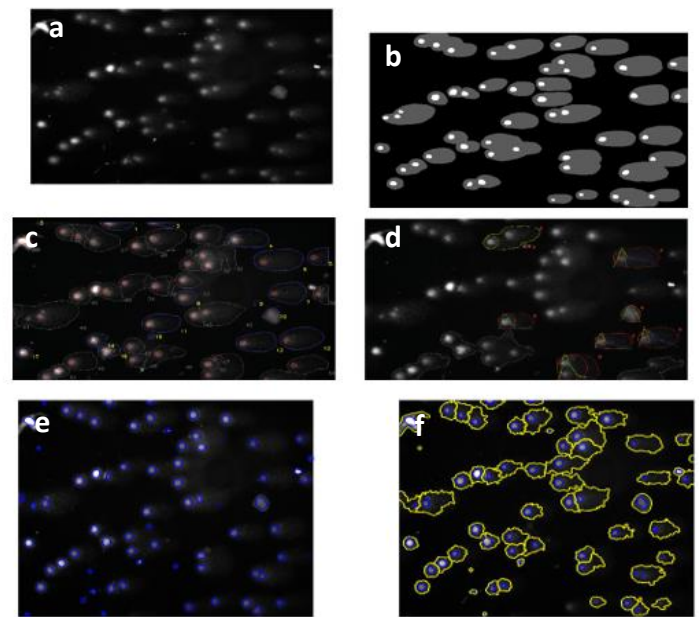


Fig. 8. Comet assay dataset samples from the original size image. (a) Original image, (b) Annotated image by experts, (c) UnetComet segmentation, (d) OpenComet segmentation, (e) Head segmentation with the proposed model, (f) Final output of the proposed model.

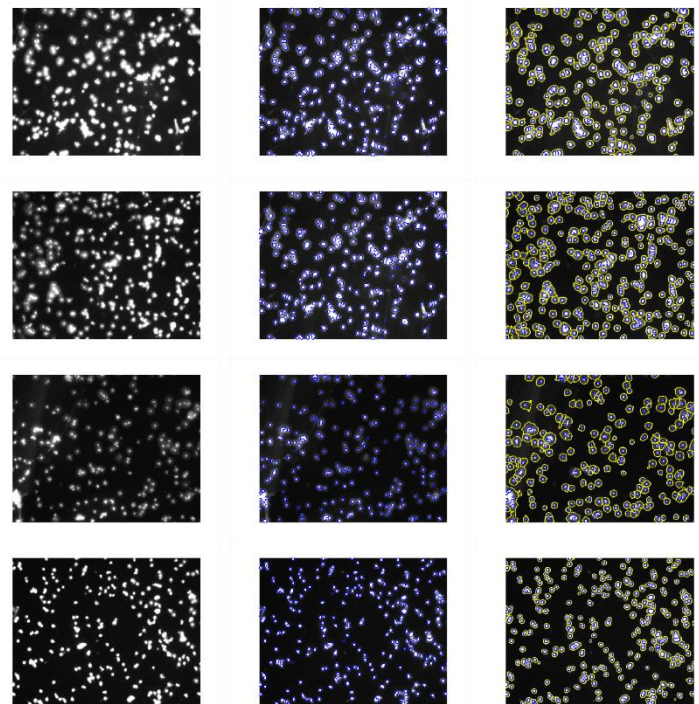


Fig. 9. Successful segmentation of comet heads and tails for superimposed comets.

To evaluate the performance of the proposed algorithm, comparison experiments were conducted against a state-of-the-art system called OpenComet (Gyori et al., 2014), and UNetComet (Ruz-Suarez et al., 2022).

In order to compare the segmentation results of both systems in comparison with the proposed algorithm, hard cases, with images that safer from low quality as well as merged comets, were considered. The objective of this process is to identify the estimated boundaries of superimposed comets and separate them into individual comets.

As it can be observed from Fig. 8 segmentation results obtained from both systems fail in a high-accuracy segmentation. The OpenComet system shows low performance whereas though the UnetComet performs relatively well one can see that UnetComet will over-segment objects such as comets number 45, 47, and 50 in Fig. 8 (c). Similar to this example UnetComet will over-segment or miss to segment comets in cases as shown in Fig. 9.

As part of this study, extremely hard cases, where not only superimposed comets appear as part of the images but at the same time the image is of low quality due to distortion, were considered.

As shown in Fig. 10 the proposed algorithm is not successful. This is going to be a motivation for the future work where dehazing and deblurring techniques can be hired for such cases as an image preprocessing technique.

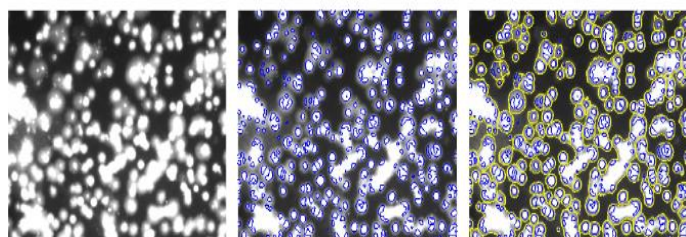


Fig. 10. Fail of the proposed system to be considered as future work.

References

- Afiyahayati A. E., Yanuarieska R. D., & Mulyana, S. (2022). GamaComet: A deep learning-based tool for the detection and classification of DNA damage from buccal mucosa comet assay images. *Diagnostics (Basel)*, 12(8), 2002.
- Chan, T. F., & Vese, L. A. (2001). Active contours without edges. *IEEE Transactions on Image Processing*, 10, 266-277.
- Chatterjee, N., & Walker, G. C. (2017). Mechanisms of DNA damage, repair, and mutagenesis. *Environmental and Molecular Mutagenesis*, 58(5), 235-263.
- Dice, L. R. (1945). Measures of the amount of ecologic association between species. *Ecology*, 26, 297-302.
- Fairbairn, D. W., Olive, P. L., & O'Neill, K. L. (1995). The comet assay: a comprehensive review. *Mutation Research/Reviews in Genetic Toxicology*, 339, 37-59.
- Ganapathy, S., Muraleedharan, A., Sathidevi, P. S., Chand, P., & Rajkumar, R. P. (2016). CometQ: An automated tool for the detection and quantification of DNA damage using comet assay image analysis. *Computer Methods and Programs in Biomedicine*, 133, 143-154.
- Le Guyader, C., & Gout, C. (2008). Geodesic active contour under geometrical conditions: Theory and 3D applications. *Numerical algorithms*, 48, 105-133.
- Gyori, B. M., Venkatachalam, G., Thiagarajan, P., Hsu, D., & Clement, M. V. (2014). OpenComet: An automated tool for comet assay image analysis. *Redox Biology*, 2, 457-465.
- Hafiyani, Y. T., Yanuarieska, R. D., Anarossi, E., Sutanto, V. M., Triyanto, J., & Sakakibara, Y. (2021). A hybrid convolutional neural network-extreme learning machine with augmented dataset for DNA damage classification using comet assay from buccal mucosa sample. *International Journal of Innovative Computing, Information and Control*, 17(4), 1191-11201.
- Helmma, C., & Uhl, M. (2000). A public domain image-analysis program for the single-cell gel-electrophoresis (comet) assay. *Mutagenesis*, 466, 9-15.
- Lee, T., Lee, S., Sim, W. Y., Jung, Y. M., Han, S., Won, J. H., ... & Yoon, S. (2018). HiComet: a high-throughput comet analysis tool for large-scale DNA damage assessment. *BioMed Central Bioinformatics*, 19(1), 49-61.
- Li, Q., Sone, S., & Doi, K. (2003). Selective enhancement filters for nodules, vessels, and airway walls in two-and three-dimensional CT scans. *Medical Physics*, 30, 2040-2051.
- Lindeberg, T. (1998). Feature detection with automatic scale selection. *International Journal of Computer Vision*, 30, 77-116.
- Ostling, O., & Johanson, K. (1984). Microelectrophoretic study of radiation-induced DNA damages in individual mammalian cells. *Biochemical and Biophysical Research Communications*, 123, 291-298.
- Qin, Y., Wang, W., Liu, W., & Yuan, N. (2013). Extended-maxima transform watershed segmentation algorithm for touching corn kernels. *Advances in Mechanical Engineering*, 5, 268046.
- Rada, L., Erdil, E., Argunsah, A. O., Unay, D., & Cetin, M. (2014). Automatic dendritic spine detection using multiscale dot enhancement filters and sift features. *2014 IEEE International Conference on Image Processing (ICIP)*, Paris, France, 26-30.
- Ruz-Suarez, D., Martin-Gonzalez, A., Brito-Loeza, C., & Pacheco-Pantoja, E. L. (2022). Convolutional neural network for segmentation of single cell gel electrophoresis assay. In: Brito-Loeza C., Martin-Gonzalez A., Castañeda-Zeman V., Safi A. (eds) *International Symposium on Intelligent Computing Systems* (pp. 57-68). Cham: Springer International Publishing.
- Singh, N. P., McCoy, M. T., Tice, R. R., & Schneider, E. L. (1988). A simple technique for quantitation of low levels of DNA damage in individual cells. *Experimental Cell Research*, 175(1), 184-191.
- Taye, M. M. (2023). Understanding of machine learning with deep learning: architectures, workflow, applications and future directions. *Computers*, 12(5), 91.
- Uthirapathy, S. (2023). Cytostatic effects of avocado oil using single-cell gel electrophoresis (comet assay). *Aro-The Scientific Journal of Koya University*, 11(1), 16-21.

Cite as: Rada Ulgen, L. (2023). Automated comet assay segmentation using combined dot enhancement filters and extended-maxima transform watershed segmentation. *Front Life Sci RT*, 4(2), 92-98.



Research article

Infuse herbal oils: a comparative study of wheat germ and tomato seed oils

Firat Baris Barlas^{*1,2} ¹ Istanbul University-Cerrahpasa, Institute of Nanotechnology and Biotechnology, 34500, Istanbul, Türkiye² Health Biotechnology Joint Research and Applications Center of Excellence, 34220, Istanbul, Türkiye

Abstract

The use of traditional herbal medicine products has recently been revived, with special emphasis on the use of herbal oils in non-invasive wound treatment. Extraction conditions are very important in seed oils and especially suitable temperatures at which the extraction process is carried out. It is vital for the preservation of primary and secondary metabolites. In this study, wheat germ (WG) was collected from the Central Anatolia Region and tomato seed (TS) was collected from the Aegean Region. Oils were obtained from these two seeds by cold pressing and their infused forms (WGO-TSO) were prepared. To investigate the *in vitro* activities of these study groups, cytotoxicity, wound healing, and antioxidant capacity tests were performed on HaCaT (Human keratinocyte) and Vero (Monkey kidney fibroblast-like) cell lines. According to the results of the intracellular cytotoxicity analysis, a common dose of 25 µg/mL was determined to be non-toxic for all groups, and this dose was then used as the working dose. Antioxidant capacity studies, in cells under oxidative stress with hydrogen peroxide, yielded positive results for all working groups and the WGO/TSO group showed statistically superior outcomes. In addition, similar results were obtained in wound healing experiments. As a result, using oils in the form of infusion may be more effective in combating oxidative stress and promoting wound healing than using oil alone.

Keywords: Antioxidant capacity; cell culture; infuse oils; wound healing

1. Introduction

Mankind has used plant-derived ingredients in the treatment of diseases since ancient times. Due to their natural antibacterial, antifungal, and wound-healing properties, they played an important role in the survival of people in these times (Shankar and Liao, 2004; Allaw et al., 2021). After the discovery of modern antibiotics and the subsequent side effects and resistance problem, there is a return to herbal ingredients (Munuswamy et al., 2013). In addition, the fact that herbal materials are cheap, have fewer side effects, and have a high variety of active substances attracts the attention of researchers (Budala et al., 2023).

Traditional medicine relies on experience and natural ingredients, especially herbal ingredients. Seed oils and their derivatives, such as creams, soaps, and liposomes, have been

extensively used in the treatment of wound healing and dermatological diseases to prevent infection and promote rapid tissue repair without scarring (Ahmad et al., 2013; Ehterami et al., 2019). While plant extracts or oils have demonstrated therapeutic activity on their own, combining them with other biologically active substances can produce even more effective products through a synergistic or additive effect (Khan et al., 2022; Razzaq et al., 2022). As a result, the flavonoid and phenolic compound content of herbal sources can be enhanced and diversified by mixing different sources together.

The tomato (*Solanum lycopersicum*) is an edible berry and one of the most widely cultivated crops that are used for human nutrition around the world. The tomato, a species with origins in western South America, Mexico, and Central America, was first encountered by the Spanish following their contact with the Aztecs. During the 16th century, the plant was brought to Europe

* Corresponding author.

E-mail address: fbarlas@iuc.edu.tr (F. B. Barlas).

<https://doi.org/10.51753/flsrt.1313038> Author contributions

Received 11 June 2023; Accepted 03 August 2023

Available online 26 August 2023

2718-062X © 2023 This is an open access article published by Dergipark under the [CC BY](https://creativecommons.org/licenses/by/4.0/) license.

by the Spanish, marking its introduction to the continent. They contain important compounds like lycopene (LYC) (Machmudah et al., 2012; Osmá et al., 2012). Lycopene belongs to the family of carotenoids, which have been shown to have health benefits such as anti-inflammatory, antioxidant, anti-microbial, neuroprotective, and cardiovascular disease prevention (Hung et al., 2008; Shakir et al., 2018; Przybylska, 2020; Binsuwaidan et al., 2022; Przybylska and Tokarczyk, 2022). Also, there are so many studies about lycopene and tomato processing industries produce a large amount of waste, including tomato pomace, which is typically used as animal feed or disposed of as solid waste and the seeds of tomatoes also contain oil that is high in lycopene and beta-carotene, which are important nutrients (Gumus et al., 2020).

Triticum aestivum L., commonly known as wheat, has been a significant part of human evolution and continues to serve as a staple food source for humanity. The utilization of wheat extends beyond human consumption and encompasses the production of oil and feed. Wheat germ oil (WGO), a specialty product derived from wheat, is rich in vitamin E and tocopherols, particularly Alpha-tocopherol (α -TOH). The α -TOH, which is one of the most common tocopherols in WGO, has been the subject of many studies today. Numerous medical properties have been discovered in the light of these studies, including anti-diabetic, anti-inflammatory, anti-microbial and anti-nephrotoxic activities (Lee et al., 2004; Ajith et al., 2007; Harrabi et al., 2021; Liu et al., 2021; Guven et al., 2022). Removal of wheat germ during flour production from wheat is a common process, while WGO to be produced from it has high medicinal properties. This product is known for its high concentration of vitamin E and tocopherol, making it a valuable ingredient in a variety of applications (Catzeddu et al., 2023).

In this research text, cold-pressed oils were obtained from wheat germ and tomato seeds, and infused versions of these oils were prepared. Then, cytotoxicity, antioxidant capacity, and wound healing experiments were performed with these formulations, and the results were compared with the control groups. The objective of this study was to identify the most biologically active formulation.

2. Materials and methods

2.1. Material

MTT (3-(4,5-Dimethylthiazol-2-yl)-2,5-Diphenyltetrazolium Bromide), H₂O₂ (Hydrogen Peroxide Solution 30 % (w/w) in H₂O), DMSO (Dimethyl sulfoxide, cell culture grade), DMEM (Dulbecco's Modified Eagle Medium), PBS (Phosphate Buffered Saline, pH:7.4), FBS (Fetal Bovine Serum), P/S (Penicillin/Streptomycin) purchased from Sigma Aldrich. Ultra-pure water (Millipore), Microplate Readers (Thermo Fisher Scientific), inverted microscope (Leica).

2.2. Sampling

Wheat germ oil (WGO), tomato seed oil (TSO) and their mix oils obtained by cold-press extraction (CPE) were produced in different regions in Türkiye and were kindly donated from EGE-LS (Türkiye). Tomato seeds (TS) were obtained from İzmir (Aegean Region), and wheat germ (WG) was purchased from Konya city (Central Anatolia Region). Three different working groups were formed, WGO, TSO and WGO/TSO (v/v).

2.3. Cell culture studies

To investigate the biological activities of the samples, two cell lines were utilized: HaCaT (Human keratinocyte from ATCC) and Vero (Monkey kidney fibroblast cell from ATCC). These cell lines were maintained in a humidified incubator set at 37°C with 5.0% CO₂, using DMEM as the growth medium. The DMEM was supplemented with 10% FBS, 100 UI/mL Penicillin/Streptomycin, and 2.0 mM L-Glutamine to ensure optimal cell growth. The cells were sub-cultured twice a week by trypsinization when they reached 70% confluence.

2.3.1. Cell viability

In this study, by following the method used by Barlas et al. (2019), 8000 HaCaT and Vero cells were grown in a 96-well plate (37°C, 5% CO₂, and 95% humidity) in a controlled environment for 48 hours. At the end of this period, the normal medium was removed from the cells and added to the medium containing the working groups. Subsequently, a solution of MTT was added to each well and incubated for 4 hours. The living cells convert MTT into formazan crystals, which are insoluble in the MTT solution. The number of living cells was quantified by measuring the absorbance of the solution at 570 nm and 630 nm reference wavelengths. The control group in the assay consisted of cells treated only with DMEM, which were considered to be 100% viable. The relative cell viability of the sample-treated cells was then calculated as a percentage of the absorbance of the control group. The results were reported as the mean of four replicates.

2.3.2. Scratch assay for wound healing

The *in vitro* wound healing assay was used to assess the cell migration ability, or the capacity of cells to move towards and fill in a damaged area. Two monolayer cell line, HaCaT and Vero cells were cultivated in 24-well plates and waited to grow into a confluent. Then, a wound was created by gently scratching the cells using a pipette tip. The cells at the edge of the wound were expected to move towards the opening and close it until new cell-cell contacts were established. After the wound was formed, various samples were added to the wells, and the scratch area was documented at different time intervals (1st, 4th, and 8th hours) using an inverted microscope equipped with a CCD camera. Migration in the cavity of the cell monolayer was photographed and then using a computer program (ImageJ) the results were calculated as percent migration compared to the control group. The results were reported as the mean of three replicates (Liang et al., 2007; Roy et al., 2023).

2.3.3. Antioxidant activity

Here is a description of the cell-based hydrogen peroxide (H₂O₂) assay without numbered steps or individual items described by Guler et al., (2014). H₂O₂ stimulated antioxidant capacity test is a frequently used method. According to this experiment, the cells are first left to pre-incubate with the samples for two hours, then certain doses of H₂O₂ are added to see how much this stress is prevented by viability tests. For this purpose, 8000 HaCaT and Vero cells were seeded in 96-well plates and incubated for 48 hours under normal cell culture conditions. Then, the media were drawn from them and incubated

ted for two hours with the study media containing the samples. After this pre-treatment, 1.25 mM H₂O₂ was added to the cells and incubated for 24 hours. At the end of the period, cell viability was measured with the MTT method. The results are calculated and compared with the control groups to determine the antioxidant activity of the sample.

2.4. Statistical analysis

All statistical analyses were performed using one-way analysis of variance (ANOVA) and Tukey multiple comparison test with the help of GraphPad 5 Prism software. The results were presented as the mean and standard deviation. The significance of the comparison between groups was determined by a *p* value of less than 0.05.

3. Results and discussion

The cell viability analyse was performed with MTT method on HaCaT and Vero cell lines to evaluate cytotoxicity and dose dependent effect of samples. Cells were treated with samples at different doses and then allowed to incubate for 24 hours. Subsequently, cell viability was measured by the MTT method and non-cytotoxic doses were determined and used in subsequent studies. The MTT assay was performed to evaluate the cell viability of the samples in two different cell lines (HaCaT and Vero). The results, depicted in Fig. 1, showed that the cell viability for WGO, WGO-TSO, and TSO at a dose of 25 µg/mL was 100.025 ± 1.214, 100.025 ± 1.671, and 101.921 ± 2.671, respectively, in the HaCaT cell line compared to the control group. In the Vero cell line, the cell viability was 105.32 ± 5.029, 105.32 ± 4.083, and 114.364 ± 1.957, respectively. Based on these results, the dose of 25 µg/mL was selected as the study dose as it did not demonstrate high proliferative effects and was not toxic for all groups.

Cell-based antioxidant activity was assayed on the cells those are exposed to hydrogen peroxide destruction. The cells were pre-treated with seed oils 2 h before and then, treated with 100 mM hydrogen peroxide and allowed to incubate for 24 h. Afterwards, viability was measured, and comparisons were made between the groups (Fig. 2). The results showed that the viability of the HaCaT cell line decreased to 48.314 ± 3.00 when exposed to hydrogen peroxide (H₂O₂) alone. However, the viability of WGO, WGO-TSO, and TSO remained at the levels of 61.240 ± 4.565, 71.832 ± 3.691, and 60.279 ± 2.914, respectively. In the Vero cell line, the viability decreased to 50.738 ± 4.096 with H₂O₂ alone, whereas the viability of WGO, WGO-TSO, and TSO remained at the levels of 61.384 ± 3.227, 69.201 ± 3.217, and 60.940 ± 4.258, respectively. Antioxidant activity assays have shown that the mixture of seed and oils is more effective against to the oxidative stress compared to their use alone (Fig. 2). α-TOH present in wheat germ oils constitute the most important part of the antioxidant capacities. Also, the antioxidant properties of the tomato seed oil are well known because of LYC (Barnes, 1982; Eller et al., 2010; Kumar et al. 2023). Furthermore, cold pressed oils may contain higher level of lipophilic phytochemicals including important natural components and biologically active compounds. Also, these oils are free from chemical contamination (Yuenyong et al., 2021; Sumara et al., 2023).

The scratch assay is a commonly used method in the field of tissue regeneration for evaluating the migration of cells across a wounded area. This assay is particularly important for studying the roles of keratinocytes and fibroblast cells in the process of tissue repair. In this study, a gap was opened with a 100 µM pipette and photographs were taken at three different time points (0, 4, and 8 hours). As can be seen in Fig. 3, the migrations of the cells were found by comparison with the control groups with the help of the image j program. Considering the measurements made after 8 hours, the cell migration rate for the HaCaT cell

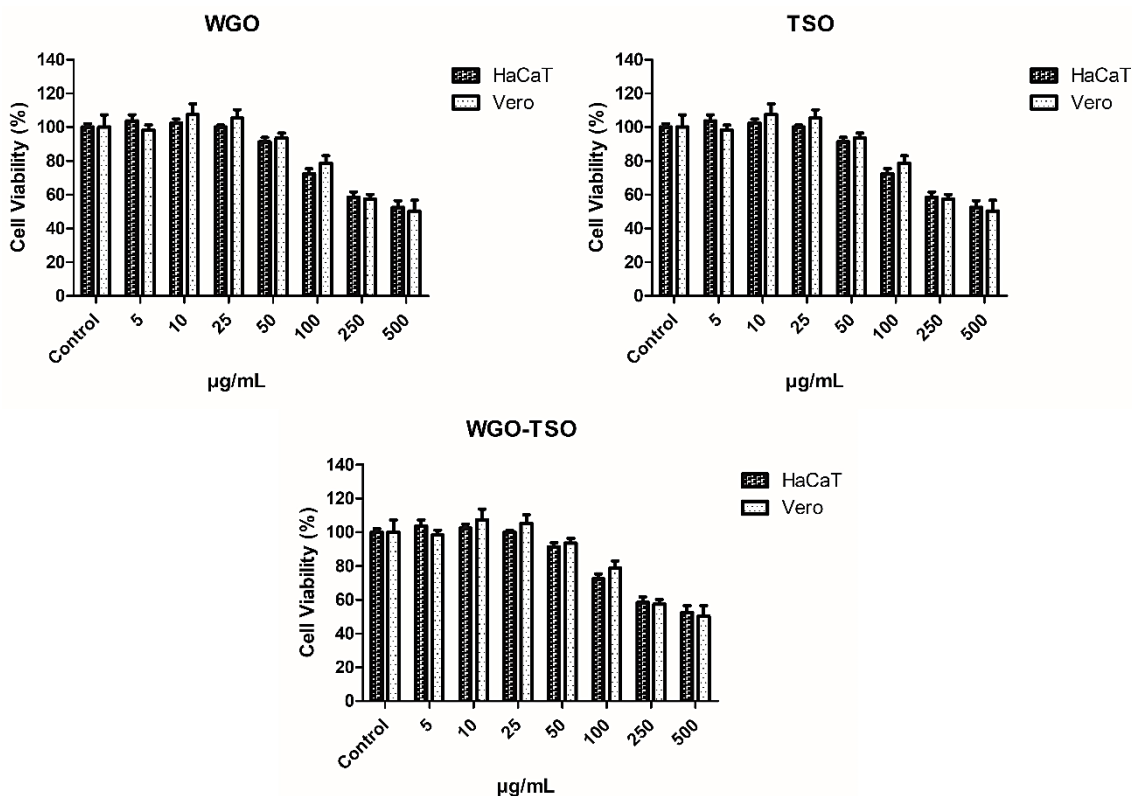


Fig. 1. *In vitro* cytotoxicity effect of seed oils and infuse form on HaCaT and Vero cell lines.

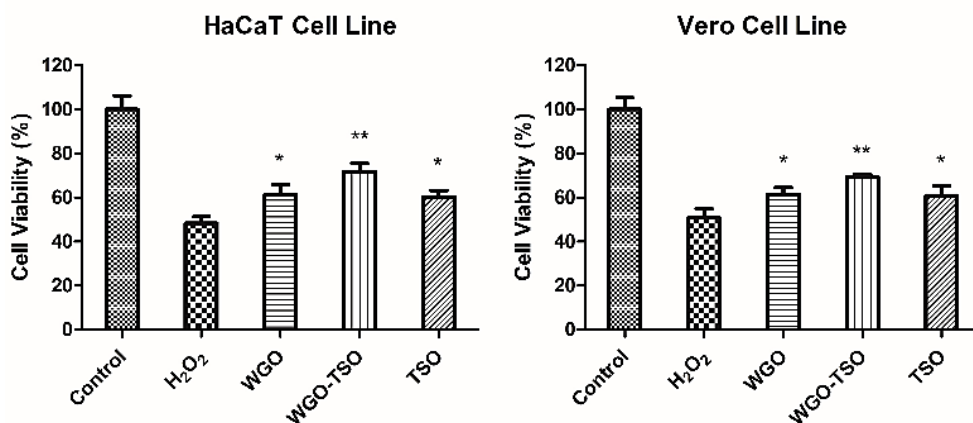


Fig. 2. Effect of seed oils and their infuse form on hydrogen peroxide-induced oxidative stress.

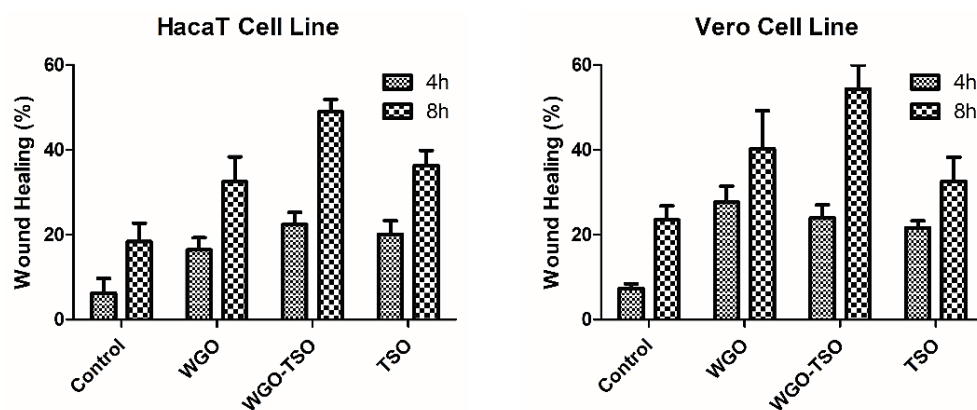


Fig 3. The wound healing effect of seed oils and infuse form on HaCaT and Vero cell lines.

line was 18.3741 ± 4.371 in the control group. On the other hand, it is 32.4700 ± 5.914 , 48.9915 ± 2.902 and 36.2790 ± 3.574 for WGO, WGO-TSO and TSO, respectively. for the Vero cell line at the same time, the control group had a migration rate of $23,4850 \pm 3,278$, while it was 40.2280 ± 8.996 , 54.3470 ± 5.614 and 32.6180 ± 5.672 for WGO, WGO-TSO and TSO, respectively. In light of the scratch assay results, it is observed that the use of seed oils in an infused form gives more successful results than using them alone. This is evidenced by the increased migration rates observed in the WGO, WGO-TSO, and TSO treatment groups compared to the control group. These findings show that seed oils and their combination have a beneficial effect on wound healing and have great potential to be a potential therapeutic option in the field of tissue regeneration. In previous studies, wheat germ oil and tomato germ oil have been extensively studied for potential health benefits such as lowering blood cholesterol levels, improving physical strength, promoting healing, exhibiting antioxidant wound activity, and anti-aging therapeutic effects have been reported (Malecka, 2002; Ghafoor et al., 2017; Zahid et al., 2019). Some studies have reported that combining oils is more effective than using them individually, similar to our results (El-Marasy et al., 2012). Additionally, for these oils used, a combination of intracellular activities of key components such as Alpha-tocopherol (α -TOH) and lycopene (LYC) may be more effective. Furthermore, the synergistic effects of minor compounds in oils from both plants may contribute to improved wound healing and antioxidant properties of the combined use of seed oils (Zaid and Al Ramahi,

2019; Bengi et al., 2022).

4. Conclusion

In this study, infused oils (WGO-TSO) (v/v) were prepared from a mixture of cold-pressed wheat germ oil (WGO) and tomato seed oil (TSO) in equal volumes. Then, *in vitro* cytotoxicity analyses of these samples were examined in two different cell lines (HaCaT and Vero). As a result of this study, $25\mu\text{g}/\text{mL}$ was chosen as the working dose. After that, *in vitro* antioxidant capacity test was evaluated with hydrogen peroxide stimulation, and wound healing studies were evaluated with scratch assay. In light of the results, it was determined that infused oils showed better therapeutic effects than the use of oils alone. As a result, they exhibit a synergistic effect in combinations of active and minor compounds found in WGO and TSO. This suggests that the use of infused forms of seed oils is more promising for medical and cosmetic applications.

Acknowledgment: The author is grateful to EGE-LS company for providing cold-pressed seed oils.

Conflict of interest: The author declares that he has no conflict of interests.

Informed consent: The author declares that this manuscript did not involve human or animal participants and informed consent was not collected.

References

- Ahmad, A., Husain, A., Mujeeb, M., Khan, S. A., Najmi, A. K., Siddique, N. A., Damanhour, Z. A., & Anwar, F. (2013). A review on therapeutic potential of *Nigella sativa*: A miracle herb. *Asian Pacific Journal of Tropical Biomedicine*, 3(5), 337-352.
- Ajith, T., Usha, S., & Nivitha, V. (2007). Ascorbic acid and α -tocopherol protect anticancer drug cisplatin induced nephrotoxicity in mice: a comparative study. *Clinica Chimica Acta*, 375(1-2), 82-86.
- Allaw, M., Manconi, M., Caboni, P., Bacchetta, G., Escribano-Ferrer, E., Peris, J. E., Nacher, A., Diez-Sales, O., & Manca, M. L. (2021). Formulation of liposomes loading lentisk oil to ameliorate topical delivery, attenuate oxidative stress damage and improve cell migration in scratch assay. *Biomedicine and Pharmacotherapy*, 144, 112351.
- Barlas, F., Celikbas, E., Arslan, M., Timur, S., & Yagci, Y. (2019). Gold nanoparticle conjugated poly (p-phenylene- β -cyclodextrin)-graft-poly (ethylene glycol) for theranostic applications. *Journal of Applied Polymer Science*, 136(12), 47250.
- Barnes, P. (1982). Lipid composition of wheat germ and wheat germ oil. *Fette, Seifen, Anstrichmittel*, 84(7), 256-269.
- Bengi V, U., Saygun, I., Bal, V., Ozcan, E., Kose Ozkan, C., Torun, D., Avcu, F., & Kantarci, A. (2022). Effect of antioxidant lycopene on human osteoblasts. *Clinical Oral Investigations*, 1-7.
- Binsuwaideen, R., Sultan, A. A., Negm, W. A., Attallah, N. G., Alqahtani, M. J., Hussein, I. A., Shaladam, M. A., El-Sherbeni, S. A., & Elekhaway, E. (2022). Bilosomes as nanoplatform for oral delivery and modulated *in vivo* antimicrobial activity of lycopene. *Pharmaceuticals*, 15(9), 1043.
- Budala, D. G., Martu, M. A., Maftai, G. A., Diaconu-Popa, D. A., Danila, V., & Luchian, I. (2023). The role of natural compounds in optimizing contemporary dental treatment-current status and future trends. *Journal of Functional Biomaterials*, 14(5), 273.
- Catzeddu, P., Fois, S., Tolu, V., Sanna, M., Braca, A., Vitangeli, I., ... & Roggio, T. (2023). Quality evaluation of fresh pasta fortified with sourdough containing wheat germ and wholemeal semolina. *Foods*, 12(14), 2641.
- Ehterami, A., Salehi, M., Farzamfar, S., Samadian, H., Vaez, A., Ghorbani, S., Ai, J., & Sahraeyma, H. (2019). Chitosan/alginate hydrogels containing Alpha-tocopherol for wound healing in rat model. *Journal of Drug Delivery Science and Technology*, 51, 204-213.
- El-Marasy, S. A., El-Shenawy, S. M., El-Khatib, A. S., El-Shabrawy, O. A., & Kenawy, S. A. (2012). Effect of *Nigella sativa* and wheat germ oils on scopolamine-induced memory impairment in rats. *Bulletin of Faculty of Pharmacy, Cairo University*, 50(2), 81-88.
- Eller, F., Moser, J., Kenar, J., & Taylor, S. (2010). Extraction and analysis of tomato seed oil. *Journal of the American Oil Chemists' Society*, 87, 755-762.
- Ghafoor, K., Özcan, M. M., AL-Juhaimi, F., Babiker, E. E., Sarker, Z. I., Ahmed, I. A. M., & Ahmed, M. A. (2017). Nutritional composition, extraction, and utilization of wheat germ oil: A review. *European Journal of Lipid Science and Technology*, 119(7), 1600160.
- Guler, E., Barlas, F. B., Yavuz, M., Demir, B., Gumus, Z. P., Baspinar, Y., Coskunol, H., & Timur, S. (2014). Bio-active nanoemulsions enriched with gold nanoparticle, marigold extracts and lipoic acid: *In vitro* investigations. *Colloids and Surfaces B: Biointerfaces*, 121, 299-306.
- Gumus, Z. P., Argon, Z. U., Celenk, V. U., & Timur, S. (2020). Cold pressed tomato (*Lycopersicon esculentum* L.) seed oil. In: Ramadan M. F. (ed) *Cold pressed oils* (pp. 449-458). Elsevier.
- Güven, H., Durmus, N., Hocaoglu, N., Guner, O., Acar, S., Akan, P., & Calan, O. G. (2022). Protective effects of wheat germ oil against erectile and endothelial dysfunction in streptozotocin-induced diabetic rats. *International Journal of Impotence Research*, 34(6), 581-587.
- Harrabi, S., Ferchichi, A., Fellah, H., Feki, M., & Hosseinian, F. (2021). Chemical composition and *in vitro* anti-inflammatory activity of wheat germ oil depending on the extraction procedure. *Journal of Oleo Science*, 70(8), 1051-1058.
- Hung, C.-F., Huang, T.-F., Chen, B.-H., Shieh, J.-M., Wu, P.-H., & Wu, W.-B. (2008). Lycopene inhibits TNF- α -induced endothelial ICAM-1 expression and monocyte-endothelial adhesion. *European Journal of Pharmacology*, 586(1-3), 275-282.
- Khan, Z. A., Prabhu, N., Ahmed, N., Lal, A., Issrani, R., Maqsood, A., Vohra, F., & Alam, M. K. (2022). A comparative study on alvogy and a mixture of black seed oil and powder for alveolar osteitis: a randomized double-blind controlled clinical trial. *International Journal of Clinical Practice*, 2022.
- Kumar, M., Sharma, D., & Singh, V. P. (2023). Modulation of the chain-breaking antioxidant activity of phenolic organochalcogens with various co-antioxidants at various pH values. *Organic & Biomolecular Chemistry*, 21(6), 1316-1327.
- Lee, C. H., An, D. S., Lee, S. C., Park, H. J., & Lee, D. S. (2004). A coating for use as an antimicrobial and antioxidative packaging material incorporating nisin and α -tocopherol. *Journal of Food Engineering*, 62(4), 323-329.
- Liang, C. C., Park, A. Y., & Guan, J. L. (2007). *In vitro* scratch assay: a convenient and inexpensive method for analysis of cell migration *in vitro*. *Nature Protocols*, 2(2), 329-333.
- Liu, R., Xu, Y., Chang, M., Tang, L., Lu, M., Liu, R., Jin, Q., & Wang, X. (2021). Antioxidant interaction of α -tocopherol, γ -oryzanol and phytosterol in rice bran oil. *Food Chemistry*, 343, 128431.
- Machmudah, S., Winardi, S., Sasaki, M., Goto, M., Kusumoto, N., & Hayakawa, K. (2012). Lycopene extraction from tomato peel by-product containing tomato seed using supercritical carbon dioxide. *Journal of Food Engineering*, 108(2), 290-296.
- Małecka, M. (2002). Antioxidant properties of the unsaponifiable matter isolated from tomato seeds, oat grains and wheat germ oil. *Food Chemistry*, 79(3), 327-330.
- Munuswamy, H., Thirunavukkarasu, T., Rajamani, S., Elumalai, E. K., & Ernest, D. (2013). A review on antimicrobial efficacy of some traditional medicinal plants in Tamilnadu. *Journal of Acute Disease*, 2(2), 99-105.
- Przybylska, S. (2020). Lycopene—a bioactive carotenoid offering multiple health benefits: a review. *International Journal of Food Science & Technology*, 55(1), 11-32.
- Przybylska, S., & Tokarczyk, G. (2022). Lycopene in the prevention of cardiovascular diseases. *International Journal of Molecular Sciences*, 23(4), 1957.
- Razzaq, L., Abbas, M. M., Miran, S., Asghar, S., Nawaz, S., Soudagar, M. E. M., Shaukat, N., Veza, I., Khalil, S., & Abdelrahman, A. (2022). Response surface methodology and artificial neural networks-based yield optimization of biodiesel sourced from mixture of palm and cotton seed oil. *Sustainability*, 14(10), 6130.
- Roy, I., Magesh, K. T., Sathyakumar, M., Sivachandran, A., Purushothaman, D., & Aravindhan, R. (2023). Evaluation of wound healing property of the ethanolic extract of glycyrrhiza glabra on vero cell lines using *in vitro* scratch assay test. *Journal of Pharmacy and Bioallied Sciences*, 15(Suppl 1), S630-S635.
- Osma, E., Ozyigit, I. I., Leblebici, Z., Demir, G., & Serin, M. (2012). Determination of heavy metal concentrations in tomato (*Lycopersicon esculentum* Miller) grown in different station types. *Romanian Biotechnological Letters*, 17(1), 6962-6974.
- Sumara, A., Stachniuk, A., Trzpił, A., Bartoszek, A., Montowska, M., & Fornal, E. (2023). LC-MS metabolomic profiling of five types of unrefined, cold-pressed seed oils to identify markers to determine oil authenticity and to test for oil adulteration. *Molecules*, 28(12), 4754.
- Shakir, S. K., Irfan, S., Akhtar, B., Rehman, S. U., Daud, M. K., Taimur, N., & Azizullah, A. (2018). Pesticide-induced oxidative stress and antioxidant responses in tomato (*Solanum lycopersicum*) seedlings. *Ecotoxicology*, 27, 919-935.
- Shankar, K., & Liao, L. P. (2004). Traditional systems of medicine. *Physical Medicine and Rehabilitation Clinics*, 15(4), 725-747.
- Yuenyong, J., Pokkanta, P., Phuangsaichai, N., Kittiwachana, S., Mahatheeranon, S., & Sookwong, P. (2021). GC-MS and HPLC-DAD analysis of fatty acid profile and functional phytochemicals in fifty cold-pressed plant oils in Thailand. *Heliyon*, 7(2), e06304.
- Zahid, S., Khalid, H., Ikram, F., Iqbal, H., Samie, M., Shahzadi, L., Shah, A. T., Yar, M., Chaudhry, A. A., & Awan, S. J. (2019). Bi-layered α -tocopherol acetate loaded membranes for potential wound healing and skin regeneration. *Materials Science and Engineering: C*, 101, 438-447.
- Zaid, A. N., & Al Ramahi, R. (2019). Depigmentation and anti-aging treatment by natural molecules. *Current Pharmaceutical Design*, 25(20), 2292-2312.

Cite as: Barlas, F. B. (2023). Infuse herbal oils: a comparative study of wheat germ and tomato seed oils. *Front Life Sci RT*, 4(2), 99-104.



Review article

Important extremophilic model microorganisms in astrobiology

Simge Emlik^{*1} , Sevgi Marakli¹ 

¹ Yildiz Technical University, Faculty of Arts and Sciences, Department of Molecular Biology and Genetics, 34220, Istanbul, Türkiye

Abstract

Humankind has been curious about the sky and beyond since its existence. Since the most primitive times, researchers have been trying to find answers to this curiosity. In recent years, a relatively new discipline, astrobiology, has emerged to answers to frequently asked questions. Astrobiology is an interdisciplinary field that tries to explain beyond the sky, and extraterrestrial life, where life origin came from, evolution, and the big bang. Extremophiles draw attention as the only creatures that will enlighten us in understanding extraterrestrial conditions and the mechanisms of creatures living in these conditions. This review examines the recent discoveries and the principal advances concerning both bacteria (*Chroococcidiopsis* sp., *Colwellia psychrerythraea*, *Planococcus halocryophilus*) and archaea (*Halorubrum lacusprofundi* and *Halobacterium salinarum* NRC-1) species which have potentials to examine in astrobiology as model organisms. Obtaining findings from different studies open new perspectives and strategies for several unresolved questions in astrobiology.

Keywords: *Chroococcidiopsis* sp.; *Colwellia psychrerythraea*; *Extremophiles*; *Halorubrum lacusprofundi*; *Halobacterium salinarum* NRC-1; *Martian environment*; *Planococcus halocryophilus*

1. Introduction

Russian astronomer Gavriil Adrianovich Tikhov mentioned “astrobiology” for the first time in 1953 (Tikhov, 1953; Thombre et al., 2020). Later, the space age began and astrobiology studies have been accelerated with the first artificial satellite, Sputnik, in 1957. In 1960, Joshua Lederberg studied Exo-biology and explored any clue about life in the universe (Lederberg, 1960). Lederberg together with Carl Sagan instituted exobiology as a scientific study field in NASA. The discovery of a meteorite coming from Mars increased the interest in the exobiology area in 1996. This meteorite was named AH 84001 (Allan Hills 84001) and it was observed that it had microfossil-like organic compounds (Blumberg, 2003).

Researchers wanted to promote their studies related to astrobiology, hence the NASA Astrobiology Institute (NAI) established (Morrison, 2001). Moreover, ESA (European Space Agency) was also established in 1996 (Brack et al., 1999). Later, the European Astrobiology Network Association (EAA) was

founded by the European astrobiology community in 2001. The aim is to collect information about astrobiology studies in European countries and provide collaborations among countries (Horneck et al., 2016). Thus, the term exobiology was replaced by astrobiology. Artemis program is generated by the world’s space agencies (NASA, CSA, ESA, JAXA, etc.). This program declared two main goals: going to the Moon and establishing a sustainable entity there by 2028 (Fernandez et al., 2023; Smith et al., 2020; Tarasashvili et al., 2023).

Model organisms can be easily produced, and observed, providing valuable information about their life cycle and other extinct and extant organisms. Therefore, the utilization of these species is very important to figure out what the life is. Among model organisms, extremophiles are also a fairly new field of study. Extremophiles have species in all domains. Due to their adaptations, species can live in harsh environments such as deserts, acidic mine drainage, volcanoes, glaciers, etc. Extremophiles are divided into categories according to the environments in which adapted. These divisions include

* Corresponding author.

E-mail address: simge.emlik@std.yildiz.edu.tr (S. Emlik).

<https://doi.org/10.51753/flsrt.1299840> Author contributions

Received 20 May 2023; Accepted 15 June 2023

Available online 26 August 2023

2718-062X © 2023 This is an open access article published by Dergipark under the [CC BY](https://creativecommons.org/licenses/by/4.0/) license.

thermophiles (develop above 55°C) (Atalah et al., 2019), psychrophiles (develop below 20°C) (Kirkinici et al., 2021), oligophiles (survive at low nutrient concentration) (Stan-Lotter, 2019), alkaliphiles (develop pH above 9.0) (Merino et al., 2019), acidophiles (grow at pH below 3-4) (Tripathi et al., 2021), halophiles (grow above 15% NaCl) (Stan-Lotter, 2019), barophiles or piesophiles (develop more than 0.1 MPa) (Sharma et al., 2022), etc.

The enzymes, metabolites, and biomolecules produced by extremophiles are important to survive in extreme environments and provide the usage of these organisms in biotechnological and industrial applications. In addition, these organisms are also used as model organisms for astrobiology. The aim of this study is to give detailed information and application areas of *Chroococcidiopsis* sp., *Colwellia psychrerythraea*, *Planococcus halocryophilus*, *Halorubrum lacusprofundi*, and *Halobacterium salinarum* NRC-1 which are important organisms for astrobiology.

2. Model microorganisms in astrobiology

2.1. *Chroococcidiopsis* sp.

Chroococcidiopsis sp. is a cyanobacterium and is considered an eoaerobiot, which can survive in cases of extreme desiccation (Billi and Potts, 2002; Li et al., 2022). The member of this genus lives in the dry valleys of Antarctica (Billi, 2020), the Mojave Desert in California (Billi et al., 2013), the hyper-aridity core of the Atacama Desert in Chile (Wierzchos et al., 2006; Stivaletta et al., 2012; Billi et al., 2013) and the Ross Desert in Antarctica. These areas are analogous to Martian conditions, so can be examined to understand the Martian environment and how to live in these conditions. The extraordinary abilities of these microorganisms are to tolerate desiccation, UV radiations, and ionization, making them suitable model organisms (Billi et al., 2013). *Chroococcidiopsis* sp. can be unicellular or can form few-celled packets with a non-motile state.

This extreme genus has several features to combat harsh conditions. *Chroococcidiopsis* sp. has only one nitrogenase for fixation. It protects itself against high UV rays by forming and embedding slime (Baque et al., 2013; Billi et al., 2019). The pigment formation such as carotenoids and scytonemin provides extra support against UV damage (Vitek et al., 2014; Bothe, 2019). In addition, *Chroococcidiopsis* sp. has an effective antioxidant mechanism that prevents proteins from oxidative damage. This mechanism also protects it from desiccation (Fagliarone et al., 2017). Furthermore, *Chroococcidiopsis* sp. carry out photosynthesis at 51°C (Tracy et al., 2010) and also withstands higher atmospheric pressure (Thomas et al., 2008). At high temperatures, the chances of survival in a desiccated state are higher than in a hydrated state (Cockell et al., 2017). Tolerance against acidic conditions (between pH 3 and 7) are also observed (Del Arco et al., 2018; Bothe, 2019).

Chroococcidiopsis sp. has been used in various experiments in Low Earth Orbit (LEO), simulations based on the ground of space, and Martian conditions to search for clues of life (Rabbow et al., 2009; 2017). Colonization in the interior of evaporites (3-7 mm below the halite crust) is an important research topic in different Martian areas (Stivaletta et al., 2012; Billi et al., 2013). In addition, a terrestrial analog of Martian carbonates has been found in the Mojave Desert (Bishop et al., 2011; Billi et al., 2013). In this desert, *Chroococcidiopsis* sp.

found mainly when compared to other microorganisms in red-coated carbonate rocks. It can also be tested for the panspermia theory, as the amount of observable oxygen in the planet's atmosphere increased as cyanobacteria, suggesting that oxygen may act as an indicator for the presence of life (Billi et al., 2013).

In a study, *Chroococcidiopsis* sp. CCMEE 029 was collected from the Negev Desert, and it survived 4 years in polycarbonate filters and Petri dishes, (Billi, 2009; Fagliarone et al., 2017) and 13 years in desiccated agar (Cockell et al., 2017). Moreover, it was showed that dried *Chroococcidiopsis* sp. CCMEE 029 can resist up to 24 kGy of γ -radiation (Verseux et al., 2017; Mosca et al., 2019). The dried monolayers can withstand a UV flux similar to Mars of 15 kJ/m². (Cockell et al., 2005). These results are valuable because understanding the mechanisms of desiccation tolerance will also help explain resistance under various stresses including high vacuum and radiation from space.

In a different study, *Chroococcidiopsis* sp. was isolated from solar panels and was transformable using SEVA vectors. (Baldanta et al., 2023). These vectors contain the Cpf1 nuclease, a typical CRISPR enzyme. It is suggested that this cyanobacterium with its genetically modified and strengthened features as well as its own characteristics will become a useful tool in many fields. In addition, *Chroococcidiopsis* sp. can grow in the presence of sugars such as sucrose, maltose, glucose, and fructose but cannot grow in sugary environments such as lactose, mannose, galactose, arabinose, and glycerol. The fact that *Chroococcidiopsis* sp. can also use urea as a nitrogen source in an environment such as Mars. A similar study was performed by Fernandez et al. (2023). According to their findings, *Chroococcidiopsis* sp. CCMEE 029 can serve as both a PowerCell and a nitrogen source for human synthetic urine. *Chroococcidiopsis* sp. is also important due to the use of wastewater for recycling (Baldanta et al., 2023).

Li et al. (2022) studied the change in physiological and transcriptional properties of *Chroococcidiopsis* sp. ASB-02 when it was exposed to near space in the HH-21-5 mission. It was shown a decrease in photosystem II (PSII) activity and an increase in ROS (reactive oxygen species) levels but the number of living cells remained high. Expression of extracellular polysaccharides and regulation of carotenoid and scytonemin biosynthesis genes reduced the amount of radiation reaching the cells after exposure to UV radiation. Genes involved in protein synthesis were also activated in response to cold conditions in addition to radiation. It was also noted that genes in several DNA and PSII repair pathways were elevated after rehydration. This proved that cells' DNA and PSII proteins had been damaged, highlighting the necessity of repair mechanisms for the cyanobacterium's recovery.

2.2. *Colwellia psychrerythraea*

Colwellia psychrerythraea belonging to the Colwelliaceae family is a marine heterotrophic bacterium (Liu et al., 2020). This bacterium has become important for studying adaptive strategies against cold and salinity habitats and may be for extraterrestrial conditions (Mudge et al., 2021; Casillo et al., 2022). This species can grow at -12°C to 22°C, and 15 to 70 ppt in salinity (Wells and Deming, 2006). Due to its genome and many eccentric biochemical characteristics, it has become a model microorganism for carbon cycling in cold sea sediments. It can also be utilized for observing growth and survival under simulated Martian conditions (Hallsworth et al., 2021).

It is a polyextremophilic bacterium species isolated from sub-zero marine sediments. *C. psychrerythraea* strain 34H (*Cp34H*) is a Gram-negative psychrophile isolated from Arctic marine sediments at -1°C (Huston, 2003; Methé et al., 2005). To endure fluctuations in salinity in sea ice brines, this strain can transport suitable solutes (small molecular weight organic molecules) (Firth et al., 2016). *Cp34H* can live in the cold dark ocean without proteorhodopsins which are photoactive proteins utilized by many bacteria in the ocean to produce additional energy (Béja, 2001).

Enzymes involved in adaptation to cold stress show great economic and ecological benefits in terms of their structures and functions (Kavitha, 2016). It has been shown that *Cp34H* can produce functional extracellular enzymes even in the harshest conditions (-8°C , 35 ppt). Compared to warmer temperatures, enzyme activity rates increased at less extreme temperatures (-1°C) (Huston et al., 2000). On the other hand, *Cp34H* can still survive for a short time when exposed to a warmer and stressful room temperature (Showalter and Deming, 2018). It was also reported that catabolic pathways and flagella-related genes were significantly downregulated as a result of transcriptomic analyses (Czajka et al., 2018; Showalter and Deming, 2018).

Cp34H has a proteome with 4910 predicted proteins (Methé et al., 2005) and 2362 of them were identified (Mudge et al., 2021). Proteins play roles in diverse cellular motility consisting of flagellar, pilus, and chemotaxis. This situation supports the results of previous investigations of *Cp34H* in response to sub-zero temperatures, offering biomarkers for motility for life as requested by NASA's Ladder of Life Detection (Nunn et al., 2015; Showalter and Deming, 2018; Neveu et al., 2018). Future astrobiology missions must be able to find biomarkers because the majority of the solar system's planets have high salinities, little water activity, and temperatures below the freezing point of water (Carr et al., 1998; Khurana et al., 1998; Hand et al., 2009; Parro et al., 2018; Hendrix et al., 2019). Findings of small (3–4 amino acid) peptides on ice worlds that are analogous to those found on Earth are crucial for the discovery of observable biomarkers for life in the future (Mudge et al., 2021). Four physiological states were observed in *Cp34H* after 1 month of incubation period: growing and culturable cells (high activity and culturability at -5°C , artificial seawater), active cells (low activity and acceptable culturability at -5°C in brine), viable but not culturable (acceptable activity and very low or no culturability at -10°C , artificial seawater without nutrient) and surviving cells (very low to no activity and not culturable at -10°C in brine) (Mudge et al., 2021).

2.3. *Planococcus halocryophilus*

Planococcus consists of Gram-positive and aerobic cocci. Like other species mentioned above, *Planococcus* can grow at moderate/low temperatures and in salt environments (Arctic, Antarctic, marine) (Mykytczuk et al., 2012). Moreover, some *Planococcus* species are resistant to heavy metals, and some can detoxify pollutants (Li et al., 2006; Hupert-Kocurek et al., 2014; Jung et al., 2018). It is very important to examine this bacterium in non-NaCl salty and sub-zero temperature habitats, and this topic has gained interest in astrobiology (Heinz et al., 2018). In this sense, *P. halocryophilus* is an ideal model organism for Martian environments (Heinz et al., 2018).

P. halocryophilus lives in an active permafrost soil layer in the Canadian High Arctic. It is a psychrotolerant bacterium

adapted to cold stress due to the expression of several osmolyte transporters, cold-adapted proteins, and carbohydrate storage as energy (Mykytczuk et al., 2013, 2016). While it can grow at a concentration of 19% NaCl (w/v) and -15°C , some studies reported that it has metabolic activity at -25°C (Mykytczuk et al., 2013; Raymond-Bouchard et al., 2017).

According to laboratory investigations, the survival of cryotolerant and halotolerant bacterial species in concentrated brine depends on the salt concentration, anion parameters, and water activity. The potential habitability of Martian cryobrines was therefore discovered to depend on factors such as anion brine composition, salt content, and water activity (Waajen et al., 2020). It is known that several chlorides (Cl^-) and perchlorate (ClO_4^-) salts are found in Martian soils (Hecht et al., 2009; Kounaves et al., 2010). How well and how long *P. halocryophilus* can survive multiple freeze/thaw cycles, subzero Cl^- and ClO_4^- brines have been explored since these extreme conditions on Mars may exist momentarily and/or continue cyclically (Martínez and Renno, 2013). Heinz et al. (2018) reported that the survival rate of this bacterium in samples containing Cl^- was higher than in ClO_4^- samples at all temperatures. Furthermore, it was also revealed that lifespan enhanced systematically with decreasing temperatures in Cl^- and ClO_4^- samples.

2.4. *Halorubrum lacusprofundi*

In addition to bacteria, the archaea species have been widely examined in extreme conditions and astrobiology. *Halorubrum lacusprofundi* is one of them. It is a halophilic species with vivid pigmentation that forms biofilms in the hypersaline Deep Lake in Antarctica (Anderson et al., 2016). *H. lacusprofundi* can live anaerobically by using perchlorate as a terminal electron acceptor, providing a metabolism for the probability of survival on the Red Planet (DasSarma et al., 2020).

H. lacusprofundi grows optimally at $31\text{--}37^{\circ}\text{C}$ (Franzmann et al., 1988) but can also live in Antarctica (-18°C to $11,5^{\circ}\text{C}$ and 21–28%, w/v salt content). Moreover, it develops approximately 3.5 M NaCl concentration (DasSarma et al., 2013; DasSarma and DasSarma, 2018; Laye and Dassarma, 2018). It is crucial to determine the limits of adaptation to hypersaline and low-temperature conditions to predict the presence of life in the icy shells (Trumbo et al., 2019) and oceans of Europa and Enceladus (Lobo et al., 2021), the permafrost on Mars (Morozova et al., 2007), subterranean lakes (Lauro et al., 2021) by using *H. lacusprofundi*. It can also grow anaerobically at low ClO_4^- concentrations. Moreover, reports have shown that magnesium perchlorate (MgClO_4^-) is inhibited the growth with greater sensitivity than sodium perchlorate (NaClO_4^-) at significantly higher concentrations (50% inhibition at 0.3 M for sodium perchlorate, 0.1 M for magnesium perchlorate) (Laye and Dassarma, 2018). As a result of spectroscopic analysis, Martian soil was found to contain poisonous NaClO_4^- and MgClO_4^- (Mattie et al., 2006; Wadsworth and Cockell, 2017). The levels of growth inhibition and enzyme activity demonstrated that extreme halophiles like *H. lacusprofundi* will not be adversely affected by the anticipated levels of ClO_4^- salts on Mars (Laye and Dassarma, 2018).

2.5. *Halobacterium salinarum* NRC-1

Halobacterium is a halophilic archaea that can develop in

hypersaline aquatic environments (DasSarma et al., 2018). *Halobacterium* can be visible as red, pink, or purple due to carotenoids found in their membranes. *Halobacterium* can live in multiple extreme conditions and therefore, are also called polyextremophiles. Similar to other organisms mentioned in this review, these organisms can use as model organisms for astrobiology, thus also given the name “exophiles” (DasSarma, 2006; DasSarma and DasSarma, 2017; DasSarma and DasSarma, 2018). Halophilic archaea show different ways of production of energy and even anaerobic development (Sundarasami et al., 2019). These organisms use trimethylamine N-oxide [(CH₃)₃NO], dimethyl sulfoxide (DMSO), fumarate (C₄H₄O₄), ClO₄⁻, and chlorate (ClO₃⁻) instead of oxygen as electron acceptors, making them good alternatives for investigations (Müller and DasSarma, 2005; Oren, 2014).

H. salinarum is a rod-shaped, motile, and highly halophilic archaea. The most extensively researched haloarchaeal genome is the 2.57 Mbp genome of *H. salinarum* NRC-1 which was the first genome to be fully sequenced. It has high genetic diversity due to the high GC content of the parent chromosome (~68%) compared to its plasmid (57-60% G+C) (Ng et al., 2000; Pfeiffer et al., 2008). This extremophile model of archaea has been taken into consideration and thoroughly explored, leading to various discoveries and knowledge about the biology of archaea and the adaptations needed to survive in saturated salt concentrations (Soppa, 2006; Beer et al., 2014).

Furthermore, the processes of resistance to high and low osmolarity, high and low temperatures, UV and ionizing radiation have been studied in investigations on *H. salinarum* NRC-1 (DasSarma, 2006). It is believed that because of its effective light and dark healing mechanisms, it can withstand UVC rays up to 100 J/m². In one study, *Halococcus*

dombrowskii, *H. salinarum* NRC-1 and *Haloarcula japonica* were grown halite after that exposed to UV radiation (200-400 nm) to simulate flux similar to the Martian surface. As a result of the study, it was reported that the cells did not show any loss of viability after exposure to 21 kJ/m² radiation. Then the cells continued to grow after 12 days in the liquid medium following the exposure to total radiation of 148 kJ/m² (Fendrihan et al., 2009).

3. Conclusion

Organisms living in extreme conditions provide detailed information about not only life on Earth but also space which is the area of astrobiology. This topic has gained interest in the last decades; therefore, studies in multidisciplinary areas are carried out by simulating environmental conditions that are comparable to the conditions in space. In this respect, extremophiles draw attention due to their characteristics including living in low/high temperatures, radiation, salt environments, etc. On the other hand, it is worth pointing out that it is the beginning stage to examine microorganisms to have the potential for usage of astrobiology. As a result, significant advancements in astrobiology could result from fascinating discoveries in the microbial world during the next years, providing a profound effect on how is seen the nature of life.

Conflict of interest: The authors declare that they have no conflict of interests.

Informed consent: The authors declare that this manuscript did not involve human or animal participants and informed consent was not collected.

References

- Anderson, I. J., DasSarma, P., Lucas, S., Copeland, A., Lapidus, A., Del Rio, T. G., ... & Kyrpidis, N. C. (2016). Complete genome sequence of the Antarctic *Halorubrum lacusprofundi* type strain ACAM 34. *Standards in Genomic Sciences*, 11(1), 1-6.
- Atalah, J., Cáceres-Moreno, P., Espina, G., & Blamey, J. M. (2019). Thermophiles and the applications of their enzymes as new biocatalysts. *Bioresource Technology*, 280, 478-488.
- Baldanta, S., Arnal, R., Blanco-Rivero, A., Guevara, G., & Llorens, J. M. N. (2023). First characterization of cultivable extremophile *Chroococcidiopsis* isolates from a solar panel. *Frontiers in Microbiology*, 14.
- Baqué, M., de Vera, J. P., Rettberg, P., & Billi, D. (2013). The BOSS and BIOMEX space experiments on the EXPOSE-R2 mission: Endurance of the desert cyanobacterium *Chroococcidiopsis* under simulated space vacuum, Martian atmosphere, UVC radiation and temperature extremes. *Acta Astronautica*, 91, 180-186.
- Beer, K. D., Wurtmann, E. J., Pinel, N., & Baliga, N. S. (2014). Model organisms retain an “ecological memory” of complex ecologically relevant environmental variation. *Applied and Environmental Microbiology*, 80(6), 1821-1831.
- Béja, O., Spudich, E. N., Spudich, J. L., Leclerc, M., & DeLong, E. F. (2001). Proteorhodopsin phototrophy in the ocean. *Nature*, 411(6839), 786-789.
- Billi, D. (2009). Subcellular integrities in *Chroococcidiopsis* sp. CCMEE 029 survivors after prolonged desiccation revealed by molecular probes and genome stability assays. *Extremophiles*, 13, 49-57.
- Billi, D., Baqué, M., Smith, H., & McKay, C. (2013). Cyanobacteria from extreme deserts to space. *Advances in Microbiology*, 3(6), 80-86.
- Billi, D., & Potts, M. (2002). Life and death of dried prokaryotes. *Research in microbiology*, 153(1), 7-12.
- Billi, D., Staibano, C., Verseux, C., Fagliarone, C., Mosca, C., Baqué, M., ... & Rettberg, P. (2019). Dried biofilms of desert strains of *Chroococcidiopsis* survived prolonged exposure to space and Mars-like conditions in low Earth orbit. *Astrobiology*, 19(8), 1008-1017.
- Billi, D. (2020). Challenging the survival thresholds of a desert Cyanobacterium under laboratory simulated and space conditions. *Extremophiles as Astrobiological Models*, 183-195.
- Bishop, J. L., Schelble, R. T., McKay, C. P., Brown, A. J., & Perry, K. A. (2011). Carbonate rocks in the Mojave Desert as an analogue for Martian carbonates. *International Journal of Astrobiology*, 10(4), 349-358.
- Blumberg, B. S. (2003). The NASA Astrobiology Institute: early history and organization. *Astrobiology*, 3(3), 463-470.
- Bothe, H. (2019). The Cyanobacterium *Chroococcidiopsis* and its potential for life on mars. *Journal of Astrobiology and Space Science Reviews*, 2, 398-412.
- Brack, A., Clancy, P., Fitton, B., Hofmann, B., Horneck, G., Kurat, G., ... & Westall, F. (1999). An integrated exobiology package for the search for life on Mars. *Advances in Space Research*, 23(2), 301-308.
- Carr, M. H., Belton, M. J., Chapman, C. R., Davies, M. E., Geissler, P., Greenberg, R., ... & Veverka, J. (1998). Evidence for a subsurface ocean on Europa. *Nature*, 391(6665), 363-365.
- Casillo, A., D'Angelo, C., Parrilli, E., Tutino, M. L., & Corsaro, M. M. (2022). Membrane and extracellular matrix glycopolymers of *Colwellia psychrerythraea* 34H: Structural changes at different growth temperatures. *Frontiers in Microbiology*, 13, 120.
- Cockell, C. S., Brown, S., Landenmark, H., Samuels, T., Siddall, R., & Wadsworth, J. (2017). Liquid water restricts habitability in extreme deserts. *Astrobiology*, 17(4), 309-318.
- Cockell, C. S., Schuenger, A. C., Billi, D., Friedmann, E. I., & Panitz, C. (2005). Effects of a simulated martian UV flux on the cyanobacterium, *Chroococcidiopsis* sp. 029. *Astrobiology*, 5(2), 127-140.
- Czajka, J. J., Abernathy, M. H., Benites, V. T., Baidoo, E. E., Deming, J. W., & Tang, Y. J. (2018). Model metabolic strategy for heterotrophic bacteria in the cold ocean based on *Colwellia psychrerythraea* 34H. *Proceedings of the National Academy of Sciences*, 115(49),

- 12507-12512.
- DasSarma, P., Capes, M. D., & DasSarma, S. (2019). Comparative genomics of Halobacterium strains from diverse locations. In: Das S., Dash H. R. (eds) *Microbial Diversity in the Genomic Era* (pp. 285-322). Academic Press.
- DasSarma, P., & DasSarma, S. (2018). Survival of microbes in Earth's stratosphere. *Current Opinion in Microbiology*, 43, 24-30.
- DasSarma, P., Zamora, R. C., Müller, J. A., & DasSarma, S. (2012). Genome-wide responses of the model archaeon *Halobacterium* sp. strain NRC-1 to oxygen limitation. *Journal of Bacteriology*, 194(20), 5530-5537.
- DasSarma, S. (2006). Extreme halophiles are models for astrobiology. *Microbe-American Society for Microbiology*, 1(3), 120.
- DasSarma, S., Capes, M. D., Karan, R., & DasSarma, P. (2013). Amino acid substitutions in cold-adapted proteins from *Halorubrum lacusprofundi*, an extremely halophilic microbe from Antarctica. *PLoS One*, 8(3), e58587.
- DasSarma, S., & DasSarma, P. (2017). Halophiles. *eLS*, 1-13.
- DasSarma, S., DasSarma, P., Laye, V. J., & Schwieterman, E. W. (2020). Extremophilic models for astrobiology: haloarchaeal survival strategies and pigments for remote sensing. *Extremophiles*, 24, 31-41.
- Del Arco, J., Sánchez-Murcia, P. A., Mancheño, J. M., Gago, F., & Fernández-Lucas, J. (2018). Characterization of an atypical, thermostable, organic solvent-and acid-tolerant 2'-deoxyribosyltransferase from *Chroococcidiopsis thermalis*. *Applied Microbiology and Biotechnology*, 102, 6947-6957.
- Faglierone, C., Mosca, C., Ubaldi, I., Verseux, C., Baqué, M., Wilmotte, A., & Billi, D. (2017). Avoidance of protein oxidation correlates with the desiccation and radiation resistance of hot and cold desert strains of the cyanobacterium *Chroococcidiopsis*. *Extremophiles*, 21, 981-991.
- Fendrihan, S., Bérces, A., Lammer, H., Musso, M., Rontó, G., Polacsek, T. K., ... & Stan-Lotter, H. (2009). Investigating the effects of simulated Martian ultraviolet radiation on *Halococcus dombrowskii* and other extremely halophilic archaeobacteria. *Astrobiology*, 9(1), 104-112.
- Fernandez, B. G., Rothschild, L. J., Faglierone, C., Chiavarini, S., & Billi, D. (2023). Feasibility as feedstock of the cyanobacterium *Chroococcidiopsis* sp. 029 cultivated with urine-supplemented moon and mars regolith simulants. *Algal Research*, 71, 103044.
- Firth, E., Carpenter, S. D., Sørensen, H. L., Collins, R. E., & Deming, J. W. (2016). Bacterial use of choline to tolerate salinity shifts in sea-ice brines. *Elementa: Science of the Anthropocene*, 4, 000120.
- Franzmann, P. D., Stackebrandt, E., Sanderson, K., Volkman, J. K., Cameron, D. E., Stevenson, P. L., ... & Burton, H. R. (1988). *Halobacterium lacusprofundi* sp. nov., a halophilic bacterium isolated from Deep Lake, Antarctica. *Systematic and Applied Microbiology*, 11(1), 20-27.
- Hallsworth, J. E., Mancinelli, R. L., Conley, C. A., Dallas, T. D., Rinaldi, T., Davila, A. F., ... & Madigan, M. T. (2021). Astrobiology of life on Earth. *Environmental Microbiology*, 23(7), 3335-3344.
- Hand, K. P., Chyba, C. F., Priscu, J. C., Carlson, R. W., & Nealson, K. H. (2009). Astrobiology and the potential for life on Europa. *Europa*, 589-629.
- Hecht, M. H., Kounaves, S. P., Quinn, R. C., West, S. J., Young, S. M., Ming, D. W., ... & Smith, P. H. (2009). Detection of perchlorate and the soluble chemistry of martian soil at the Phoenix lander site. *Science*, 325(5936), 64-67.
- Heinz, J., Schirmack, J., Airo, A., Kounaves, S. P., & Schulze-Makuch, D. (2018). Enhanced microbial survivability in subzero brines. *Astrobiology*, 18(9), 1171-1180.
- Hendrix, A. R., Hurford, T. A., Barge, L. M., Bland, M. T., Bowman, J. S., Brinckerhoff, W., ... & Vance, S. D. (2019). The NASA roadmap to ocean worlds. *Astrobiology*, 19(1), 1-27.
- Horneck, G., Walter, N., Westall, F., Grenfell, J. L., Martin, W. F., Gomez, F., ... & Capria, M. T. (2016). AstRoMap European astrobiology roadmap. *Astrobiology*, 16(3), 201-243.
- Hupert-Kocurek, K., Wojcieszynska, D., & Guzik, U. (2014). Activity of a carboxyl-terminal truncated form of catechol 2, 3-dioxygenase from *Planococcus* sp. S5. *The Scientific World Journal*, 2014.
- Huston, A. L. (2003). *Bacterial adaptation to the cold: in situ activities of extracellular enzymes in the North Water polynya and characterization of a cold-active aminopeptidase from Colwellia psychrerythraea strain 34H*. University of Washington.
- Huston, A. L., Krieger-Brockett, B. B., & Deming, J. W. (2000). Remarkably low temperature optima for extracellular enzyme activity from Arctic bacteria and sea ice. *Environmental Microbiology*, 2(4), 383-388.
- Jung, J. H., Joe, M. H., Kim, D. H., Park, H., Choi, J. I., & Lim, S. (2018). Complete genome sequence of *Planococcus* sp. PAMC21323 isolated from Antarctica and its metabolic potential to detoxify pollutants. *Standards in Genomic Sciences*, 13, 1-9.
- Kavitha, M. (2016). Cold active lipases-an update. *Frontiers in Life Science*, 9(3), 226-238.
- Khurana, K. K., Kivelson, M. G., Stevenson, D. J., Schubert, G., Russell, C. T., Walker, R. J., & Polansky, C. (1998). Induced magnetic fields as evidence for subsurface oceans in Europa and Callisto. *Nature*, 395(6704), 777-780.
- Kirkinci, S. F., Edbeib, M. F., Aksoy, H. M., Marakli, S., & Kaya, Y. (2021). Identification of Dalapon degrading bacterial strain, *Psychrobacter* sp. TaeBurcu001 isolated from Antarctica. *Polar Science*, 28, 100656.
- Kounaves, S. P., Hecht, M. H., Kapit, J., Gospodinova, K., DeFlores, L., Quinn, R. C., ... & Young, S. M. M. (2010). Wet Chemistry experiments on the 2007 Phoenix Mars Scout Lander mission: Data analysis and results. *Journal of Geophysical Research: Planets*, 115(E1).
- Lauro, S. E., Pettinelli, E., Caprarelli, G., Guallini, L., Rossi, A. P., Mattei, E., ... & Orosei, R. (2021). Multiple subglacial water bodies below the south pole of Mars unveiled by new MARSIS data. *Nature Astronomy*, 5(1), 63-70.
- Laye, V. J., & DasSarma, S. (2018). An Antarctic extreme halophile and its polyextremophilic enzyme: effects of perchlorate salts. *Astrobiology*, 18(4), 412-418.
- Lederberg, J. (1960). Exobiology: approaches to life beyond the Earth. *Science*, 132(3424), 393-400.
- Li, C., Zhang, X., Ye, T., Li, X., & Wang, G. (2022). Protection and damage repair mechanisms contributed to the survival of *Chroococcidiopsis* sp. exposed to a mars-like near space environment. *Microbiology Spectrum*, 10(6), e03440-22.
- Li, H., Liu, Y. H., Luo, N., Zhang, X. Y., Luan, T. G., Hu, J. M., ... & Lu, J. Q. (2006). Biodegradation of benzene and its derivatives by a psychrotolerant and moderately haloalkaliphilic *Planococcus* sp. strain ZD22. *Research in Microbiology*, 157(7), 629-636.
- Liu, A., Zhang, Y. J., Cheng, P., Peng, Y. J., Blom, J., & Xue, Q. J. (2020). Whole genome analysis calls for a taxonomic rearrangement of the genus *Colwellia*. *Antonie van Leeuwenhoek*, 113, 919-931.
- Lobo, A. H., Thompson, A. F., Vance, S. D., & Tharimena, S. (2021). A pole-to-equator ocean overturning circulation on Enceladus. *Nature Geoscience*, 14(4), 185-189.
- Martínez, G., & Renno, N. O. (2013). Water and brines on Mars: current evidence and implications for MSL. *Space Science Reviews*, 175, 29-51.
- Mattie, D. R., Strawson, J., & Zhao, J. (2006). Perchlorate toxicity and risk assessment. *Perchlorate: Environmental Occurrence, Interactions and Treatment*, 169-196.
- Merino, N., Aronson, H. S., Bojanova, D. P., Feyhl-Buska, J., Wong, M. L., Zhang, S., & Giovannelli, D. (2019). Living at the extremes: extremophiles and the limits of life in a planetary context. *Frontiers in Microbiology*, 10, 780.
- Méthé, B. A., Nelson, K. E., Deming, J. W., Momen, B., Melamud, E., Zhang, X., ... & Fraser, C. M. (2005). The psychrophilic lifestyle as revealed by the genome sequence of *Colwellia psychrerythraea* 34H through genomic and proteomic analyses. *Proceedings of the National Academy of Sciences*, 102(31), 10913-10918.
- Morozova, D., Möhlmann, D., & Wagner, D. (2007). Survival of methanogenic archaea from Siberian permafrost under simulated Martian thermal conditions. *Origins of Life and Evolution of Biospheres*, 37, 189-200.
- Morrison, D. (2001). The NASA astrobiology program. *Astrobiology*, 1(1), 3-13.
- Mosca, C., Rothschild, L. J., Napoli, A., Ferré, F., Pietrosanto, M., Faglierone, C., ... & Billi, D. (2019). Over-expression of UV-damage DNA repair genes and ribonucleic acid persistence contribute to the resilience of dried biofilms of the desert cyanobacterium *Chroococcidiopsis* exposed to Mars-like UV flux and long-term desiccation. *Frontiers in Microbiology*, 10, 2312.
- Mudge, M. C., Nunn, B. L., Firth, E., Ewert, M., Hales, K., Fondrie, W. E., ... & Junge, K. A. (2021). Subzero, saline incubations of *Colwellia psychrerythraea* reveal strategies and biomarkers for sustained life in extreme icy environments. *Environmental Microbiology*, 23(7), 3840-

- 3866.
- Müller, J. A., & DasSarma, S. (2005). Genomic analysis of anaerobic respiration in the archaeon *Halobacterium* sp. strain NRC-1: dimethyl sulfoxide and trimethylamine N-oxide as terminal electron acceptors. *Journal of Bacteriology*, 187(5), 1659-1667.
- Mykytczuk, N., Foote, S. J., Omelon, C. R., Southam, G., Greer, C. W., & Whyte, L. G. (2013). Bacterial growth at -15°C; molecular insights from the permafrost bacterium *Planococcus halocryophilus* Or1. *The ISME Journal*, 7(6), 1211-1226.
- Mykytczuk, N. C. S., Lawrence, J. R., Omelon, C. R., Southam, G., & Whyte, L. G. (2016). Microscopic characterization of the bacterial cell envelope of *Planococcus halocryophilus* Or1 during subzero growth at -15°C. *Polar Biology*, 39, 701-712.
- Mykytczuk, N. C., Wilhelm, R. C., & Whyte, L. G. (2012). *Planococcus halocryophilus* sp. nov., an extreme sub-zero species from high Arctic permafrost. *International Journal of Systematic and Evolutionary Microbiology*, 62(Pt_8), 1937-1944.
- Neveu, M., Hays, L. E., Voytek, M. A., New, M. H., & Schulte, M. D. (2018). The ladder of life detection. *Astrobiology*, 18(11), 1375-1402.
- Ng, W. V., Kennedy, S. P., Mahairas, G. G., Berquist, B., Pan, M., Shukla, H. D., ... & DasSarma, S. (2000). Genome sequence of *Halobacterium* species NRC-1. *Proceedings of the National Academy of Sciences*, 97(22), 12176-12181.
- Nunn, B. L., Slattery, K. V., Cameron, K. A., Timmins-Schiffman, E., & Junge, K. (2015). Proteomics of *Colwellia psychrerythraea* at subzero temperatures—a life with limited movement, flexible membranes and vital DNA repair. *Environmental Microbiology*, 17(7), 2319-2335.
- Oren, A. (2014). Halophilic archaea on Earth and in space: growth and survival under extreme conditions. *Philosophical Transactions of the Royal Society A: Mathematical, Physical and Engineering Sciences*, 372(2030), 20140194.
- Parro, V., Blanco, Y., Puente-Sánchez, F., Rivas, L. A., Moreno-Paz, M., Echeverría, A., ... & Cabrol, N. A. (2018). Biomarkers and metabolic patterns in the sediments of evolving glacial lakes as a proxy for planetary lake exploration. *Astrobiology*, 18(5), 586-606.
- Pfeiffer, F., Schuster, S. C., Broicher, A., Falb, M., Palm, P., Rodewald, K., ... & Oesterhelt, D. (2008). Evolution in the laboratory: the genome of *Halobacterium salinarum* strain R1 compared to that of strain NRC-1. *Genomics*, 91(4), 335-346.
- Rabbow, E., Horneck, G., Rettberg, P., Schott, J. U., Panitz, C., L'Afflitto, A., ... & Reitz, G. (2009). EXPOSE, an astrobiological exposure facility on the international space station—from proposal to flight. *Origins of Life and Evolution of Biospheres*, 39, 581-598.
- Rabbow, E., Rettberg, P., Parpart, A., Panitz, C., Schulte, W., Molter, F., ... & Willnecker, R. (2017). EXPOSE-R2: the astrobiological ESA mission on board of the International Space Station. *Frontiers in Microbiology*, 8, 1533.
- Raymond-Bouchard, I., Chourey, K., Altshuler, I., Iyer, R., Hettich, R. L., & Whyte, L. G. (2017). Mechanisms of subzero growth in the cryophile *Planococcus halocryophilus* determined through proteomic analysis. *Environmental Microbiology*, 19(11), 4460-4479.
- Sharma, S., Chaturvedi, U., Sharma, K., Vaishnav, A., & Singh, H. B. (2022). An Overview of Survival Strategies of Psychrophiles and Their Applications. *Survival Strategies in Cold-adapted Microorganisms*, 133-151.
- Showalter, G. M., & Deming, J. W. (2018). Low-temperature chemotaxis, halotaxis and chemohalotaxis by the psychrophilic marine bacterium *Colwellia psychrerythraea* 34H. *Environmental Microbiology Reports*, 10(1), 92-101.
- Smith, M., Craig, D., Herrmann, N., Mahoney, E., Krezel, J., McIntyre, N., & Goodliff, K. (2020). The artemis program: An overview of NASA's activities to return humans to the moon. In *2020 IEEE Aerospace Conference*, IEEE, 1-10.
- Soppa, J. (2006). From genomes to function: haloarchaea as model organisms. *Microbiology*, 152(3), 585-590.
- Stan-Lotter, H. (2019). Survival of subsurface microbial communities over geological times and the implications for astrobiology. In: Seckbach J., Rampelotto P. (eds) *Model Ecosystems in Extreme Environments* (pp. 169-187). Academic Press.
- Stivaletta, N., Barbieri, R., & Billi, D. (2012). Microbial colonization of the salt deposits in the driest place of the Atacama Desert (Chile). *Origins of Life and Evolution of Biospheres*, 42, 187-200.
- Sundarasami, A., Sridhar, A., & Mani, K. (2019). Halophilic archaea as beacon for exobiology: Recent advances and future challenges. *Advances in Biological Science Research*, 197-214.
- Tarasashvili, M. V., Elbakidze, K., Doborjginidze, N. D., & Gharibashvili, N. D. (2023). Carbonate precipitation and nitrogen fixation in AMG (Artificial Martian Ground) by cyanobacteria. *Life Sciences in Space Research*, 37, 65-77.
- Thomas, D. J., Eubanks, L. M., Rector, C., Warrington, J., & Todd, P. (2008). Effects of atmospheric pressure on the survival of photosynthetic microorganisms during simulations of ecopoiesis. *International Journal of Astrobiology*, 7(3-4), 243-249.
- Thombre, R. S., Vaishampayan, P. A., & Gomez, F. (2020). Applications of extremophiles in astrobiology. In: Salwan R., Sharma V. (eds) *Physiological and Biotechnological Aspects of Extremophiles* (pp. 89-104). Academic Press.
- Tikhov, G. A. (1953). *Astrobiology. Molodaya gvardia* (Young Guard) Moscow: Publishing House.
- Tracy, C. R., Streten-Joyce, C., Dalton, R., Nussear, K. E., Gibb, K. S., & Christian, K. A. (2010). Microclimate and limits to photosynthesis in a diverse community of hypolithic cyanobacteria in northern Australia. *Environmental Microbiology*, 12(3), 592-607.
- Tripathi, S., Singh, K., & Chandra, R. (2021). Adaptation of bacterial communities and plant strategies for amelioration and eco-restoration of an organometallic industrial waste polluted site. In: Singh J. S., Singh C., Tiwari S., Singh A. K. (eds) *Microbes in Land Use Change Management* (pp. 45-90). Elsevier.
- Trumbo, S. K., Brown, M. E., & Hand, K. P. (2019). Sodium chloride on the surface of Europa. *Science Advances*, 5(6), eaaw7123.
- Verseux, C., Baqué, M., Cifariello, R., Fagliarone, C., Raguse, M., Moeller, R., & Billi, D. (2017). Evaluation of the resistance of *Chroococcidiopsis* spp. to sparsely and densely ionizing irradiation. *Astrobiology*, 17(2), 118-125.
- Vítek, P., Jehlička, J., Ascaso, C., Mašek, V., Gómez-Silva, B., Olivares, H., & Wierzbos, J. (2014). Distribution of scytonemin in endolithic microbial communities from halite crusts in the hyperarid zone of the Atacama Desert, Chile. *FEMS Microbiology Ecology*, 90(2), 351-366.
- Waajen, A. C., Heinz, J., Airo, A., & Schulze-Makuch, D. (2020). Physicochemical salt solution parameters limit the survival of *Planococcus halocryophilus* in Martian Cryobrines. *Frontiers in Microbiology*, 11, 1284.
- Wadsworth, J., & Cockell, C. S. (2017). Perchlorates on Mars enhance the bacteriocidal effects of UV light. *Scientific Reports*, 7(1), 4662.
- Wells, L. E., & Deming, J. W. (2006). Characterization of a cold-active bacteriophage on two psychrophilic marine hosts. *Aquatic Microbial Ecology*, 45(1), 15-29.
- Wierzbos, J., Ascaso, C., & McKay, C. P. (2006). Endolithic cyanobacteria in halite rocks from the hyperarid core of the Atacama Desert. *Astrobiology*, 6(3), 415-422.

Cite as: Emlik, S., & Marakli, S. (2023). Important extremophilic model microorganisms in astrobiology. *Front Life Sci RT*, 4(2), 105-110.